Characterization of First Phosphate's Bégin-Lamarche Phosphate Deposit (*North and South Zone*), Lac-Saint-Jean Anorthositic (LSJA) Suite, Quebec, Canada: Implications for Supplying Lithium Ferro (Iron) Phosphate (LFP) Batteries

Dr. Sandeep Banerjee, P. Geo

Queen's University, Kingston, Ontario, Canada

Prof. Sarah Dare

Université du Québec à Chicoutimi (UQAC), Chicoutimi, Québec, Canada

Prof. Peir K. Pufahl, P. Geo

Queen's University, Kingston, Ontario, Canada

Respectfully Submitted on January 6, 2025

EXECUTIVE SUMMARY

The purpose of this report is to describe and interpret the mineralogy, petrology, and geochemistry of First Phosphate's Bégin-Lamarche igneous (anorthosite-hosted) phosphate deposit (**North and South Zone**). The Bégin-Lamarche is a part of the 1.14 Ga Lac-Saint-Jean Anorthositic (LSJA) Suite, Québec, which is the largest massif-anorthosite complex in the world. The primary aim of this partnership is to assess the quality of phosphatic ore for the manufacture of lithium ferro (iron) phosphate (LFP) batteries. The major findings of this study are described below.

- Fluorapatite is the primary ore mineral. The ore mineral occurs within oxide-apatite rich mafic rocks (comprising gabbronorite, olivine gabbronorite, olivine gabbro, norite, olivine norite, and leuco-troctolite), oxide-apatite ultramafic rocks (comprising dunite, lherzolite, harzburgite, wehrlite, olivine websterite, and orthopyroxenite) and nelsonite (massive oxide-apatite).

- These rocks contain variable amounts of olivine, orthopyroxene, clinopyroxene, plagioclase, amphibole, biotite, chlorite, fluorapatite, ilmenite, magnetite, and Al-spinel. The ore mineral, fluorapatite, is mostly associated with oxide minerals (ilmenite + magnetite).

- Initial results indicate that after beneficiation, the concentrate has a similar P_2O_5 concentration (40.9 wt.%) to that of *in situ* (fluor)apatite crystals of the mineralization (41.7 ±0.13 wt.%), indicating a high P_2O_5 recovery from the mineralization. The low minor element ratio (MER; 0.04) of the apatite concentrate and low concentrations of Si, Ti, Na, As, Cd, Th, and U within fluorapatite indicate the high quality of the phosphate ore for producing phosphoric acid.

- Most of the samples (74%) from the North and South Zone of the Bégin-Lamarche deposit contain fluorapatite with low Cl contents (<1000 ppm).

- The fluorapatite with low concentrations of trace elements is expected to produce high-quality phosphogypsum (with low toxic elements) during phosphoric acid production. The high-quality phosphogypsum will be a prospective raw material for plaster and wallboard production. Ilmenite and magnetite ***could also be*** potentially saleable by-products for Ti and Fe, respectively.

- Furthermore, mafic silicates (olivine and pyroxene) and plagioclase, the gangue minerals of the deposit, could be used for CO_2 sequestration and will help reduce the carbon footprint of the atmosphere.

- Finally, a very low amount of sulfide minerals (< 1%) in the deposit reduces the risk of acid mine drainage. Therefore, high-quality (fluor)apatite with low contents of toxic trace elements makes the Bégin-Lamarche deposit an attractive ESG (environmental, social, and governance)-compliant source of North American P for the LFP battery industry.

TABLE OF CONTENTS

1. Introduction 4

2. Objectives and deliverables 4

3. Background 6

4. Location 8

5. Geological Setting
   - 5.1 Regional geology 8
   - 5.2 Local geology 13

6. Sampling 13

7. Methods
   - 7.1. Mineral liberation analysis (MLA) 17
   - 7.2. Electron-probe micro-analysis (EPMA) 17
   - 7.3. Laser ablation–inductively coupled plasma-mass spectrometry (LA-ICP-MS) analysis 18

8. Results
   - 8.1. Mineralogy and mineral chemistry of the Bégin-Lamarche deposit (North and South Zone) 19
   - 8.2. Rare earth elements (REE) of apatite and silicate minerals 52
   - 8.3. Chemistry of the Bégin-Lamarche (North and South Zone) apatite concentrate 52

9. Discussion
   - 9.1. Apatite of the Bégin-Lamarche (North and South Zone) as an ESG-compliant source of phosphate 56
   - 9.2. Cl content of (fluor)apatite of the Bégin-Lamarche (North and South Zone) 58
   - 9.3. Geological processes controlling the Cl content of (fluor)apatite of the Bégin-Lamarche (North and South Zone) 58
   - 9.4. Mineral paragenesis, the timing of apatite crystallization, and fluid evolution 59
   - 9.5. Ilmenite and magnetite as secondary commodities 63
   - 9.6. Use of mafic silicate minerals for CO_2 sequestration 63

10. Conclusions 64

11. Recommendations 65

12. References 66

1. Introduction

Electric vehicles (EVs) are considered a key green technology to reach a desirable reduction of global greenhouse gas emissions for tackling climate change (Trost and Dunn, 2023; Murdock et al., 2021; Liu et al., 2018). These EVs are mostly powered by four major types of rechargeable lithium-ion batteries (Li-ion batteries), which are lithium nickel cobalt aluminum oxide (NCA), lithium nickel manganese cobalt oxide (NMC), lithium manganese oxide (LMO), and lithium iron phosphate (LFP) batteries (Guimarães et al., 2023; Tran et al., 2021; Miao et al., 2019).

Among the four types of rechargeable batteries, recently the LFP battery demand has increased dramatically due to its technical superiorities over others (Ye et al., 2018; Li and Ma, 2019; Ahsan et al., 2021). Furthermore, supply risk and price volatility of raw materials, such as cobalt and nickel, for other rechargeable batteries have accelerated the demand for LFP batteries in the automobile industry (Helbig et al., 2018; Walvekar et al., 2022; Wang et al., 2023).

Phosphorus insecurity is becoming a major global issue in the food industry itself (Walsh et al., 2023) because the fertilizer industry dominates phosphate use globally (~85%; Spears et al., 2022). Now, the parallel demand for phosphorus or phosphate in the battery industry poses a potential competition for phosphate resources between EVs and the food industry (Lunde, 2022). The recent inclusion of the phosphate-bearing mineral, **apatite**, by the Quebec government (Government of Quebec, 2024), phosphorus by the Government of Canada (Government of Canada, 2024), and the earlier inclusions of phosphate and phosphorus by other countries, such as the European Union, Ontario in Canada, and Korea (European Commission, 2020; Government of Ontario, 2022) in their critical mineral lists also signify its high supply risk.

Sedimentary phosphate ore accounts for ~95% of the global reserve and 90% of global production (Pufahl and Groat, 2017). The sedimentary phosphate ore, however, contains a high amount of toxic heavy metals, such as cadmium (Cd), uranium (U), mercury (Hg), and lead (Pb) (Walsh et al.,2023). First Phosphate Corp. targeted anorthosite-hosted, environment-friendly igneous phosphate deposits (Banerjee, 2023a), which were rarely exploited previously for phosphate ore. Furthermore, First Phosphate Corp. is the only company developing greenfield phosphate deposits to source phosphate for the lithium iron phosphate (LFP; LiFePO4) battery industry.

2. Objectives and deliverables

A recent drilling program by First Phosphate reveals that mafic and ultramafic rocks from the Bégin-Lamarche property contain multiple cumulate layers of phosphatic ore (Fig. 1A-C). The detailed geological nature of the LSJA in the Bégin-Lamarche area is currently unknown. Detailed geological mapping around the deposit is currently underway through an MSc project of Jonathan Katako Diyoyo at UQAC, Quebec (Diyoyo et al., 2024).

Fig. 1. Location map (A, B, and C) showing the Bégin-Lamarche property of First Phosphate Corp., Quebec, Canada. The Lac à l'Orignal property of First Phosphate Corp. is also shown in panel C (panels B and C are modified from Google Maps, July 2, 2024).

The primary objective of collaborative research is to provide critical new information on the mineralogy and geochemistry of the North and South Zone of the Bégin-Lamarche deposit to fully assess its character and concentration of phosphate ore. This information is essential for site feasibility study, mine planning, and ore processing with the least environmental impact possible.

The primary objective of this study is to provide comprehensive mineralogical and geochemical information from 52 drill core samples collected from 21 drill holes from the North and South zones of the Bégin-Lamarche property.

Our collaborative research will yield the following key deliverables:

1) Comprehensive mineralogy and geochemical characterization of the North and South zones of the Bégin-Lamarche deposit (property).

2) Establish mineral paragenesis of the deposit.

3) Use of mineral paragenesis and geochemical characteristics to identify a tool to trace high-quality phosphate ore in the deposit.

3. Background

The production of lithium iron phosphate (LFP; $LiFePO_4$) battery requires pure phosphoric acid with low trace element concentrations (BM Review, 2022; Banerjee 2023a). The production of pure phosphoric acid requires high-quality phosphate concentrate with high P_2O_5 and low trace elements because trace elements of phosphate ore are mostly transferred to phosphoric acid during its production. There are no economically viable technologies to remove these heavy metals or trace elements from the ore (Walsh et al., 2023). Therefore, the purity of phosphoric acid ultimately depends on the purity of phosphate ore.

Globally, phosphate ore is supplied mostly from sedimentary rocks (~90%) and a small portion from igneous rocks (~10%; Pufahl and Groat, 2017). However, sedimentary phosphate ore contains a higher amount of trace elements than those of igneous phosphate ore (Pufahl and Groat, 2017; Ouabid et al., 2021 and references therein). Furthermore, sedimentary phosphate ore produces a phosphate concentrate with lower P_2O_5 after beneficiation than that produced from igneous phosphate ore (Steiner et al., 2015; Banerjee et al., 2024a). Presently, igneous phosphate ore is supplied from silica-undersaturated alkali intrusions and carbonatites from Russia, South Africa, Brazil, and Finland (Banerjee et al., 2024a).

No phosphate ore is, however, currently supplied from mafic-ultramafic rocks hosted in massif anorthosite or layered intrusions. The phosphate ore from massif anorthosites, such as the LSJA Suite, contains even lower trace elements than those from the carbonatites (Banerjee et al., 2024a). Hence, the phosphate ore from the massif anorthosite could produce a high-quality phosphoric acid with low levels of trace elements. Until now, three massif anorthosite-hosted phosphate deposits (First Phosphate's Lac à l'Orignal deposit, Investissement Québec and Yara

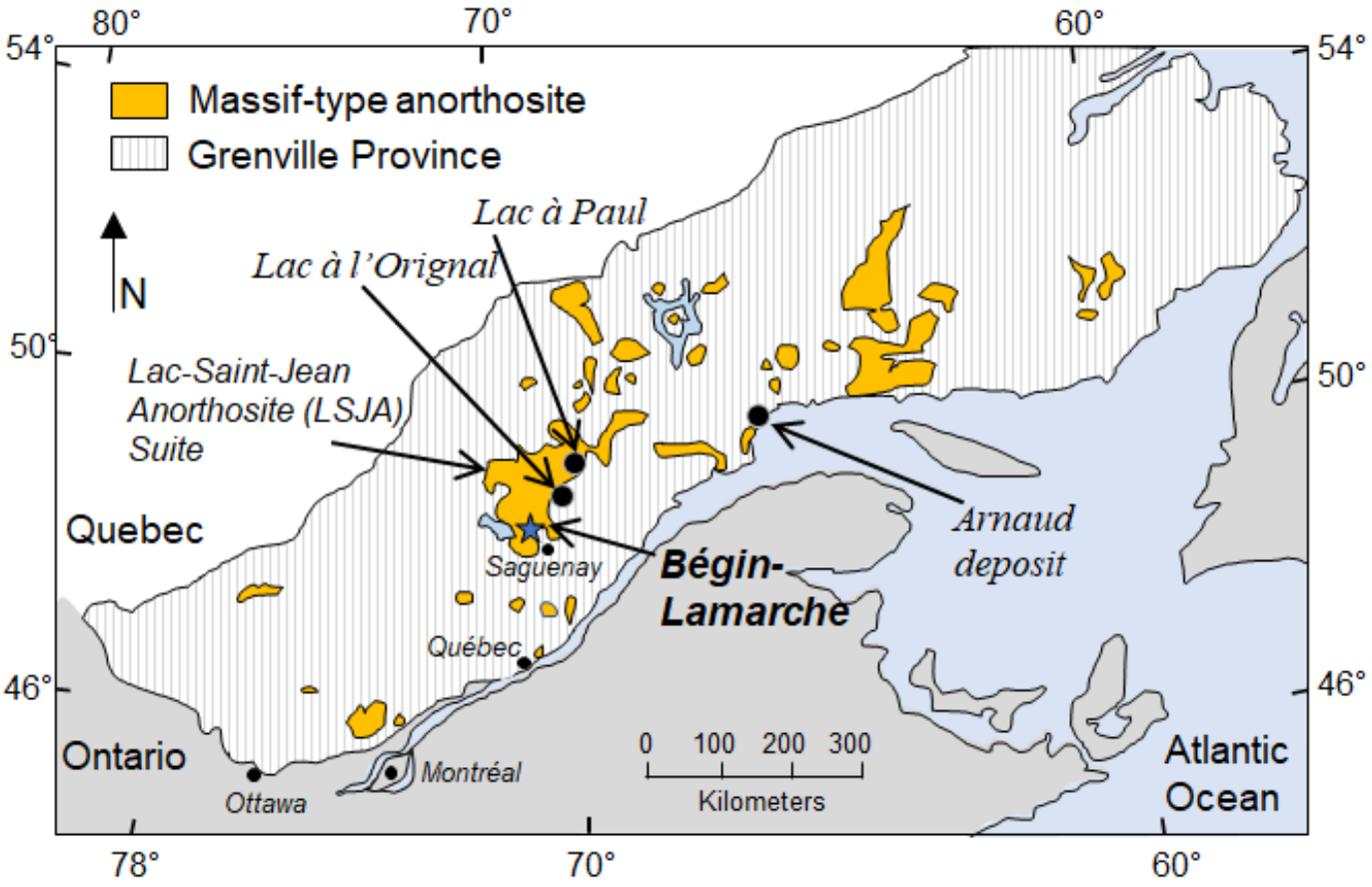

Fig. 2. Location map showing massif-type anorthosite bodies and the Bégin-Lamarche deposit, Quebec within the Grenville Province in Canada (modified after Banerjee et al., 2024b, Bédard, 2009; and Higgins et al., 2002). The three massif anorthosite-hosted phosphate deposits (Lac à l'Orignal, Arnaud, and Lac à Paul) evaluated for developing phosphate mines were also shown.

International's Arnaud deposit, and Arianne Phosphate's Lac à Paul deposit) from Québec, Canada were evaluated for developing phosphate mines (Fig. 2).

The average grade versus tonnage plot (Fig. 3) exhibits a wide range of sizes of igneous phosphate deposits, which are presently mined in Russia, South Africa, Brazil, and Finland. The deposits range from low-grade-low tonnage (e.g., Angico dos Dias, Brazil) to high-grade-high tonnage (e.g., Apatit's Kirovsk branch, Russia). The deposits that plot along a curvilinear line of Fig. 3 indicate that those deposits are expected to supply a similar amount of apatite (or P_2O_5) during the life span of the mines. For example, the First Phosphate's Lac à l'Orignal deposit plots close to the Angico dos Dias deposit, which suggests that if the Lac à l'Orignal deposit starts to supply phosphate ore, it will cumulatively supply a similar amount of apatite as that of the Angico dos Dias deposit during the life of the mine.

If the First Phosphate Corp. starts to mine phosphate ore from its Bégin-Lamarche property, the phosphate mine will be unique because it will be the ***first phosphate mine in Canada, as well as in the world, to supply phosphate ore from anorthosite massif-hosted rocks.***

4. Location

First Phosphate's Bégin-Lamarche property is located ~270 km north of Québec City, Quebec, Canada, and ~ 75 km northwest of Port Saguenay, Quebec (Fig. 1B). The property is part of the LSJA Suite (Fig. 2 and 4), the world's largest anorthosite massif (Ashwal, 1993, 2010).

The Bégin-Lamarche deposit is located on NTS sheets 22D11 and 22D14 (Fig. 4). The North Zone of the deposit is located at longitude 71.36° W and latitude 48.76° N (UTM NAD83 Zone 19N coordinates: 326,700 m E and 5,403,250 m N). The South Zone of the deposit is located at longitude 71.37° W and latitude 48.75° N (UTM NAD83 Zone 19N coordinates: 326,000 m E and 5,402,250 m N; Fig. 4 and 5).

5. Geological setting

5.1. Regional geology

The Bégin-Lamarche deposit is part of the LSJA Suite, which occurs in the central part of the Grenville Province (Fig. 2; Higgins and van Breemen, 1992). The Grenville Province is a ~1600 km long and ~350 km wide Mesoproterozoic orogenic belt along the southeastern margin of the Canadian Shield (Fig. 2). The Grenville Province contains numerous massif-type anorthosite, also called anorthosite-mangerite-charnockite-granite (AMCG) suites, including the LSJA Suite (Hébert et al., 2005).

The Grenville Province is a tectonically complex region that developed on the southeastern part of the Laurentia Paleocontinent (Carr et al., 2000; Corriveau et al., 2007; Rivers, 2012). The province resulted from a continent-continent collision between the southeastern margin of the Laurentia craton and the western margins of the Amazonian and Kalahari cratons (Jacobs et al., 2008; Ibanez-Mejia et al., 2011) over a period of ~340 million years. The collision

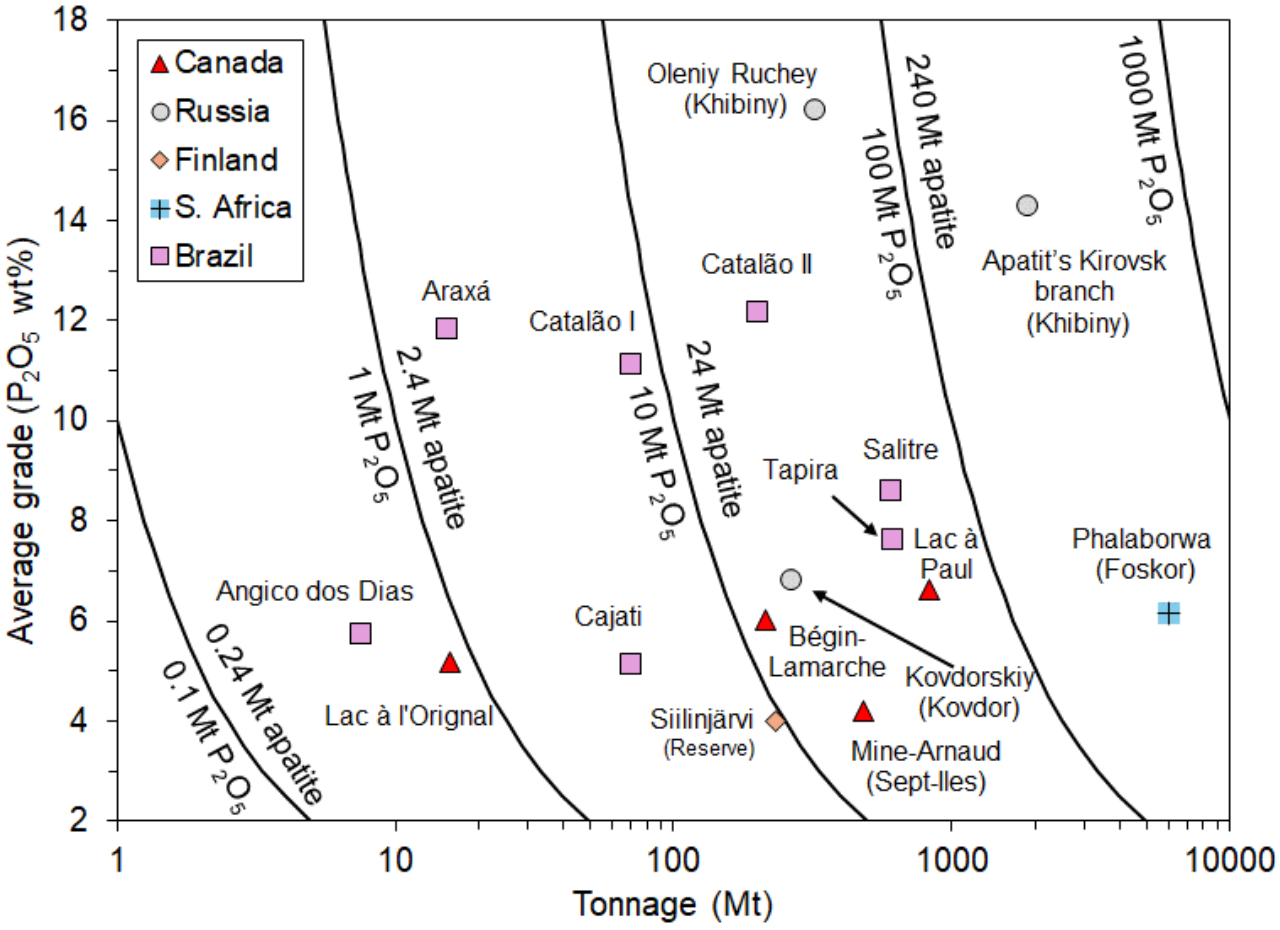

Fig. 3. Average grade versus tonnage (resource) for major igneous phosphate deposits from silica-undersaturated alkali and carbonatite intrusions from various countries around the world (modified after Banerjee et al., 2024a). The resources (tonnage) for Russian deposits (Oleniy Ruchey, Apatit's Kirovsk branch, and Kovdorskiy) are considered from the A+B+C1 reserve. Igneous phosphate deposits in Canada (prospective mines) hosted in oxide-apatite-mafic-ultramafic rocks within massif-anorthosites are also shown. Note that the tonnage (x)-axis is on a logarithmic scale. The curvilinear lines indicate the amount (Mt.) of P_2O_5 or apatite within the phosphate ore.

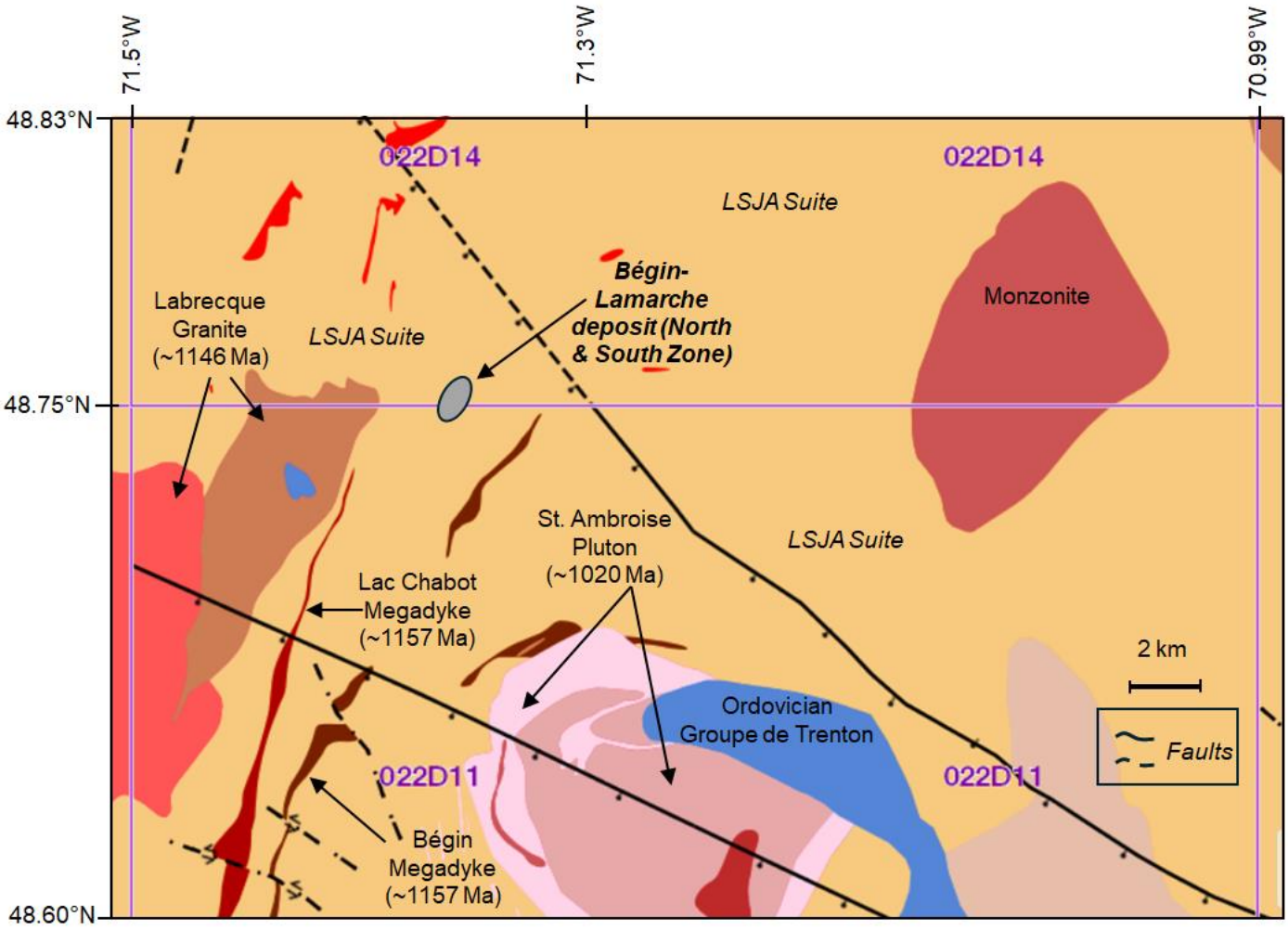

Fig. 4. Simplified location map of the Bégin-Lamarche deposit showing distributions of the Labrecque Granite, St. Ambroise Pluton, Bégin, and La Chabot megadykes within the LSJA Suite. The age data are within the parentheses and from Higgins and van Breemen (1996). Geological map modified after SIGEOM (Quebec System of Geomining Information; Hébert and Lacoste, 1998; Laurin and Sharma,1972; Intissar et al., 2021).

events occurred in three distinct phases (Shawinigan,1190–1140 Ma; Ottawan, 1080–1020 Ma; and Rigolet, 1000–980 Ma) and the phases were separated by periods of crustal extension and intra-plate volcanism (Rivers, 1997). The Himalayan-type continental collision during the Grenville Orogeny produced intense crustal thickening associated with high-grade metamorphism (amphibolite-granulite facies; Darling et al., 2004; Hynes and Rivers, 2010; Ludden and Hynes, 2000).

The LSJA Suite is the largest anorthosite body in the world (Ashwal, 1993, 2010). It consists of a complex assemblage of intrusive anorthosite plutons that are difficult to differentiate based on field relationships and mineralogy. Less abundant intrusive rocks include leuconorite, leucotroctolite, norite, olivine-bearing gabbro, gabbro, pyroxenite, peridotite, dunite, nelsonite, magnetitite, and rare charnockite–mangerite units (Hébert et al., 2005). Two large (> 30 km in length) north-northeast oriented mafic dykes (Lac Chabot and Bégin megadykes) were also reported from the LSJA Suite. All rocks including two large dykes composed of plagioclase with variable amounts of pyroxene and olivine (Higgins et al., 2002). Plagioclase is primarily of the andesine (An_{30}- An_{50}) and labradorite varieties (An_{50}-An_{70}; e.g., Hassen Ali et al., 2023; 2024; Diyoyo et al. 2024; Higgins and van Breemen, 1992). The plagioclase ranges in size from millimetric granoblastic crystals in deformed rocks to megacrysts of up to 70 cm long in less deformed rocks. Aluminum-rich orthopyroxene megacrysts are also locally abundant (Higgins and van Breemen, 1992).

The anorthositic rocks of the LSJA Suite are interpreted to have intruded in multiple phases over ~170 million years starting at ~1160 Ma (Higgins et al., 2002). The host rocks of the LSJA Complex are the Chicoutimi Gneiss Complex (~1530 Ma), the Saguenay Gneiss Complex (~ 1506 Ma), the Hulot Complex (~1434 Ma), the Cap à l'Est Gneiss Complex, and the Cyriac Rapakivi Granite (~1393 to 1383 Ma; Higgins and van Breemen, 1996; Hébert et al., 2005).

The U-Pb analyses of zircon and baddeleyite from the south-central and southeastern parts of the LSJA Suite provide an igneous crystallization age ranging from 1157 to 1142 Ma (Higgins et al., 2002). The eastern border of the suite (Vanel Anorthosite) is younger than the LSJA Suite and crystallized between 1082 and 1045 Ma (Higgins and van Breemen, 1996; Morisset et al., 2009). Other younger intrusions record periods of granitoid emplacement at 1028 and 988 Ma during the latter stages of the Grenville Orogeny (Higgins et al., 2002). When considered in the context of all geochronological data from the LSJA Suite region, these ages define three periods of magmatism recording a complex and protracted emplacement history. The first period occurred between 1160 and 1140 Ma, the second between 1082 and 1050 Ma, and the third between 1020 and 1000 Ma (Higgins and van Breemen, 1996).

Solid-state deformation of the LSJA Suite was extremely heterogeneous. Some plutons are undeformed, whereas others have transformed to grey gneiss. Syn-emplacement deformation fabrics and alteration features produced by contact metamorphism from later anorthosite plutons are also common (Higgins and van Breemen, 1992).

Multiple areas of phosphate or apatite mineralization are present in the anorthosite (or AMCG) massifs in the central part of the Grenville Structural Province (Banerjee et al., 2024b). In

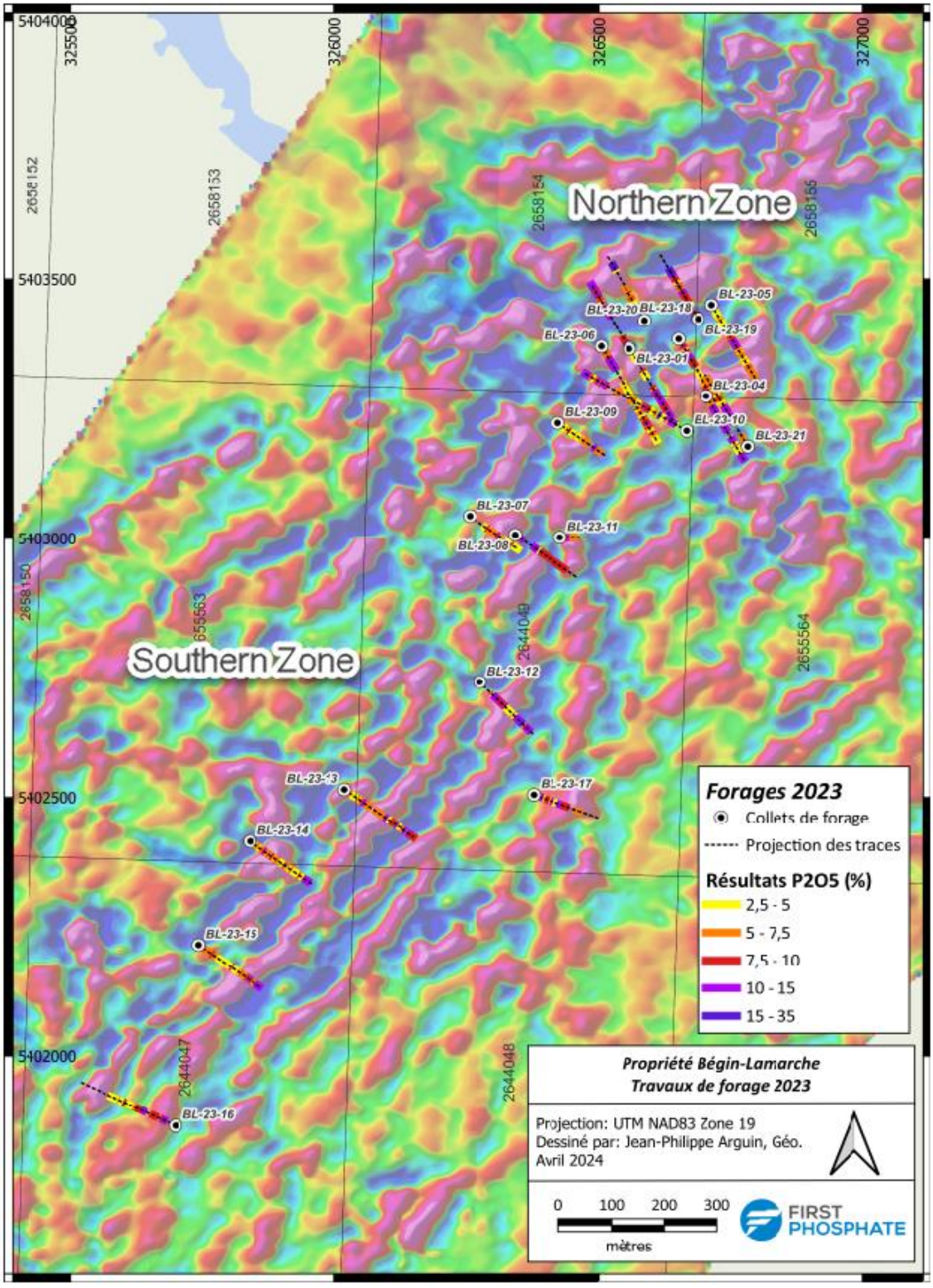

Fig. 5. Drill hole distributions within the North and South Zone of the Bégin-Lamarche property of First Phosphate Corp.

general, apatite mineralization occurs in the form of lenses, dykes, and small layered intrusions and is associated with Fe-Ti oxide minerals (Miloski et al., 2023; 2024; Hébert et al., 2005).

5.2. Local geology

The Bégin-Lamarche deposit is one of the phosphate deposits associated with Fe-Ti oxides within the LSJA Suite of the central Grenville Province (Fig. 2). The overall strike length of the North and South zones of the deposit is nearly 2000 m (First Phosphate press release, July 25, 2024). The deposit is proximate and parallel to the two megadykes (Lac Chabot (ferro)diorite and Bégin leucotroctolite megadykes of ~ 1157 Ma; Higgins and van Breemen, 1992; Fig. 4). The St. Ambroise Pluton (~1020 Ma) and the Labrecque Granite (~ 1146 Ma; Higgins and van Breemen, 1996) are on the east and west sides of the deposit, respectively (Fig. 4). Some nearly northwest oriented faults traverse the area and postdates the two north-northeast oriented megadykes.

The emplacement age of the First Phosphate's Bégin-Lamarche deposit has not been determined but may or may not be contemporaneous with the megadykes. Recently two phosphate deposits (Lac Mirepoix and Lac `a l'Orignal from the younger Vanel Anorthosite), ~75 km northeast of the Bégin-Lamarche, are dated between ~1070 and 964 Ma (Miloski et al. 2024; 2023), significantly younger than the two megadykes.

6. Sampling

A total of 52 drill core samples were collected from 21 drill holes from the North and South zones of the property (Fig. 5). Thirty-seven (37) samples were collected from drill hole BL-23-01 (n=3), BL-23-02 (n=3), BL-23-03 (n=2), BL-23-04 (n=2), BL-23-05 (n=2), BL-23-06 (n=2), BL-23-07 (n=6), BL-23-08 (n=1), BL-23-09 (n=3), BL-23-10 (n=3), BL-23-11 (n=2), BL-23-18 (n=1), BL-23-19 (n=3), BL-23-20 (2), and BL-23-21 (n=2) from the North zone. Fifteen (15) samples were collected from drill hole BL-23-12 (n=2), BL-23-13 (n=4), BL-23-14 (n=3), BL-23-15 (n=2), BL-23-16 (n=3), and BL-23-17 (n=1) from the South zone (Table 1 and appendix table A1),

The half-core samples were cut into halves to make quarters using a rock saw at the Department of Geological Sciences and Geological Engineering, Queen's University, Canada. Samples were used for petrographic, scanning electron microscopy (SEM), electron probe microanalysis (EPMA), and laser ablation inductively coupled plasma mass spectrometry (LA-ICP-MS) analysis (Table 1).

7. Methods

A total of 50 polished thin sections were prepared from the 52 core samples. Polished thin sections were studied under transmitted and reflected light using a Nikon Eclipse LV 100N microscope to identify minerals and their textural relationships.

Table 1. Core samples, with depths, of the 21 drill holes from the North and South zones of the Bégin-Lamarche property investigated in this study. Analysis type is also included.

Ser. no	bore hole	depth (m)	petrographic thin section	SEM (MLA)	EMPA	LA-ICP-MS
North zone						
LM1	BL-23-01	29.5	✓	✓	✓	✓
LM2	BL-23-01	68	✓	✓	✓	✓
LM3	BL-23-01	182.9	✓	✓		
LM4	BL-23-02	18.4	✓	✓		
LM5	BL-23-02	32.5	✓	✓		
LM6	BL-23-02	184.15	✓			
LM7	BL-23-03	171.7	✓	✓		
LM8	BL-23-03	195.4	✓			
LM9	BL-23-04	40.8	✓	✓		
LM10	BL-23-04	192	✓	✓		
LM11	BL-23-05	49.5	✓			
LM12	BL-23-05	143.7	✓	✓		
LM13	BL-23-06	63	✓	✓	✓	✓
LM14	BL-23-06	169.5	✓			
LM15	BL-23-07	71.35	✓	✓		
LM16	BL-23-07	73.5	✓	✓		
LM17	BL-23-07	98.8	✓	✓		
LM18	BL-23-07	103.7	✓	✓		
LM19	BL-23-07	112.15	✓	✓		
LM20	BL-23-07	116.5	✓	✓		
LM21	BL-23-08	84.2	✓	✓		
LM22	BL-23-09	20.5	✓			
LM23	BL-23-09	27.7	✓	✓		
LM24	BL-23-09	123.75				
LM25	BL-23-10	43.5	✓	✓		
LM26	BL-23-10	155.5	✓	✓	✓	✓
LM27	BL-23-10	310.6				

(Table 1 Continued)

Ser. no	bore hole	depth (m)	Petrographic thin section	SEM (MLA)	EMPA	LA-ICP-MS
North zone						
LM28	BL-23-11	33.7	✓	✓		
LM29	BL-23-11	35.5	✓	✓		
LM30	BL-23-18	139.6	✓			
LM31	BL-23-19	107.4	✓			
LM32	BL-23-19	307.2	✓	✓	✓	✓
LM33	BL-23-19	309	✓	✓		
LM34	BL-23-20	61.5	✓			
LM35	BL-23-20	81.75	✓	✓	✓	
LM36	BL-23-21	99.4	✓	✓		
LM37	BL-23-21	131.2	✓			
South zone						
LM38	BL-23-12	54	✓	✓	✓	✓
LM39	BL-23-12	112.5	✓	✓	✓	✓
LM40	BL-23-13	17.4	✓			
LM41	BL-23-13	30.1	✓	✓	✓	
LM42	BL-23-13	77.2	✓	✓		
LM43	BL-23-13	194.3	✓	✓		
LM44	BL-23-14	74	✓			
LM45	BL-23-14	106.7	✓	✓	✓	✓
LM46	BL-23-14	123.4	✓			
LM47	BL-23-15	77.5	✓			
LM48	BL-23-15	146.75	✓	✓		
LM49	BL-23-16	36.3	✓			
LM50	BL-23-16	43.5	✓	✓	✓	✓
LM51	BL-23-16	179.2	✓			
LM52	BL-23-17	25.1	✓	✓		
Total			***50***	***35***	***11***	***9***

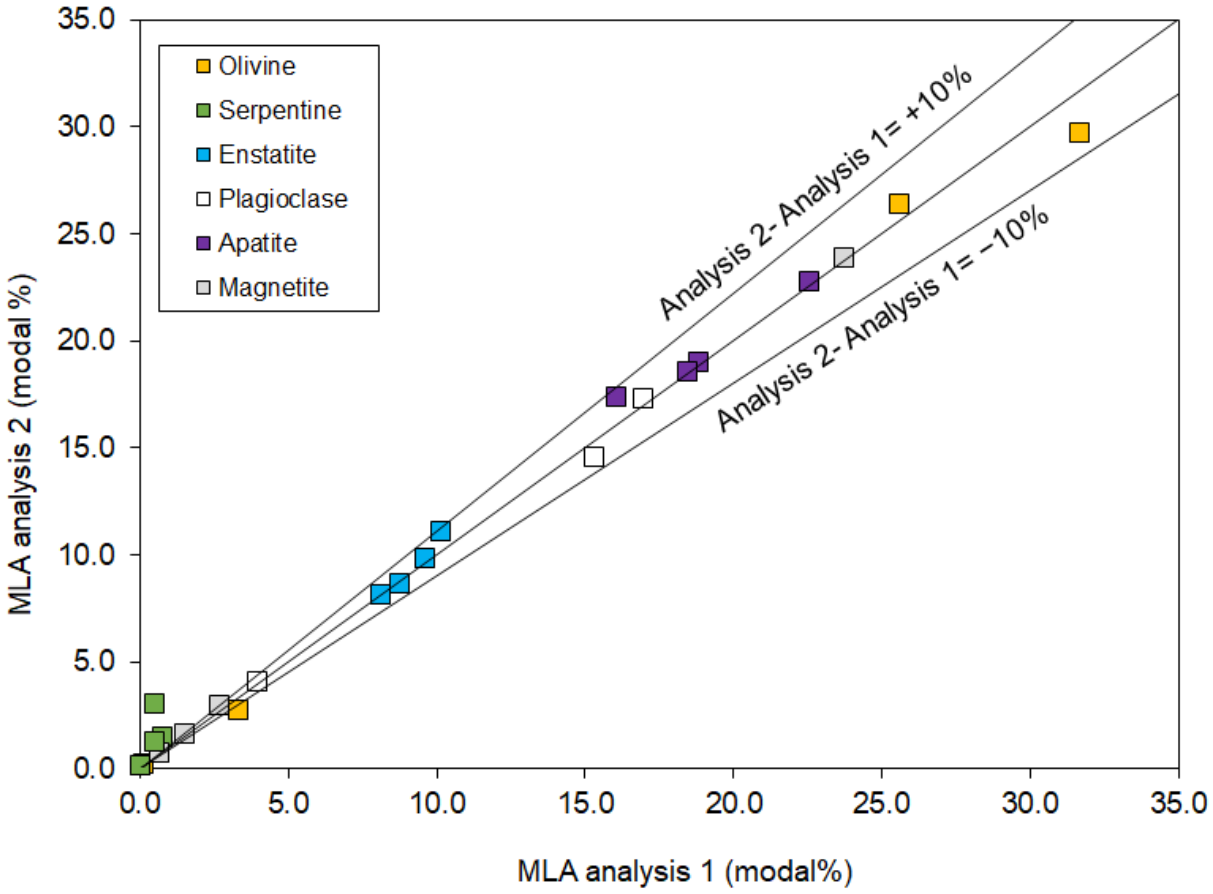

Fig. 6. Comparisons of duplicate analyses of modal abundances of minerals by MLA.

7.1. Mineral liberation analysis (MLA)

Thirty-five (26 from the North zone and 9 from the South zone; Table 1) of the 50 polished thin sections were analyzed with the FEI Quanta 650 FEG environmental scanning electron microscope (ESEM) utilizing the Mineral Liberation Analysis (MLA) to quantify mineral abundances in the samples. Samples were measured under a low vacuum at a chamber pressure of 10^{-5} torr. Energy-dispersive X-ray spectroscopy (EDS) was performed with two Bruker Nano Dual X-Flash detectors, using an accelerating voltage of 25kV and a working distance of 12 mm. Each sample was analyzed with a closely spaced grid of X-ray measurements overlaying a backscattered electron (BSE) image. Four of the thirty-five samples (~ 10%) were analyzed as duplicates as part of the quality control of the data (Table 2 and A2). The results of duplicate analyses indicate that the reproducibility of modal abundances of most of the minerals is better than 10% (Fig. 6). The analyses were performed at the Queen's Facility for Isotope Research (QFIR), Queen's University, Canada.

7.2. Electron-probe micro-analysis (EPMA)

In situ mineral compositions of major to minor elements (SiO_2, Al_2O_3, TiO_2, Cr_2O_3, FeO, MnO, MgO, CaO Na_2O, K_2O, P_2O_5, F, and Cl; Table 3) were determined on 11 polished thin sections (2 thin sections each from BL-23-01 and BL-23-12, and 1 thin section each from BL-23-06, BL-23-10, BL-23-19, BL-23-20, BL-23-13, BL-23-14, and BL-23-16; Table 1) for olivine (n=7 samples), orthopyroxene (n=10), plagioclase (n = 5), amphibole (n=8), biotite (n=9), apatite (n=11), ilmenite (n=11), magnetite (n=10), and Al-spinel (n=9).

The electron-probe micro-analyses were acquired on a fully automated JEOL JXA-iHP200F field emission electron microprobe at the University of British Columbia, Canada. All analyses used an accelerating voltage of 15 kV. A beam current of 20 nA for the analysis of olivine, pyroxene, ilmenite, magnetite, and Al-spinel, 15nA for the analyses of plagioclase, and 10 nA for the analysis of amphibole, biotite, and apatite were used. A beam diameter of 1 μm for the analysis of olivine, ilmenite, magnetite, and Al-spinel, 3 μm for pyroxene, 5 μm for plagioclase, 10 μm for amphibole, biotite, and apatite were used (Table A3). A linear background fit was used for all elements except for F. An exponential background fit was used for F. Interference corrections were applied to F and Cl for interference by Ce (Donovan et al., 1993). The reported data represent an average of three or more analyses of each mineral from different parts of each thin section (Table 3). Natural standards from the Smithsonian Institute were used for the analysis of all phases.

Electron-probe micro-analyses were also acquired for apatite crystals from six samples (LM1, LM13, LM16, LM 41, LM45, and LM 50), particularly for their F and Cl contents, at the QFIR, Queen's University. Five (LM1, LM13, LM 41, LM45, and LM 50) of them are repeat analyses, which were analyzed at the University of British Columbia. The duplicate analyses were performed at two laboratories to understand the quality (i.e., reproducibility) of F and Cl data using the EPMA method because the Cl content of apatite is crucial for this project. The analysis was performed on a JEOL JXA-8230 electron probe microanalyzer.

The apatite crystals with prismatic sections parallel to the c-crystallographic axis were identified under a petrographic microscope, and mineral compositions were analyzed from those

crystals because F and Cl migrate less along this crystallographic orientation during beam exposure of EPMA (e.g., Marks et al., 2012; Banerjee et al., 2024b). Apatite crystals were measured using a 15 kV acceleration voltage, a 15 nA beam current, and a defocused beam of 10 μm diameter. The defocused beam was used to limit F and Cl migration in apatite (e.g., Kieffer et al., 2023; Banerjee et al., 2024b). Decreasing the beam current (e.g., from 15 nA to 10 nA) can also limit the F and Cl migration (Mark et al., 2012). A defocused beam of 15 nA with a beam diameter of 10 μm, however, can substantially decrease the F and Cl migration (Kieffer et al., 2023; Banerjee et al., 2024b).

7.3. Laser ablation–inductively coupled plasma-mass spectrometry (LA-ICP-MS) analysis

In situ trace (and minor) element compositions were determined on a subset of 9 polished thin sections (2 thin sections from BL-23-01, and BL-23-12, and 1 thin section each from BL-23-06, BL-23-10, BL-23-19, BL-23-14, and BL-23-16) for olivine (n=5 samples), orthopyroxene (n=2), plagioclase (n = 3), apatite (n=8), ilmenite (n=9), and magnetite (n=8). A trace element is an element that is present in a rock or mineral in concentrations of less than 0.1 wt% or 1000 ppm (Rollinson, 2014). Depending on the mineral structure one element can be present as a major element in one mineral and the same element can be present as a trace element in another mineral.

Isotopes (^{24}Mg, ^{27}Al, ^{29}Si, ^{39}K, ^{44}Ca, ^{45}Sc, ^{47}Ti, ^{51}V, ^{52}Cr, ^{55}Mn, ^{57}Fe, ^{59}Co, ^{60}Ni, ^{63}Cu, ^{65}Cu, ^{66}Zn, ^{67}Zn, ^{71}Ga, ^{72}Ge, ^{75}As, ^{77}Se, ^{82}Se, ^{85}Rb, ^{88}Sr, ^{89}Y, ^{90}Zr, ^{93}Nb, ^{95}Mo, ^{111}Cd, ^{115}In, ^{118}Sn, ^{125}Te, ^{137}Ba, ^{139}La, ^{140}Ce, ^{141}Pr, ^{146}Nd, ^{147}Sm, ^{153}Eu, ^{155}Gd, ^{157}Gd, ^{159}Tb, ^{163}Dy, ^{165}Ho, ^{166}Er, ^{169}Tm, ^{172}Yb, ^{175}Lu ^{178}Hf, ^{206}Pb, ^{207}Pb, ^{208}Pb, ^{232}Th, ^{235}U, and ^{238}U) in these minerals were analyzed using a NWR-ESI 193nm ArF excimer laser system coupled to a Thermo Fischer TQs ICP-MS at QFIR. The laser reference glass standards NIST610, NIST 612, NIST 614, and BHVO-2G were used, whereas Durango apatite and BC-28 were used as matrix-matched reference materials to monitor the results. Spots on standards and reference materials were ablated before and after each set of samples and preferred values obtained from GeoReM were used for data reduction (Jochum et al., 2005, 2011). Before each spot analysis, a gas blank was measured for 20s to establish background values. A beam diameter of 35 μm with a laser repetition rate of 10 Hz was used for each spot. The total analyte measurement time was 1s with an average dwell time of 0.013s per mass. Laser energy was checked daily. Fluence on the samples was 5.1 J/cm^2. When choosing sites to ablate, care was taken to avoid visible inclusions in the crystals.

Data were reduced using the Iolite 4 software (Woodhead et al., 2007; Paton et al., 2011). Ablation spots were calibrated for each mineral to the standard reference material with the closest concentration and matrix type. All mineral groups were calibrated to the same reference material for each laser ablation session (Table A4). The precision and accuracy of the standards are provided in Table A5-A10. Data for olivine, orthopyroxene, and plagioclase were normalized using constant Si values (stoichiometric values). Similarly, apatite, ilmenite, and magnetite data were normalized using constant Ca, Ti, and Fe values, respectively. Although the elemental concentrations of minerals (e.g., Si for plagioclase and Fe for magnetite) from EPMA data could be used for the normalization for determining the trace element concentrations with higher accuracy. The use of stoichiometric values of the elements for the normalization will be adequate in this study to understand the elemental concentration distributions of each mineral from the

deposit. The reported data represent an average of analyses of each mineral from different parts of each thin section (Table 4 and A11-A21).

8. Results

8.1. Mineralogy and mineral chemistry of the Bégin-Lamarche deposit (North and South Zone)

The rock types comprising the LSJA Suite in the Bégin-Lamarche deposit exhibit a wide variation. The phosphatic ore mineral is apatite (specifically fluorapatite) but it is associated with a wide variety of mineral assemblages. The major minerals comprising the rocks are olivine (0-54 modal%), iddingsite + 'serpentine-type mineral' (0-25 %; alteration products of olivine), orthopyroxene (0-58 %), clinopyroxene (0-18 %), plagioclase (0-99 %), amphibole (0-68 %), biotite (0-36 %), chlorite (0-16 %), apatite (0-71 %), magnetite (0-27 %), ilmenite (0-24 %), and Al-spinel (0-5 %; Table 2). Carbonate (calcite; < 11 %) is also present in many samples, mostly in the form of veins. An orthoclase and quartz-rich vein was also identified from one sample (LM07). Furthermore, garnet is identified from one sample (LM45). Finally, sulfide minerals occur as an accessory phase (<1 %).

Depending on the modal abundances of the minerals, the rock types identified in this study are predominantly oxide and apatite-bearing mafic-ultramafic rocks, and anorthosite (Table 2; Fig 7A and B). The oxide-apatite prefix was used in the rock name only when the modal abundances of oxide and apatite were ≥ 5 %. Although apatite abundance is higher than that of the oxide minerals from the Bégin-Lamarche deposit, we considered the commonly used prefix 'oxide-apatite' for the nomenclature of these rocks. The ***oxide-apatite mafic rocks (plagioclase>10%)*** of the deposit include oxide-apatite gabbronorite (OAGN), oxide-apatite olivine gabbronorite (OAOGN), oxide-apatite olivine gabbro (OAOG), oxide-apatite olivine norite (OAON), oxide-apatite mela-norite (OAmN), oxide-apatite mela-olivine norite (OAmON), apatite-mela-olivine norite (AmON), apatite leuco-norite (AlN), and oxide-apatite leuco-troctolite (OAlT; Table 2, Fig. 7A). The ***oxide-apatite ultramafic rocks (~0% plagioclase)*** include oxide-apatite lherzolite (OAL), oxide-apatite dunite (OAD), oxide-apatite harzburgite (OAH), oxide-apatite olivine websterite (OAOW), oxide-apatite olivine orthopyroxenite (OAOO), and oxide-apatite orthopyroxenite (OAO) (Table 2, Fig. 7B). For the nomenclature of the rocks, the iddingsite + 'serpentine-type mineral' was considered as olivine because they are altered products of olivine (Fig. 7A and B).

Nelsonite (~2/3 of oxide minerals and ~1/3 of apatite; Philpotts, 1967) is a rock that contains only oxide minerals and apatite (i.e., devoid of silicate minerals). Therefore, *sensu stricto* nelsonite is not a dominant rock type in the Bégin-Lamarche deposit (Fig. 8A and B). The apatite (and oxide) predominantly present as semi-massive and disseminated forms (Fig. 8A). Furthermore, the abundances of oxide minerals of the Bégin-Lamarche deposit are relatively lower than that of combined silicate minerals and apatite (Fig. 8A), which is similar to the other two massif anorthosite-hosted phosphate deposits (Lac à l'Orignal, and Lac à Paul) in Quebec (Fig. 8A). Similar to the Lac à l'Orignal deposit, the oxide-apatite mafic-ultramafic rocks of the Bégin-Lamarche deposit contain significantly higher abundances of orthopyroxene relative to clinopyroxene (Fig. 8C, Table 2). The rocks from the Bégin-Lamarche deposit, however, contain

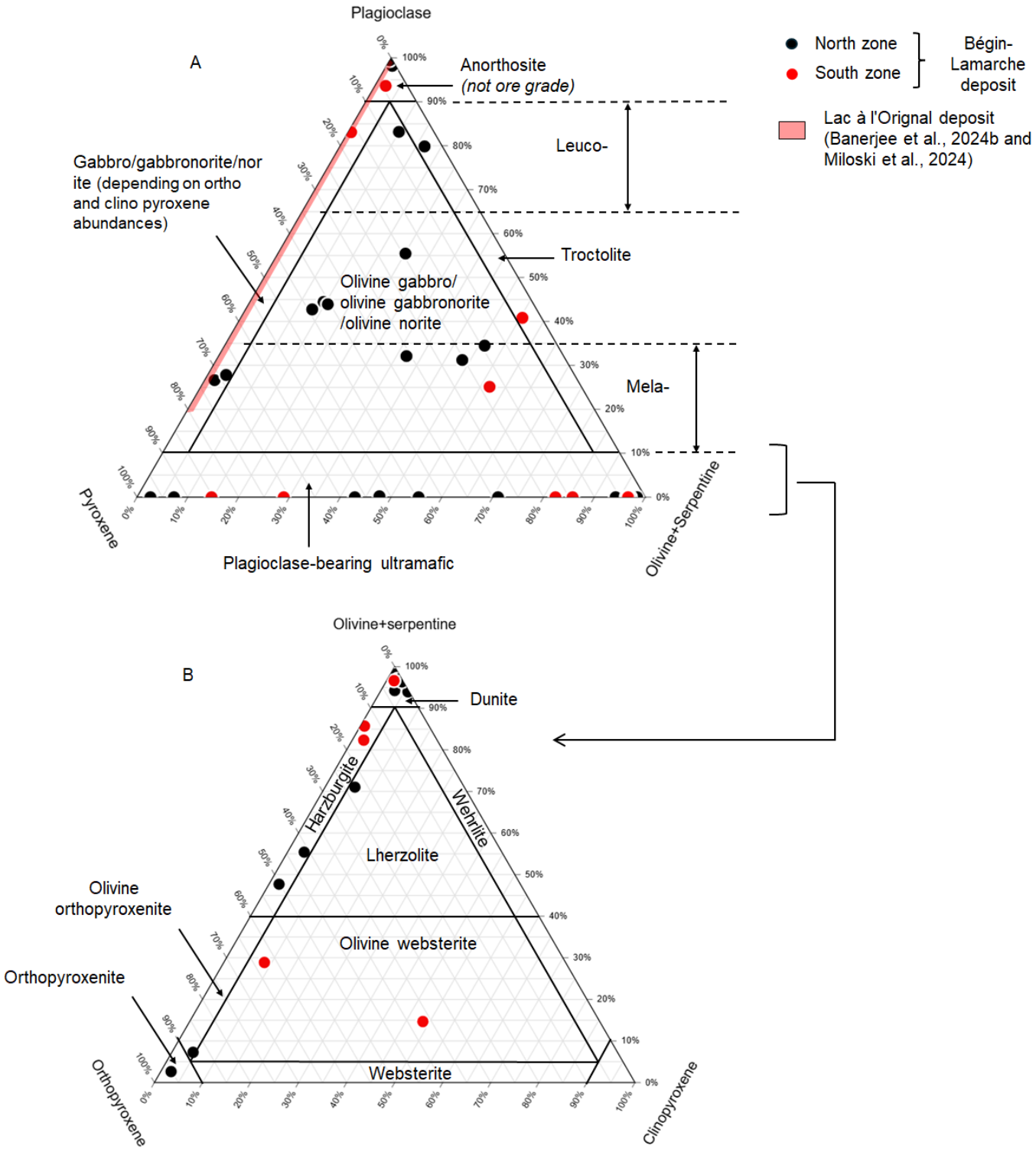

Fig. 7. Classification of oxide-apatite-mafic and ultramafic rocks of the Bégin-Lamarche deposit (North and South Zone). The distributions of plagioclase, pyroxene, and olivine+serpentine of the Lac à l'Orignal deposit are also shown in Fig. A

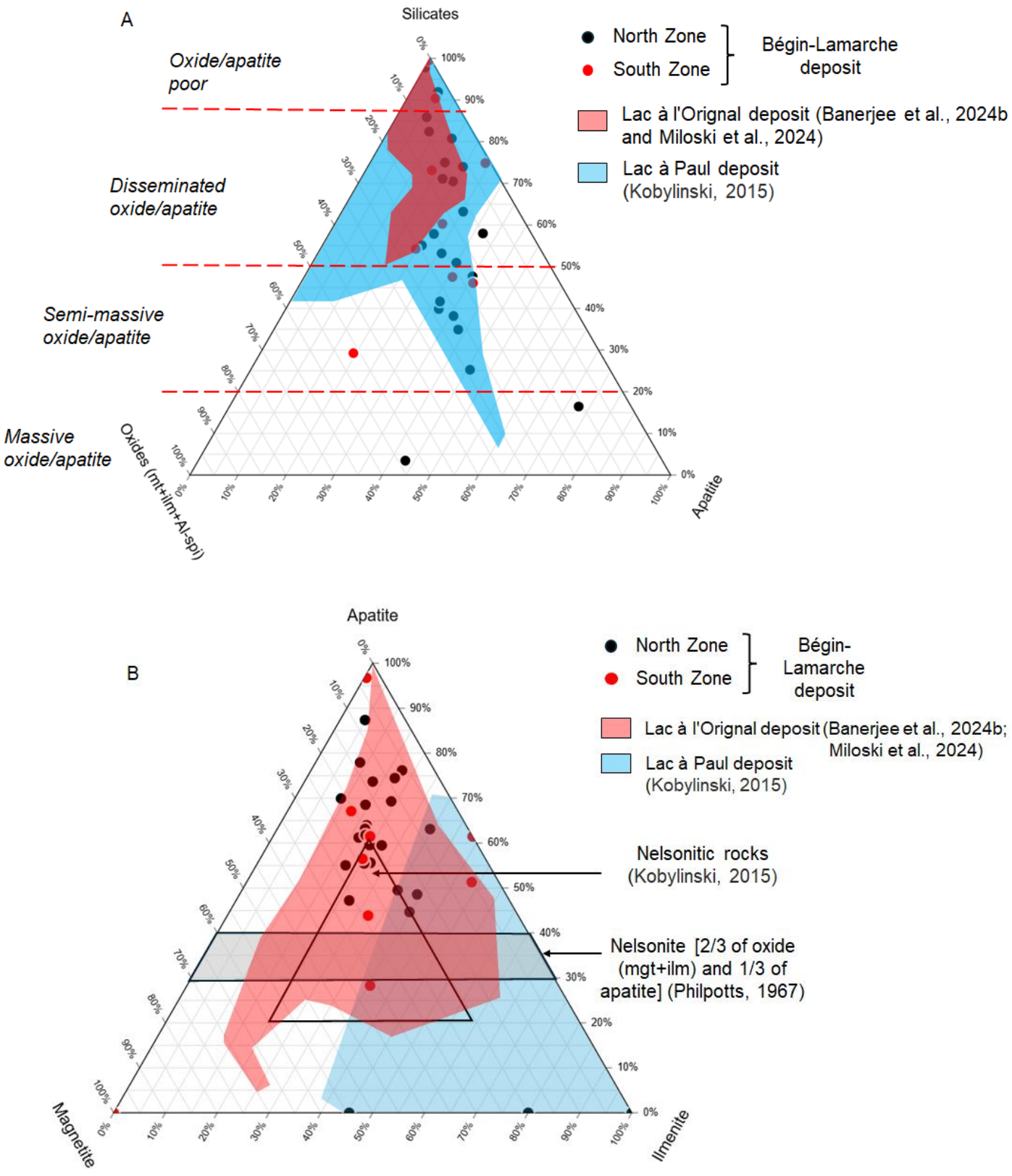
A
Silicates
Oxide/apatite poor
Disseminated oxide/apatite
Semi-massive oxide/apatite
Massive oxide/apatite
Oxides (mt+ilm+Al-spi)
Apatite
North Zone
South Zone
Bégin-Lamarche deposit
Lac à l'Orignal deposit (Banerjee et al., 2024b and Miloski et al., 2024)
Lac à Paul deposit (Kobylinski, 2015)
B
Apatite
Magnetite
Ilmenite
North Zone
South Zone
Bégin-Lamarche deposit
Lac à l'Orignal deposit (Banerjee et al., 2024b; Miloski et al., 2024)
Lac à Paul deposit (Kobylinski, 2015)
Nelsonitic rocks (Kobylinski, 2015)
Nelsonite [2/3 of oxide (mgt+ilm) and 1/3 of apatite] (Philpotts, 1967)

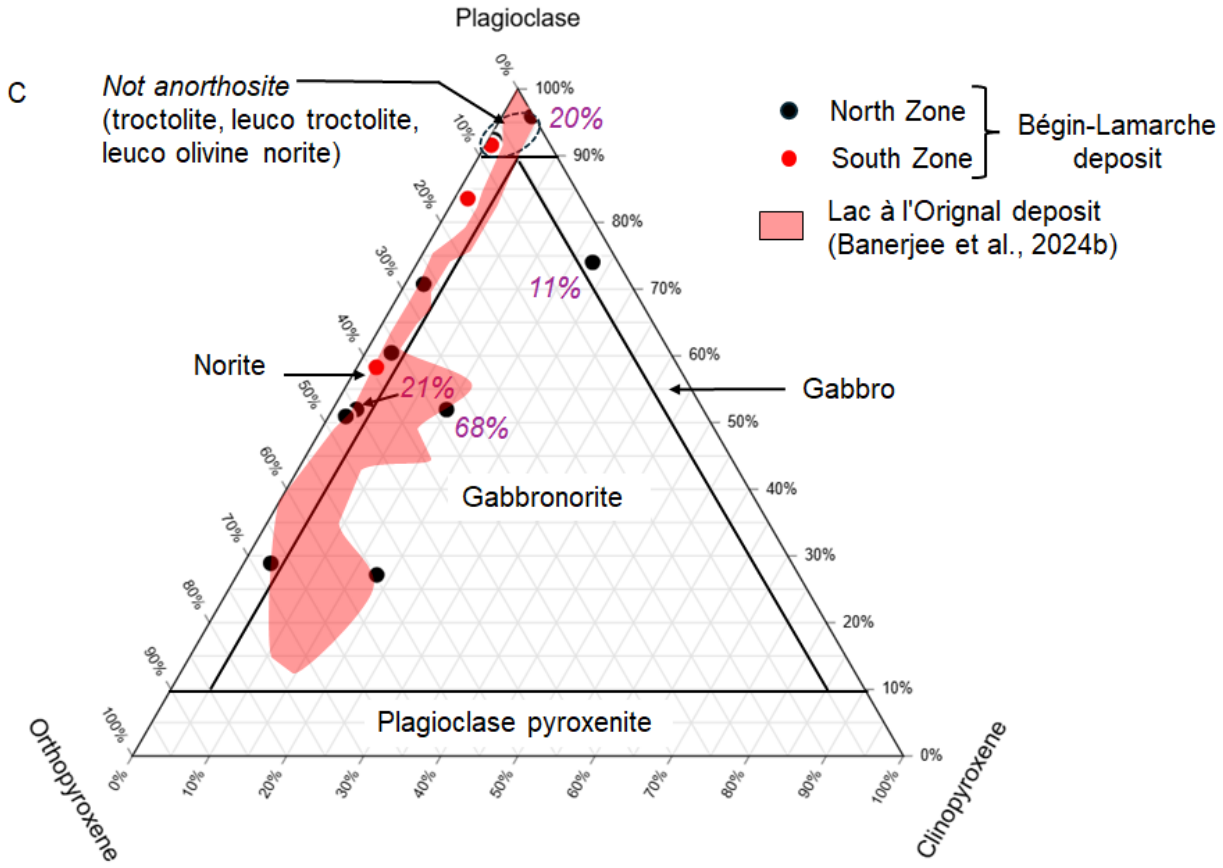

Fig. 8. Comparisons of anorthosite hosted oxide-apatite mafic and ultramafic rock types of three phosphate deposits (Bégin-Lamarche, Lac à l'Orignal, and Lac à Paul) in Quebec. Anorthosite and plagioclase-bearing ultramafic rocks from the Bégin-Lamarche deposit were not included in Figure C. High abundances (11-68 %) of amphibole for the four samples of the Bégin-Lamarche are also reported (in % values; in italic) in Figure C. Abbreviations: magnetite, mt; ilmenite, ilm; Al-spinel, Al-spi.

Table 2. Mineral distributions of rocks and rock types (nomenclature of rocks) from the Bégin-Lamarche deposit (North and South Zone) analyzed through MLA.

Sample	Olivine	Serpentine*	Orthopyroxene	Clinopyroxene	Plagioclase	Amphibole	Biotite	Chlorite	Apatite	Magnetite	Ilmenite	Al-spinel	Carbonate	Rock name	Name of oxide-apatite plag bearing ultramafic rocks
	Modal %														
North zone															
Drill hole BL-23-01															
LM01	8.8	1.5	3.3	0.9	0.0	0.3	0.7	0.5	70.6	6.3	3.9	0.5	2.8	oxide-apatite ultramafic	oxide-apatite lherzolite (OAL)
LM02	0.8	0.2	0.3	0.3	86.7	4.7	4.0	0.7	0.0	1.2	1.0	0.0	0.1	anorthosite (Anr)	
LM03	29.5	13.3	1.3	1.3	0.0	0.1	0.0	1.5	34.4	8.6	7.2	1.4	1.5	oxide-apatite ultramafic	oxide-apatite dunite (OAD)
Drill hole BL23-02															
LM04	25.6	9.7	0.1	0.5	0.0	0.1	0.2	1.6	35.5	12.4	11.7	1.8	0.8	oxide-apatite ultramafic	oxide-apatite dunite (OAD)
LM05	3.7	0.6	8.5	3.8	13.2	68.1	0.3	0.4	0.0	0.0	0.4	0.0	0.9	altered norite or gabbronorite (N/ GN)	
Drill hole BL-23-03															
LM07	30.9	1.0	12.3	1.1	20.5	1.6	1.8	1.1	19.4	3.3	5.3	1.3	0.4	oxide-apatite mela-olivine norite (OAmON)	
Drill hole BL-23-04															
LM09	11.7	1.1	9.5	0.8	0.0	0.2	0.2	1.5	45.3	13.6	11.9	3.4	0.7	oxide-apatite ultramafic	oxide-apatite harzburgite (OAH)
LM10	10.5	25.1	0.1	2.2	0.0	0.2	0.0	1.6	31.7	12.9	12.4	2.9	0.4	oxide-apatite ultramafic	oxide-apatite dunite (OAD)
Drill hole BL-23-05															
LM12	54.1	1.4	0.6	0.4	0.0	0.0	0.1	1.3	21.8	9.4	8.1	2.8	0.1	oxide-apatite ultramafic	oxide-apatite dunite (OAD)
Drill hole BL-23-06															
LM13	36.9	18.3	0.5	1.2	0.0	0.1	0.3	0.4	31.8	5.5	3.5	1.0	0.4	oxide-apatite ultramafic	oxide-apatite dunite (OAD)
Drill hole BL-23-07															
LM15	7.6	1.0	21.2	1.5	24.5	8.0	3.8	6.8	15.4	1.8	7.2	0.3	0.8	oxide-apatite olivine norite (OAON)	
LM16	0.2	0.1	8.3	2.7	4.1	21.1	35.6	0.7	19.5	1.6	4.5	0.0	1.6	oxide-apatite gabbronorite (OAGN)	
LM17	2.5	0.3	34.0	1.7	0.0	0.6	0.5	1.8	31.0	15.6	9.7	1.7	0.7	oxide-apatite ultramafic	oxide-apatite olivine orthopyroxenite (OAOO)
LM18	8.3	0.9	26.7	4.3	30.0	5.6	3.1	1.2	14.0	1.6	3.2	0.2	0.8	oxide-apatite olivine gabbronorite (OAOGN)	
LM19	21.0	1.8	24.0	1.0	0.1	2.1	0.3	0.4	29.8	9.4	8.0	1.7	0.4	oxide-apatite ultramafic	oxide-apatite harzburgite (OAH)
LM20	7.4	0.7	0.1	1.6	38.8	20.0	16.0	1.2	6.3	2.9	4.9	0.0	0.2	oxide-apatite leuco troctolite (OAIT)	

(Table 2 continued)

Sample	Olivine	Serpentine*	Orthopyroxene	Clinopyroxene	Plagioclase	Amphibole	Biotite	Chlorite	Apatite	Magnetite	Ilmenite	Al-spinel	Carbonate	Rock name	Name of oxide-apatite plag bearing ultramafic rocks
						Modal %									
North zone															
Drill hole BL-23-08															
LM21	17.1	0.2	1.7	11.7	38.2	11.4	1.2	0.6	8.5	3.0	6.0	0.0	0.4	oxide-apatite olivine gabbro (OAOG)	
Drill hole BL-23-09															
LM23	15.7	0.2	12.7	0.6	13.8	6.0	2.0	3.8	20.6	8.5	12.5	3.1	0.5	oxide-apatite olivine norite (OAON)	
Drill hole BL-23-10															
LM25	17.9	4.2	5.6	0.5	14.9	4.3	1.9	3.7	25.7	8.0	9.5	3.5	0.2	oxide-apatite olivine norite (OAON)	
LM26	7.9	0.2	5.0	0.5	67.6	3.9	4.5	1.6	5.6	1.0	1.0	0.4	0.8	apatite leuco olivine norite (AlON)	
Drill hole BL-23-11															
LM28	0.2	0.3	0.0	0.8	0.0	0.2	0.3	1.5	41.1	26.9	19.0	5.1	4.6	nelsonite	
LM29	0.0	0.0	0.2	0.3	91.5	1.8	3.5	1.9	0.0	0.1	0.4	0.0	0.3	anorthosite (Anr)	
Drill hole BL-23-19															
LM32	1.0	0.6	57.6	1.3	0.0	1.8	0.2	0.4	25.1	7.6	3.2	0.6	0.5	oxide-apatite plag bearing ultramafic	oxide-apatite orthopyroxenite (OAO)
LM33	0.0	0.0	0.0	0.0	98.6	0.0	0.6	0.3	0.0	0.0	0.0	0.0	0.5	anorthosite (Anr)	
Drill hole BL-23-20															
LM35	1.6	0.7	41.3	2.1	17.6	4.6	1.5	1.2	16.9	6.1	4.6	1.1	0.6	oxide-apatite mela-norite (OAmN)	
Drill hole BL-23-21															
LM36	20.2	11.4	0.1	1.1	0.0	0.1	0.0	1.6	38.0	12.6	10.9	2.9	0.8	oxide-apatite ultramafic	oxide-apatite dunite (OAD)
South zone															
Drill hole BL-23-12															
LM38	38.1	2.1	6.3	0.4	0.0	0.1	0.0	0.4	30.8	9.9	9.4	2.4	0.1	oxide-apatite ultramafic	oxide-apatite harzburgite (OAH)
LM39	0.4	0.1	12.1	1.4	68.7	3.8	3.8	0.1	5.9	0.0	3.7	0.0	0.0	apatite leuco-norite (AlN)	
Drill hole BL-23-13															
LM41	25.4	2.1	5.1	0.8	0.0	3.6	1.6	15.3	19.7	13.0	12.2	0.5	0.6	oxide-apatite ultramafic	oxide-apatite harzburgite (OAH)
LM42	2.0	3.5	13.8	18.2	0.0	6.1	0.4	9.9	20.0	8.4	7.0	0.2	10.6	oxide-apatite ultramafic	oxide-apatite olivine websterite (OAOW)
LM43	49.8	1.7	3.2	0.3	38.0	2.3	3.4	0.3	0.0	0.2	0.0	0.2	0.4	troctolite (T)	

(Table 2 continued)

Sample	Olivine	Serpentine*	Orthopyroxene	Clinopyroxene	Plagioclase	Amphibole	Biotite	Chlorite	Apatite	Magnetite	Ilmenite	Al-spinel	Carbonate	Rock name	Name of oxide-apatite plag bearing ultramafic rocks
						Modal %									
South zone															
Drill hole BL-23-14															
LM45	0.8	0.1	0.9	0.9	39.7	8.9	5.9	15.8	13.7	1.4	11.6	0.0	0.3	oxide-apatite metagabbro/norite (OAmG/N)	
Drill hole BL-23-15															
LM48	31.4	3.1	10.3	0.7	15.3	4.4	3.8	5.7	24.0	0.7	0.1	0.2	0.1	apatite mela-olivine norite (AmON)	
Drill hole BL-23-16															
LM50	33.8	3.4	0.7	0.6	0.0	0.1	2.2	4.8	35.5	10.9	6.5	0.5	1.0	oxide-apatite ultramafic	oxide-apatite dunite (OAD)
Drill hole BL-23-17															
LM52	2.8	1.3	8.9	1.2	0.0	0.3	7.0	7.6	19.2	24.7	24.0	2.1	0.9	oxide-apatite ultramafic	oxide-apatite olivine websterite (OAOW)
Duplicate analysis															
LM07	25.6	0.8	10.2	0.9	17.0	1.3	1.5	0.9	16.1	2.7	4.4	1.1	0.4		
LM07_Dup	26.3	1.5	11.0	0.9	17.2	1.4	1.2	0.9	17.3	2.9	4.6	1.2	0.3		
LM16	0.2	0.0	8.2	2.7	4.0	20.4	34.8	0.7	18.9	1.5	4.3	0.0	1.6		
LM16_Dup	0.2	0.1	8.1	2.7	4.0	20.5	34.7	0.7	19.0	1.6	4.4	0.0	1.6		
LM48	31.7	0.5	9.7	0.6	15.4	4.1	3.6	5.4	22.6	0.7	0.1	0.2	0.1		
LM48_Dup	29.7	3.0	9.7	0.6	14.5	4.2	3.6	5.4	22.7	0.7	0.1	0.2	0.0		
LM52	3.4	0.6	8.8	1.1	0.0	0.3	6.8	7.6	18.5	23.8	23.1	2.0	0.9		
LM52_Dup	2.7	1.2	8.6	1.1	0.0	0.2	6.8	7.3	18.5	23.8	23.2	2.0	0.9		

* They are not truly serpentine [$Mg_3Si_2O_5(OH)_4$]. They contain significant amounts of iron (FeO~ 18.6-35.6 wt%) (Table A12).

Modal abundances of these minerals are normalized to 100%.

Sulfide mineral abundances are <1%.

'Oxide and or apatite' prefix was used when the modal abundances of oxide and apatite were ≥ 5 %.

both olivine and (ortho+clino) pyroxene unlike the Lac à l'Orignal deposit, which is devoid of olivine (Fig. 7A).

Most core samples exhibit alternating phaneritic leucocratic (light-colored) and melanocratic (dark-colored) layers. The leucocratic layers are mostly composed of plagioclase and the melanocratic layers are formed of mafic silicate (olivine, pyroxene, amphibole, and biotite) and oxide minerals (ilmenite and magnetite). All rock types exhibit cumulate texture.

It is important to note that the interpretations of the mineralogy, petrology, and geochemical data are based on a small set of samples of the deposit. Furthermore, it is also obvious that samples from each set of rock types (Table 2) are also very limited. Therefore, all rocks are grouped as a single group, i.e., oxide-apatite mafic and ultramafic rocks, for the simplicity of description in this study. A description of the petrographic and geochemical characteristics of individual minerals composing the Bégin-Lamarche deposit is provided below.

Olivine (Mg_2SiO_4-Fe_2SiO_4): Olivine (0-54 modal%) is one of the major mafic minerals of the deposit (Fig. 9A-F). The mineral is subhedral to anhedral in shape (Fig. 9A-C). The crystals range in size from ~0.1 to 4 mm. The crystals are typically fractured (Fig. 8A). The fractures are filled with "serpentine" like minerals (Fig. 9D). However, electron-probe micro-analysis indicates that they are not truly serpentine [$Mg_3Si_2O_5(OH)_4$]. They contain significant amounts of iron (FeO~ 18.6-35.6 wt%; Table A12). Many olivine crystals are altered to iddingsite (Fig. 9E). In some samples, olivine crystals exhibit triple junction crystal boundaries (Fig. 9F) suggesting crystal boundary migration during recrystallization (Ragan, 1969). Finally, late-stage veinlets (of 'serpentine' like minerals) are also observed to cross-cut iddingsite crystals (Fig. 9E).

Olivine has end-member compositions of forsterite (Mg_2SiO_4; 47.2-58.8 mol% Fo) and fayalite (Fe_2SiO_4; 41.2-52.8 mol% Fa; Table 3). The magnesium number [Mg# = Mg/ (Mg + Fe^{2+})] of olivine (47.2-58.8) is similar to their forsterite contents (47.2-58.8 mol%), which is typical for olivine. The Mg# of mafic silicate minerals is an indicator of the degree of magmatic differentiation, (Zieg and Wallrich, 2018), i.e. the extent of magmatic crystallization (early *vs* late stage crystallization). There is little variability in SiO_2 (34.4-35.9 wt.%), MnO (0.5-0.6 wt.%), and CaO ($\leq$0.04 wt.%) contents (Table 3).

Common trace elements include Ca (133-501 ppm), Zn (93-591 ppm), Co (180-243 ppm), Ni (59-101 ppm), Ti (7-39 ppm), and Al (1-17 ppm; Fig. 10, Table 4). The REE (rare earth elements; also described later in section 8.2) contents of the olivine crystals are very low (< instrumental LOD, Table 4).

Orthopyroxene ($Mg_2Si_2O_6$-$Fe_2Si_2O_6$): Orthopyroxene (0-58 %) is another dominant mafic silicate mineral of the deposit (Fig. 11 A-F). The crystals are mostly subhedral and range in size from ~0.1 to 3 mm. The crystals sometimes contain oxide mineral inclusions (Fig 11A). Orthopyroxene crystals are associated with oxide minerals (Fig. 11A), plagioclase, clinopyroxene (Fig. 11B), and apatite, (Fig. 11B-D). The association of orthopyroxene with amphibole (Fig. 11E) and alteration of orthopyroxene to amphibole are also observed in a few samples. Furthermore, the presence of (ortho/clino) pyroxene surrounding olivine and amphibole

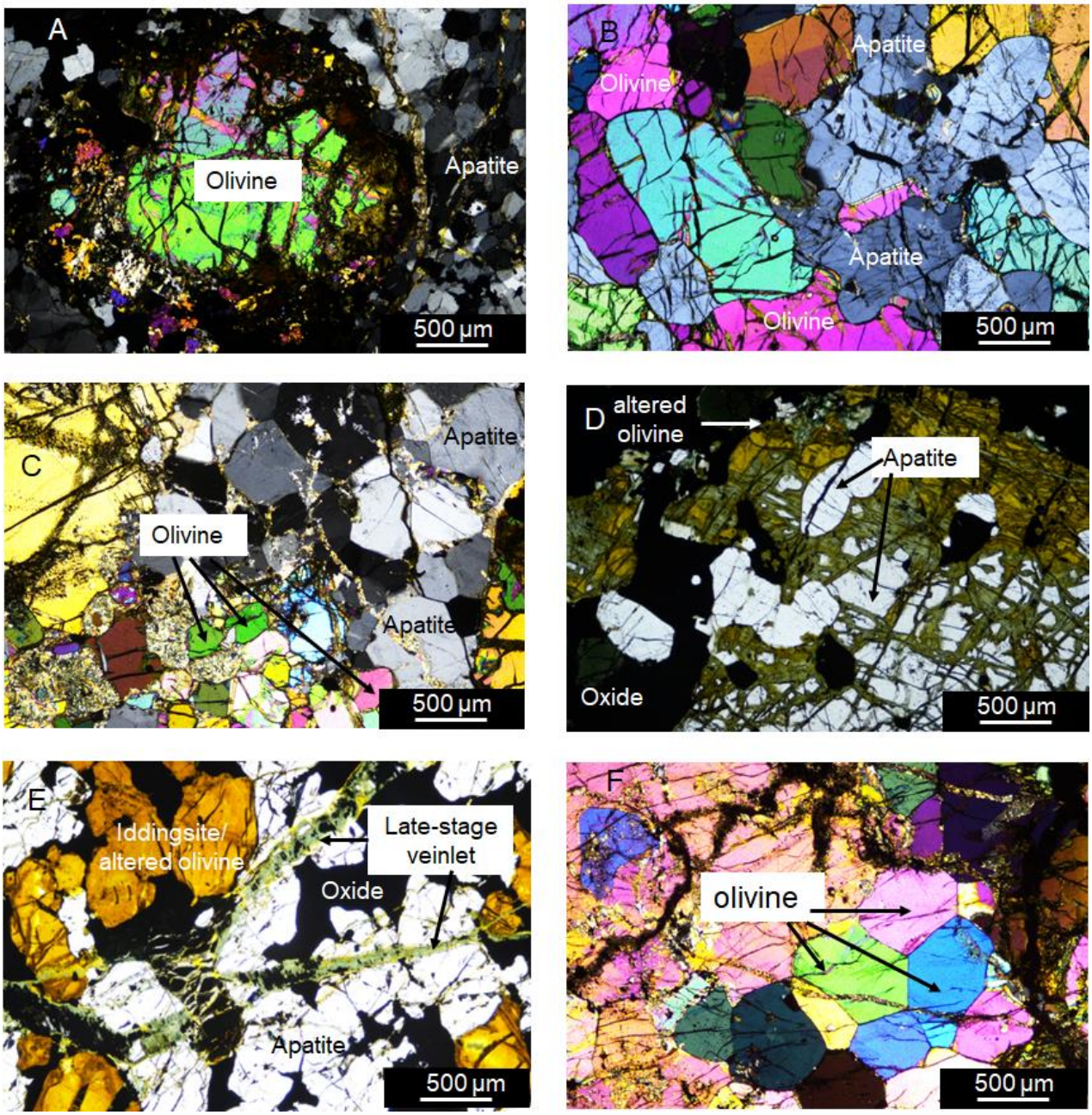

Fig. 9. Textural relationships of olivine from the Bégin-Lamarche deposit (under transmitted light). (A) Fractured olivine crystal surrounded by apatite (sample LM1; cross-polarized light); (B) Cumulate texture of olivine and apatite (sample LM12; cross-polarized light); (C) Small size crystals of olivine associated with larger size apatite crystals (sample LM8; cross-polarized light); (D) Altered olivine associated with apatite and oxide minerals (sample LM4; plane-polarized light); (E) Iddingsite (altered olivine) associated with apatite and oxide minerals; late-stage veinlets cross cut iddingsite and apatite (sample LM4; plane-polarized light); (F) Olivine crystals with straight triple junction crystal boundaries (LM8; cross-polarized light).

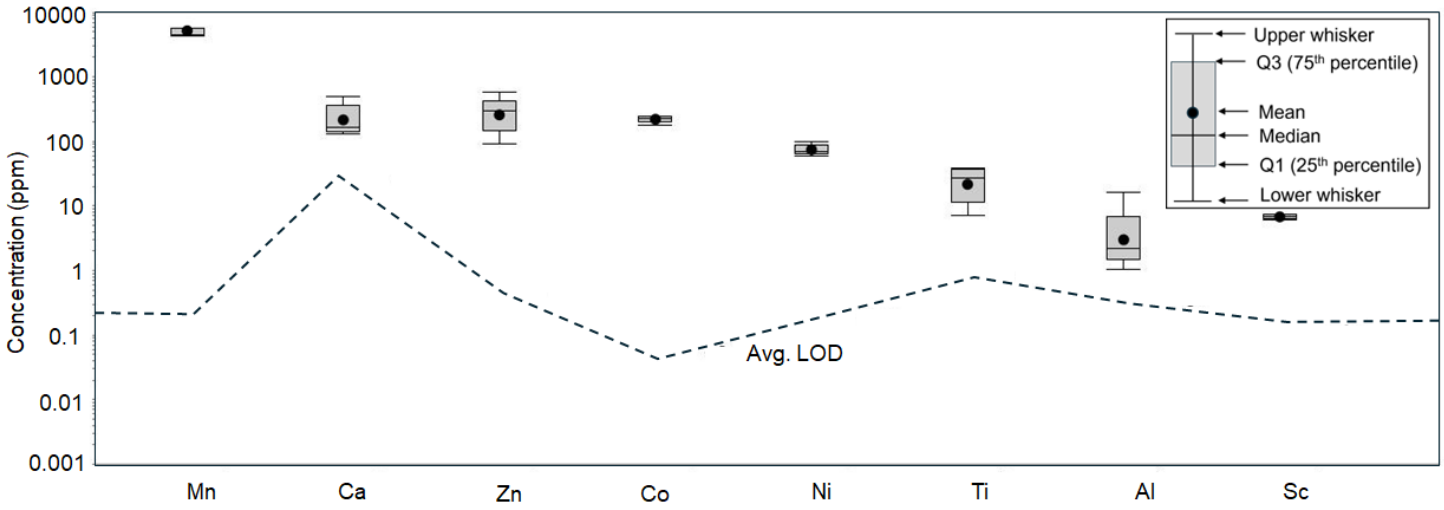

Fig. 10. Concentrations of selected trace (and minor) elements in olivine (n=7 samples) of the Bégin-Lamarche deposit (North and South Zone). The less than LOD values (<LOD) are replaced by LOD/2. The elements are arranged by their decreasing concentrations.

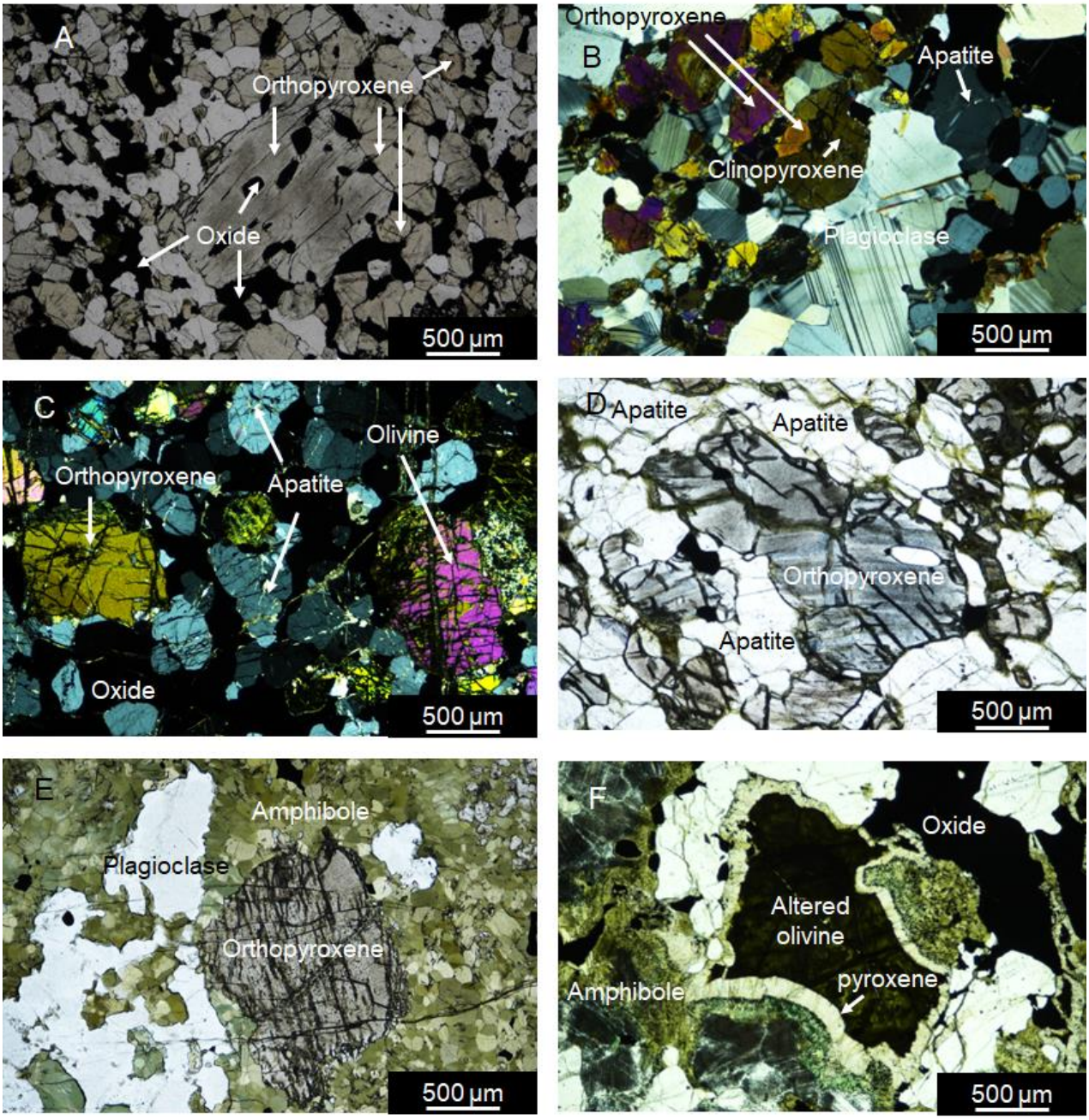

Fig. 11. Textural relationships of orthopyroxene from the Bégin-Lamarche deposit (under transmitted light). (A) Orthopyroxene crystals associated with oxide minerals (sample LM17; plane-polarized light); oxide minerals are also present as inclusions within orthopyroxene; (B) cumulate texture of orthopyroxene, clinopyroxene, and plagioclase (sample LM39; cross-polarized light); (C) Orthopyroxene crystals associated with olivine, apatite, and oxide minerals (sample LM25; cross-polarized light); (D) Orthopyroxene crystal surrounded by apatite crystals (sample LM6; plane-polarized light); (E) Orthopyroxene crystal surrounded by amphibole crystals (sample LM5; plane-polarized light) and (F) Corona structure where (ortho/clino) pyroxene forms a band around altered olivine and amphibole forms band around the pyroxene (sample LM31; plane-polarized light).

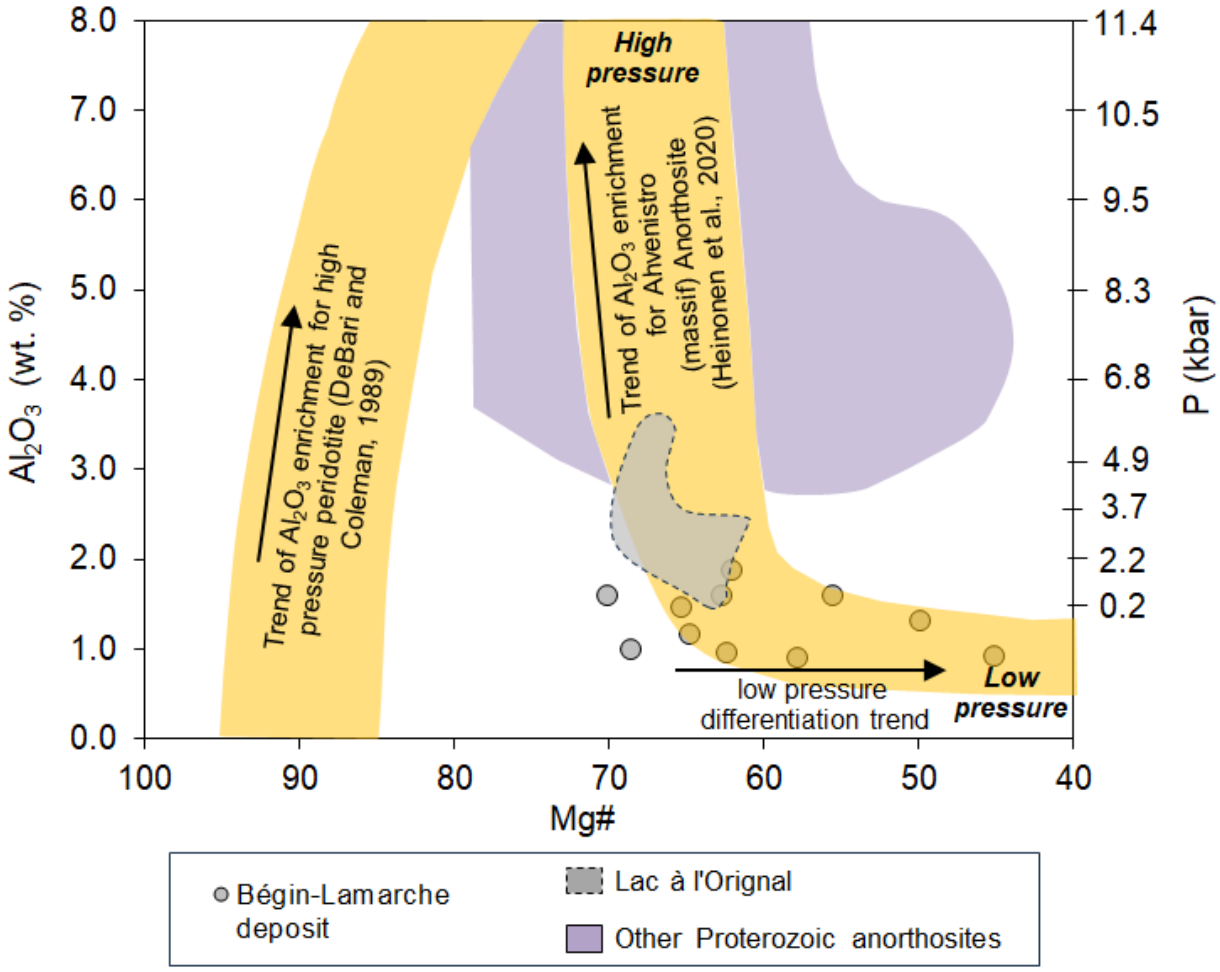

Fig. 12. Relationships between Al_2O_3 content and Mg# of orthopyroxene in the oxide-apatite-mafic-ultramafic rocks of the Bégin-Lamarche deposit (North and South Zone). Orthopyroxene from the Lac à l'Orignal deposit (Banerjee et al., 2024b; Miloski et al., 2024; Grant, 2020) and other Proterozoic anorthosites (Mealy Mountains Intrusive Suite, Nain Plutonic Suite, Canada; Bybee et al., 2014; Rogaland Anorthosite Province, Norway, Bybee et al., 2014; Charlier et al., 2010) are also shown. The Mg# of orthopyroxene from Miloski et al. (2024) and Grant (2020) are calculated from their FeO_{total} and MgO data of orthopyroxene. The pressures of orthopyroxene crystallization were calculated using the Al content of orthopyroxene from the Ahvenisto Anorthosite, Finland (Heinonen et al., 2020) according to the geobarometeric relationship of Emslie et al. (1994).

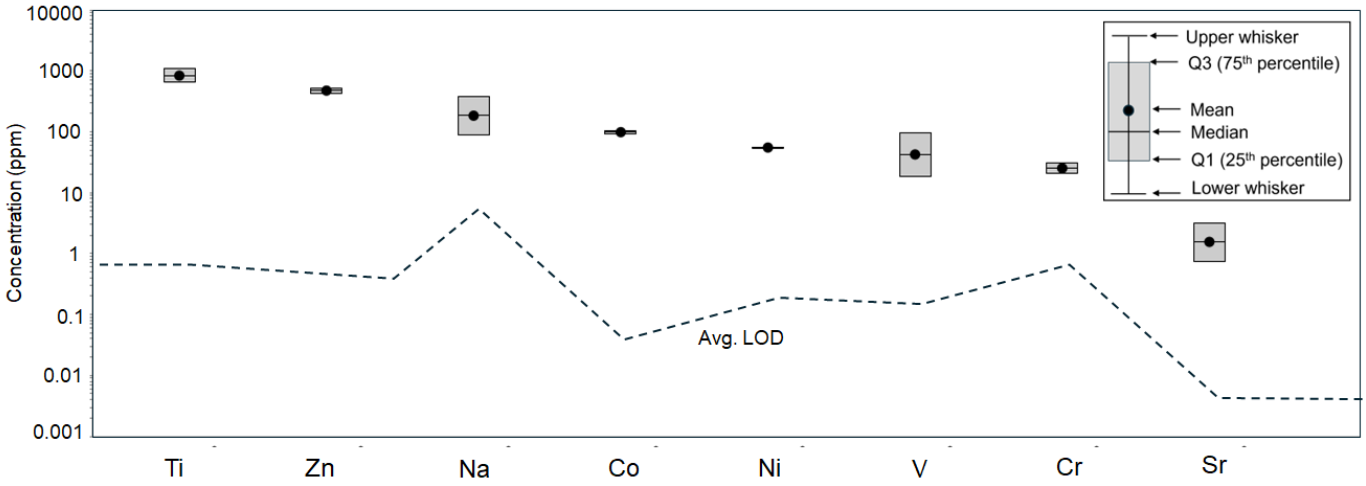

Fig. 13. Concentrations of selected trace elements in orthopyroxene (n= 2 samples) of the Bégin-Lamarche deposit (North and South Zone). The less than LOD values (<LOD) are replaced by LOD/2. The elements are arranged by their decreasing concentrations.

Table 3. Abundances and chemical compositional ranges of minerals in oxide-apatite mafic and ultramafic rocks from the North and South Zone of the Bégin-Lamarche deposit analyzed by EPMA.

	Olivine	Orthopyroxene	Plagioclase	Amphibole	Biotite	Apatite	Ilmenite	Magnetite	Al-spinel
	modal abundance (%)								
Modal (%)	0-54	0-58	0-99	0-68	0-36	0-71	0-24	0-27	0-5%
# (n) of spot	n=74	n=88	n=53	n=38	n=31	n=115	n=114	n=106	n=45
	(wt%)								
SiO_2	34.4-35.9	50.5-55.3	56.7-60.8	40.3-48.9	35.0-41.5	0.0-0.2	0.0-0.01	0.01-0.11	0.0-0.08
Al_2O_3		0.9-1.9	24.7-26.9	7.4-15.6	14.6-17.2		0.01-1.7	0.31-0.85	57.8-60.5
TiO_2		0-0.2		0.4-1.5	0.4-4.3		49.7-52.5	0.15-1.36	0.02-0.2
Cr_2O3	0-0.01	0-0.02		0.0-0.02	0.0-0.04		0.01-0.02	0.01-0.16	0.0-0.2
FeO	35.4-43.2	17.3-32.4	0.09-0.14	9.8-22.5	6.8-20.9		45.2-49.2	91-92.6	22.8-33.8
Fe_2O_3									
MnO	0.5-0.6	0.4-0.9		0.02-0.2	0.02-0.06	0.02-0.17	0.4-0.9	0.0-0.07	0.14-0.35
MgO	21.7-28.3	14.9-24.5	0.0-0.03	0.02-0.2	10.0-24.1		0.3-1.5	0.01-0.15	3.3-9.4
ZnO	0.02-0.04	0-0.1					0.01-0.06	0.01-0.03	0.7-6.8
CaO	0-0.04	0.1-0.9	6.4-9.2	6.8-12.2	0.01-0.11	54.8-55.7	0.01-0.05	0-0.08	0.0-0.03
Na_2O	0-0.03	0-0.4	6.4-8.2	0.7-3.3	0.04-3.1	0.03-0.1			
K_2O			0.04-0.19	0.1-0.7	3.9-10.3				
P_2O_5						41.4-41.8			
F						1.67-3.4 (16700-34000 ppm)			
Cl				0.02-0.21	0.02-0.29	0.04-0.5 (400-5000 ppm)			
H_2O				1.7-2.9	4.1-6.5	0.4-1.4			
X^{Ap}_{FAp} (mole fraction of fluorapatite)						0.442-0.91			
X_{hem} (mole fraction of hematite in ilmenite							0.0-0.06		
Mg#	47.2-58.8	45.0-70.0		42.6-75.6	46.1-86.3				
End members	$Fo_{47.2-58.8}$ $Fy_{41.2-52.8}$	$En_{44.7-69.7}$ $Fs_{29.9-54.7}$ $Wo_{0.1-2.1}$	$An_{30.2-44.0}$ $Ab_{55.6-69.6}$ $Or_{0.2-1.1}$						

Table 4. Ranges of trace (and minor) element compositions of minerals from oxide-apatite mafic and ultramafic rocks from the North and South Zone of the Bégin-Lamarche deposit analyzed by LA-ICP-MS.

	Olivine	Orthopyroxene	Plagioclase	Apatite	Ilmenite	Magnetite
#(n) of spot	43	9	27	48	61	42
	(ppm)					
Na	<LOD	89-380	-	288-727	<LOD	<LOD
Mg	-	-	228-1065	235-2352	1924-12361	476-4385
Al	1.1-16.6	4101-5094	-	3.8-214	83-367	13784-23041
Si	-	-	-	429-1602	1346-5637	1688-13242
Ca	133-501	2210-2950	-	-	<LOD	<LOD
Sc	6.1-7.4	21.4-23.9	7.9-9.8	<LOD	9.6-61.7	<LOD
Ti	7.1-39.3	649-1071	155-376	64-133	-	1106-20493
V	<LOD	18.6-96.1	2.9-20.8	<LOD	131-1073	2115-6560
Cr	<LOD	20.5-30.9	<LOD	<LOD	12.8-87.3	415-989
Mn	4229-5663	4078-5107	8.9-63.5	182-1473	3683-6755	144-1097
Fe	-	-	633-2181	1230-5247	-	-
Co	180-243	93.1-104.0	<LOD	0.5-3.4	73.2-195	128-389
Ni	59.2-101	54.4-55.6	<LOD	0.6-1.3	7.1-48.6	86.7-600
Zn	92.8-591	429-523	1.8-7.9	<LOD	37.4-440	14.2-2196
Ga	<LOD	2.8-5.8	22.9-26.4	5.6-28.3	0.7-22.7	150-366
Ge	2.6-5.0	3.6-4.7	1.2-1.8	11.1-45.1	2.1-6.6	18.0-52.8
As	<LOD	<LOD	<LOD	3.0-8.8	<LOD	<LOD
Rb	<LOD	<LOD	<LOD	<LOD	<LOD	<LOD
Sr	<LOD	0.8-3.2	1114-1358	409-1053	0.3-1.0	0.4-6.5
Ba	<LOD	<LOD	164-300	<LOD	<LOD	<LOD
Zr	<LOD	0.4-2.4	<LOD	<LOD	3.0-80.7	<LOD
Nb	<LOD	<LOD	<LOD	<LOD	1.5-82.2	<LOD
Mo	<LOD	<LOD	<LOD	<LOD	0.6-6.7	2.8-28.3
Cd	<LOD	<LOD	<LOD	<LOD	<LOD	<LOD
Sn	<LOD	<LOD	<LOD	<LOD	1.3-5.5	<LOD
Pb	<LOD	<LOD	0.8-2.5	0.3-10.6	<LOD	<LOD
Th	<LOD	<LOD	<LOD	<LOD	<LOD	<LOD
U	<LOD	<LOD	<LOD	<LOD	<LOD	<LOD

(Table 4 continued)

	Olivine	Orthopyroxene	Plagioclase	Apatite	Ilmenite	Magnetite
	(ppm)					
REE+Y						
La	<LOD	<LOD	2.0-2.7	85.2-263	<LOD	<LOD
Ce	<LOD	<LOD	3.3-5.4	509-1115	<LOD	<LOD
Pr	<LOD	<LOD	0.4-0.6	82-140	<LOD	<LOD
Nd	<LOD	<LOD	0.9-2.5	410-613	<LOD	<LOD
Sm	<LOD	<LOD	<LOD	92.4-135	<LOD	<LOD
Eu	<LOD	<LOD	1.5-2.5	18.1-31.9	<LOD	<LOD
Gd	<LOD	<LOD	<LOD	82.2-129	<LOD	<LOD
Tb	<LOD	<LOD	<LOD	9.0-15.9	<LOD	<LOD
Dy	<LOD	<LOD	<LOD	43.7-88.5	<LOD	<LOD
Ho	<LOD	<LOD	<LOD	7.2-15.5	<LOD	<LOD
Er	<LOD	<LOD	<LOD	15.3-37.8	<LOD	<LOD
Tm	<LOD	<LOD	<LOD	1.4-3.8	<LOD	<LOD
Yb	<LOD	<LOD	<LOD	6.5-21.1	<LOD	<LOD
Lu	<LOD	<LOD	<LOD	0.9-2.8	<LOD	<LOD
Y	<LOD	0.5-3.2	<LOD	191-429	<LOD	<LOD
∑REE	<LOD	<LOD	8.0-14.2	1567-2599	<LOD	<LOD

Note: If the majority of any elemental concentration data of a mineral are < LOD (lower limit of detection), the data are reported as < LOD. The average concentration of each element of each mineral is provided in the Appendix tables.

surrounding orthopyroxene in the form of a corona structure (Fig 11E) is observed in a few samples, which is typical in anorthosite massifs (Woussen et al. 1981).

Orthopyroxene has end-member compositions of enstatite ($Mg_2Si_2O_6$, 44.7-69.7 mol.%), ferrosilite ($Fe_2Si_2O_6$, 29.9-54.7 mol.%), and wollastonite ($CaSiO_3$, 0.1-2.1 mol.%). The Mg# of orthopyroxene exhibits a wide variation (45-70). The Al_2O_3 (0.9-1.9 wt.%), MnO (0.4-0.9 wt%), Na_2O (≤0.4 wt%), and TiO_2 (≤0.2 wt%) contents of orthopyroxene are low (Table 3). The Al_2O_3 contents (0.9-1.9 wt %; Table 3) of orthopyroxene do not show any correlation with their Mg# (45–70; Fig. 12), which is typical of orthopyroxene crystallized in mid- to low-pressure intrusions (DeBari and Coleman, 1989; Helmy et al., 2014; Kharbish et al., 2022; Banerjee et al., 2024b). In the case of polybaric crystallization, the Al_2O_3 content of orthopyroxene decreases with decreasing pressure of crystallization (Fig. 12).

Common trace elements include Ti (649-1071 ppm), Zn (429-523 ppm), Na (89-380 ppm), Co (93-104 ppm), V (19-96 ppm), Ni (54-56 ppm), Cr (21-31 ppm) and Sr (1-3 ppm; Fig. 13, Table 4). Similar to the olivine, REE contents of the orthopyroxene are very low (< instrumental LOD, Table 4).

Clinopyroxene [(Ca,Mg,Fe) (Mg,Fe)Si_2O_6]: The abundances of clinopyroxenes (0-18 %) are significantly lower than that of orthopyroxenes (Fig. 8C and 14A-B). Clinopyroxene crystals, like orthopyroxene, are mostly subhedral. The crystals range in size from ~0.1 to 2 mm and are generally associated with orthopyroxene (Fig. 13A) and plagioclase cumulates (Fig. 14B).

Clinopyroxene (number of analysis = 1 sample) is of the diopside variety with end member compositions of wollastonite (47 mol.%), enstatite (40.2 mol.%), and ferrosilite (12.8 mol.%). The Mg# of clinopyroxene (75.8) is higher than that of orthopyroxene (45-70). The Al_2O_3 (0.66 wt.%), Na_2O (0.29 wt.%), and TiO_2 contents (0.06 wt.%, Table A14) are, however, low, similar to those of orthopyroxene. Trace elements were not analyzed for clinopyroxene.

Plagioclase ($NaAlSi_3O_8$ – $CaAl_2Si_2O_8$): Plagioclase crystals (Fig. 15A-F) of the rock types reported in this study exhibit a wide variation (e.g., ~0 % in ultramafic rocks, 4-69 % in mafic rocks, and 87-91% in anorthosite). The crystals range in size from ~ 0.2 to 4 mm. Equant crystals of plagioclase are common. Plagioclase crystals are mostly associated with orthopyroxene (Fig. 15A), olivine (Fig. 15B), clinopyroxene (Fig. 15C), apatite (Fig. 15D), amphibole, and biotite (Fig. 15E). In some cases, inclusions of olivine are also observed within plagioclase (Fig 15A). The granoblastic texture of plagioclase crystals with serrated crystal boundaries is interpreted to be the consequence of dynamic recrystallization (Fig. 15F).

All plagioclase crystals are of andesine variety with end member compositions of anorthite ($CaAl_2Si_2O_8$; 30.2-44.0 mol.%), albite ($NaAlSi_3O_8$; 55.6-69.6.1 mol.%), and orthoclase ($KAlSi_3O_8$; 0.2-1.1 mol.%). The SiO_2 (56.7-60.8 wt.%) and Al_2O_3 (24.7-26.9 wt.%) contents have narrow ranges (Table 3).

Common trace elements include Sr (minor element, 1114-1358 ppm), Fe (633-2182 ppm), Mg (228-1065 ppm), Ti (155-376 ppm), Ba (164-300 ppm), Mn (9-64 ppm), V (3-21 ppm), Zn (2-8 ppm), and Pb (1-3 ppm; Fig. 16, Table 4). The REE contents of the plagioclase are low (8-14 ppm; Table 4).

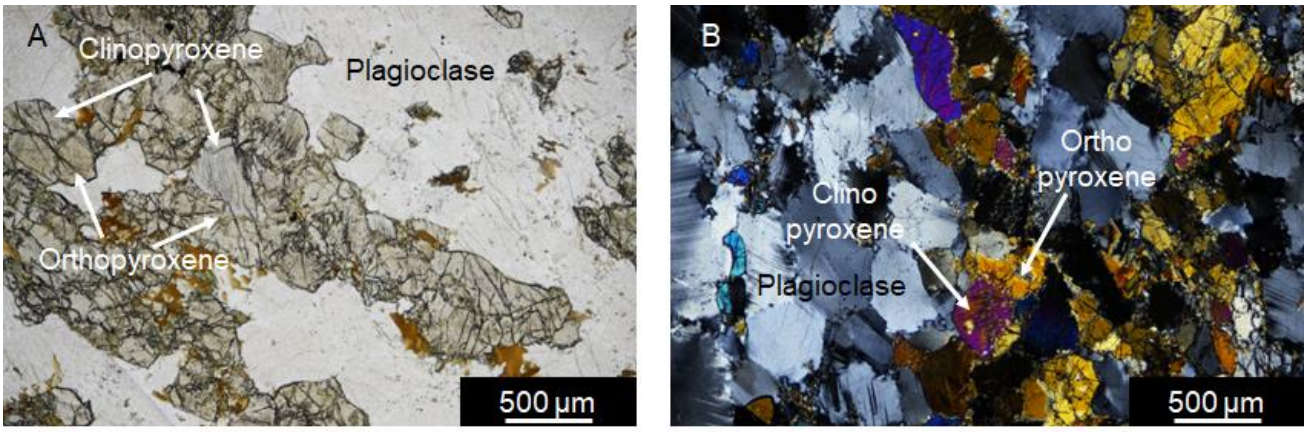

Fig. 14. Textural relationships of clinopyroxene from the Bégin-Lamarche deposit (under transmitted light). (A) Clinopyroxene crystals associated with orthopyroxene and plagioclase (sample LM18; plane-polarized light); (B) Clinopyroxene crystals associated with orthopyroxene and plagioclase (sample LM18; cross-polarized light).

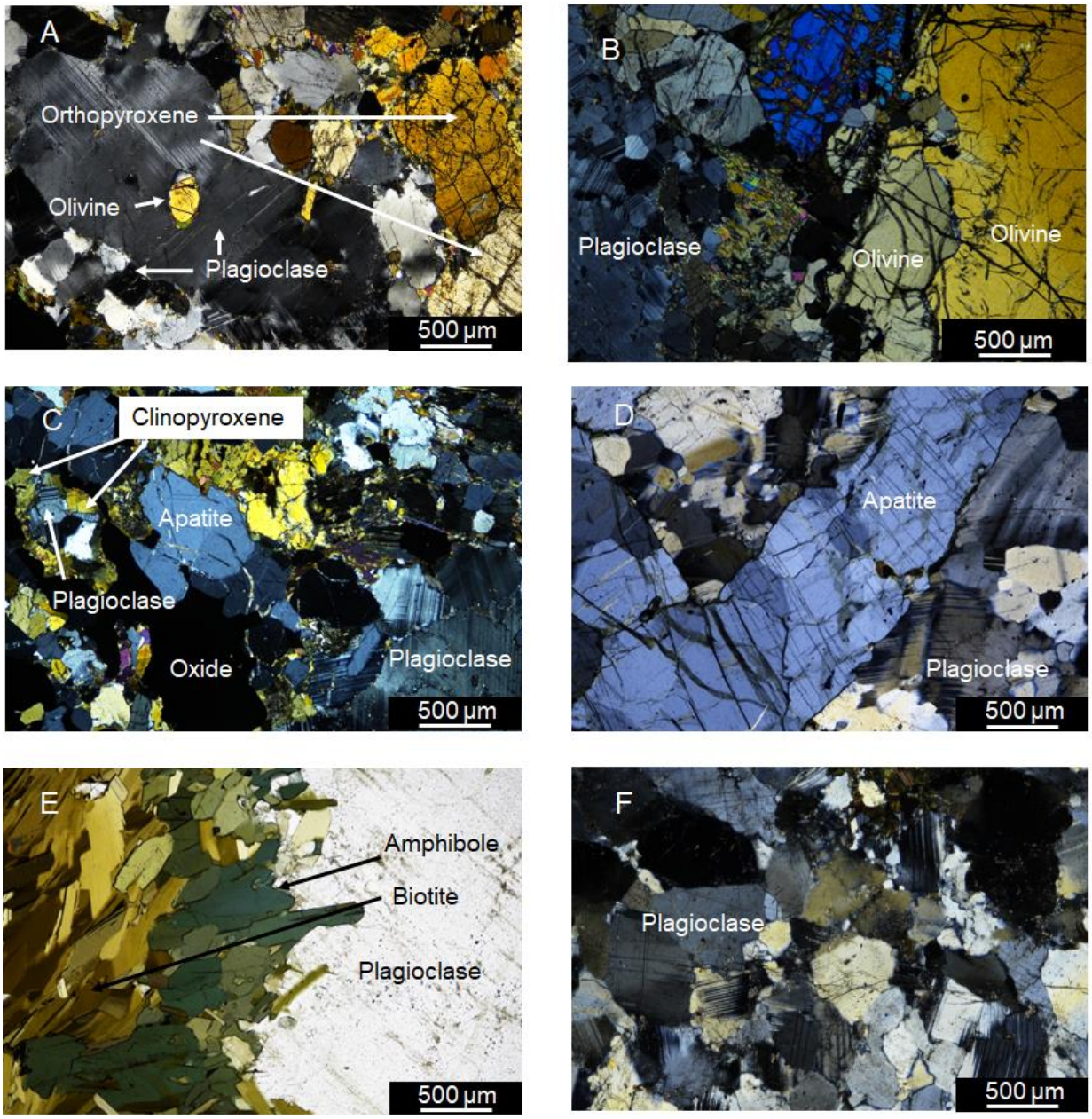

Fig. 15. Textural relationships of plagioclase from the Bégin-Lamarche deposit (under transmitted light). (A) Cumulate texture of orthopyroxene and plagioclase; olivine is also present as inclusion within a plagioclase crystal (sample LM15; cross-polarized light); (B) Plagioclase crystals associated with olivine crystals (sample LM7; cross-polarized light) c); (C) Different sizes of plagioclase crystals associated with clinopyroxene, apatite, and oxide minerals (sample LM21; cross-polarized light); (D) Plagioclase crystals associated with apatite crystals (sample LM48; cross-polarized light); (E) Plagioclase crystals associated with amphibole and biotite crystals (sample LM16; plane-polarized light); (F) Granoblastic texture of plagioclase crystals with serrated crystal boundaries in anorthosite (sample LM33; cross-polarized light).

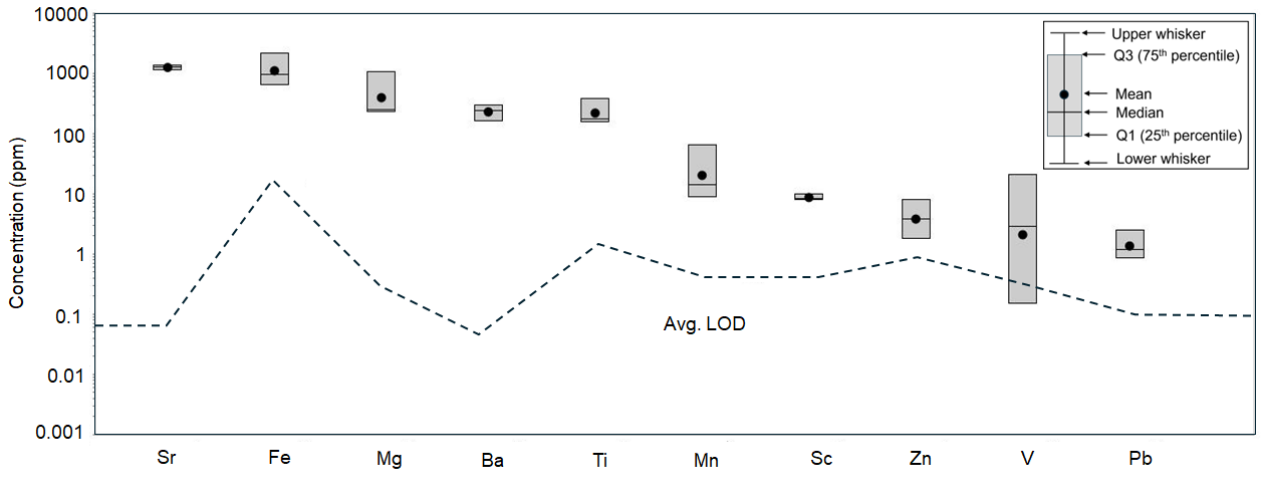

Fig. 16. Concentrations of selected trace (and minor) elements in plagioclase (n=3 samples) of the Bégin-Lamarche deposit (North and South Zone). The less than LOD values (<LOD) are replaced by LOD/2. The elements are arranged by their decreasing concentrations.

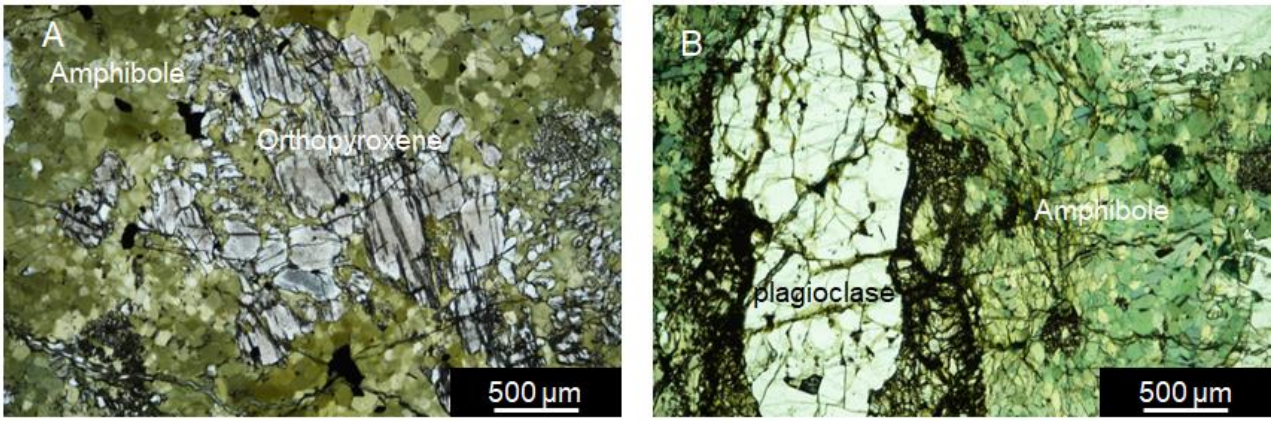

Fig. 17. Textural relationships of amphibole from the Bégin-Lamarche deposit (under transmitted plane-polarized light). (A) Amphibole crystals surrounding orthopyroxene crystal; note the conversion of orthopyroxene to amphibole (sample LM5); (B) Amphibole crystals associated with plagioclase crystals (sample LM40).

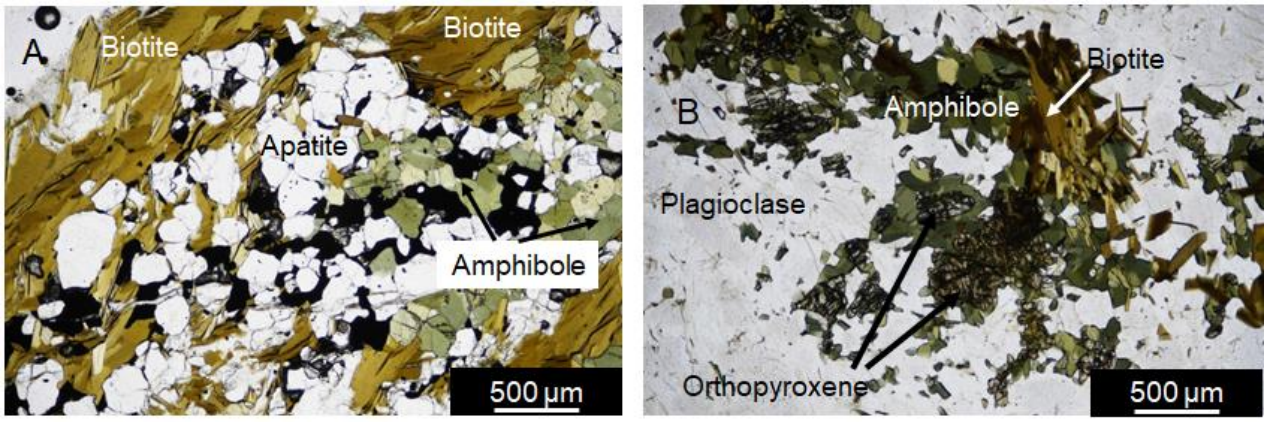

Fig. 18. Textural relationships of biotite from the Bégin-Lamarche deposit (under transmitted plane-polarized light). (A) Biotite crystals associated with apatite and amphibole crystals (sample LM16); (B) Biotite crystals associated with amphibole and plagioclase crystals (sample LM2); Note the orthopyroxene surrounded by amphibole.

Amphibole [$(Ca,Na)_2(Mg,Fe,Al)_5(Al,Si)_8O_{22}(OH)_2$]: Most of the samples contain < 10 % of amphibole. However, four samples (LM05, LM16, LM20, and LM21; Table 2) contain high amounts of amphibole (11-68 %; Fig. 8C). Amphibole crystals are subhedral to anhedral and associated with orthopyroxene (Fig. 17A), plagioclase (Fig. 17B), and biotite (Fig. 17E). Conversion of orthopyroxene to amphibole was also observed (Fig. 17A) in a few samples.

The Mg# of amphibole exhibits a wide variation (42.6-75.6; Table 3). The Al_2O_3 (7.4-15.6 wt.%), TiO_2 (0.4-1.5 wt.%), and Na_2O (0.7-3.3 wt.%) contents of amphibole are higher than those of orthopyroxene and clinopyroxene. The MnO contents of amphibole (0.02-0.2 wt.%) are, however, lower than those of the orthopyroxene (0.4-0.9 wt.%; Table 3). Trace elements were not analyzed for amphibole.

Biotite ($K(Mg,Fe)_3AlSi_3O_{10}(F,OH)_2$): Most of the samples contain < 10 % of biotite. However, two samples (LM16 and LM20) contain high amounts of biotite (16-36 %). Biotite crystals are tabular in shape. They are mostly associated with amphibole and plagioclase (Fig. 18A and B). In a few cases, they are also associated with apatite (Fig. 18A).

Biotite has a widely variable Mg# (46.1-86.3). The Al_2O_3 (14.6-17.2 wt.%), TiO_2 (0.4-4.3 wt.%), Na_2O (0.04-0.3.1 wt.%), and MnO (0.02-0.06 wt.%) contents of biotite are comparable with those of amphibole (Table 3). Trace elements were not analyzed for biotite.

Chlorite [$(Mg,Fe)_3(Si,Al)_4O_{10}(OH)_2 \cdot (Mg,Fe)_3(OH)_6$]: Chlorite is identified during mineral liberation analysis (MLA) in SEM. Most of the samples contain < 10 % of chlorite. Only two samples (LM41 and LM45) contain high amounts of chlorite (15-16 %).

Apatite ($Ca_5(PO_4)_3F$): Apatite crystals are mostly present within melanocratic layers. The crystals are dominantly associated with oxide minerals, i.e., magnetite and ilmenite (Fig. 19A-C). Apatite crystals in association with olivine (Fig. 19D and E), and orthopyroxene (Fig. 19E) are also common. In a few cases, they are also associated with amphibole and biotite. The presence of apatite within the leucocratic layers (plagioclase-rich) is also observed, but their abundances were low (< 5%). Apatite crystals are subhedral to anhedral and range in size from ~0.1 to 1 mm. In some cases, apatite crystals are cross-cut by late-stage carbonate (Fig. 19B) and other types of (serpentine?) veins (Fig. 9E).

Apatite crystals have narrow ranges of CaO (54.8-55.7 wt.%) and P_2O_5 (41.4-41.8 wt.%) contents. The SiO_2 (≤0.2 wt.%) and MnO (0.4-0.9 wt.%) contents are low (Table 3). F (1.67-3.4 wt.%) concentrations are higher than Cl (0.04-0.5 wt.%) and H_2O (0.4-1.4 wt%; in the form of -OH; Table 3) concentrations. Comparison of *in-situ* Cl content analyses of apatite crystals both from the University of British Columbia and Queen's University showed similar results (Fig. 20, Table 5). Therefore, Cl content analysis by EPMA is highly reliable to trace Cl contents of apatite for exploration purposes. Mole fraction values of fluor-(FAp), chlor-(CAp), and hydroxylapatite (HAp) are calculated following the procedure described by Piccoli and Candela (2002). The ternary plot of FAp-CAp-HAp indicates that the apatite in **the Bégin-Lamarche deposit is predominantly fluorapatite** (Fig. 21). Apatite crystals also have a narrow range in their CaO/P_2O_5 ratios (1.32-1.34), but relatively higher variability in their F/Cl ratios (4.7-63.8, Fig. 22).

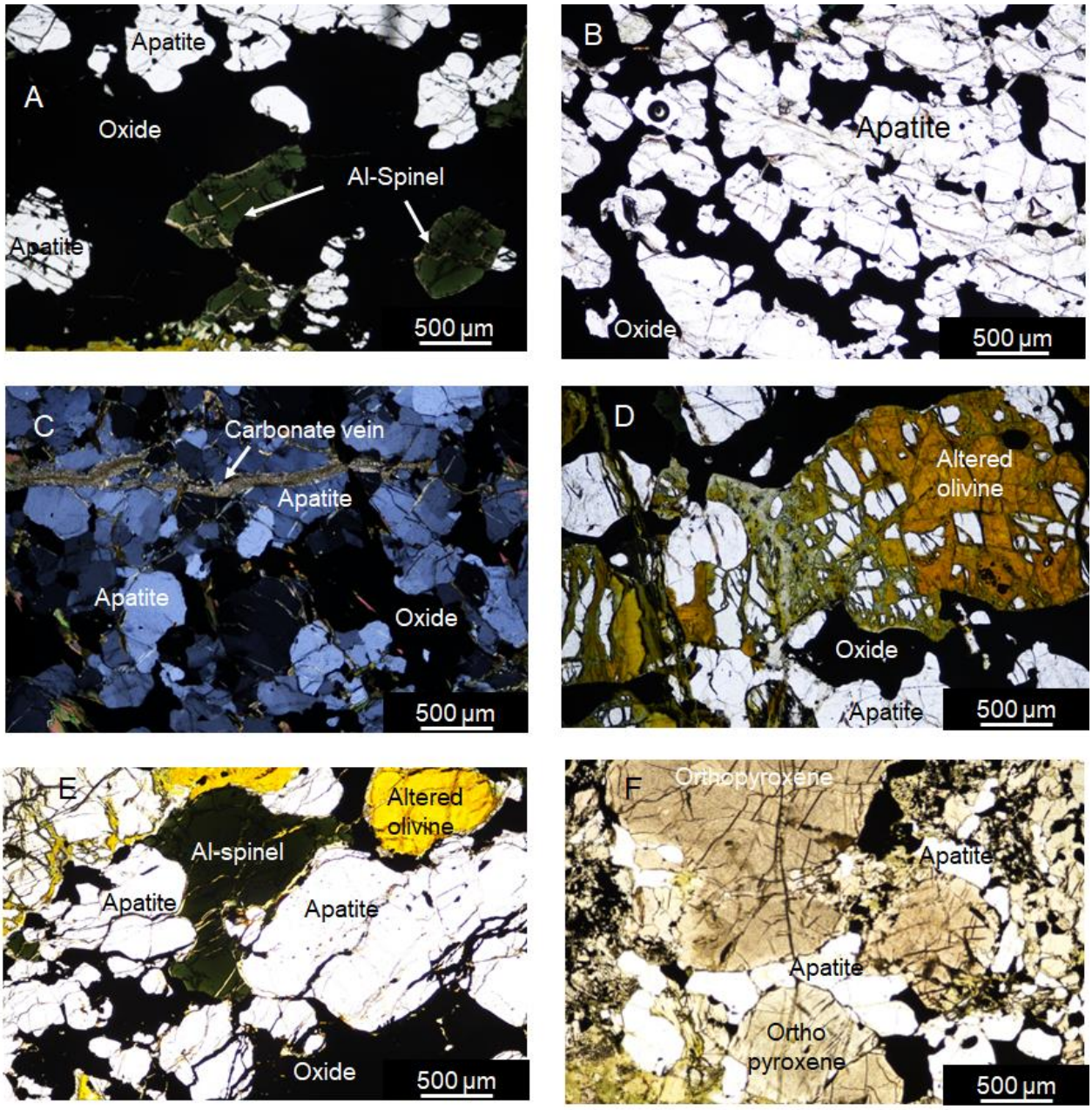

Fig. 19. Textural relationships of apatite from the Bégin-Lamarche deposit (under transmitted light). (A) Apatite crystals associated with oxide minerals and Al-spinel (sample LM4; plane-polarized light); (B) Apatite crystals with different sizes within oxide minerals-rich layer (sample LM49; plane-polarized light); (C) Apatite crystals associated with oxide minerals; a carbonate vein cross-cut apatite (sample LM44; cross-polarized light); (D) Apatite crystals associated with altered olivine (iddingsite) and oxide minerals (sample LM12; plane-polarized light); (E) Apatite crystals associated with altered olivine, Al-spinel, and oxide minerals (sample LM3; plane-polarized light); (F) Apatite crystals associated with orthopyroxene crystals (sample LM15; plane-polarized light).

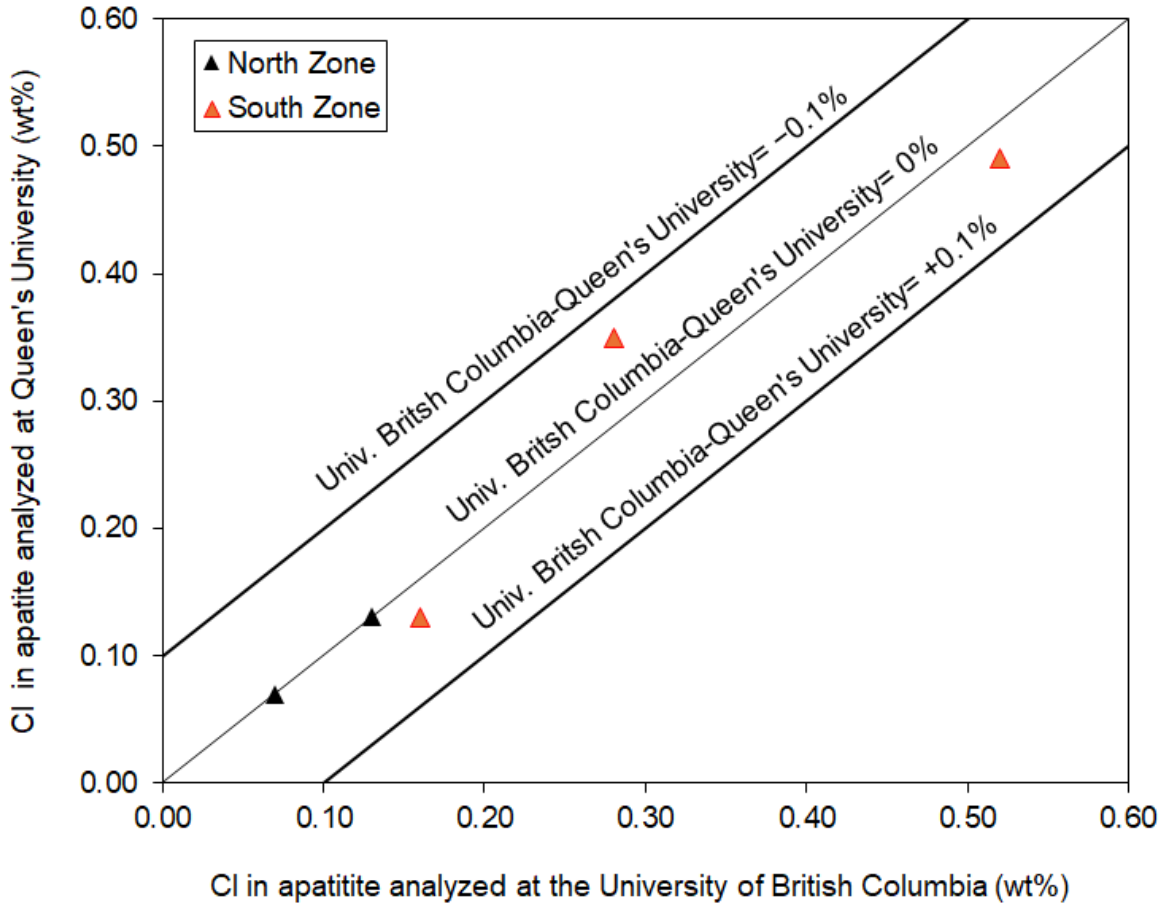

Fig. 20. Comparisons of *in situ* Cl contents of apatite crystals analyzed at the University of British Columbia and Queen's University.

Table 5. Comparisons of F and Cl contents (±1σ) of apatite crystals from the Bégin-Lamarche deposit (North and South Zone) analyzed by EPMA from the University of British Columbia and Queen's University. The average FAp, CAp, and HAp components of apatite crystals are also included.

		University of British Columbia							Queen's University				
Sample	spots	F	Cl	X (FAp)	X (CAp)	X (HAp)	Sample	spots	F	Cl	X (FAp)	X (CAp)	X (HAp)
		(wt%)	(wt%)	avg. molar fractions					(wt%)	(wt%)	avg. molar fractions		
North Zone													
LM01	n=11	2.88±0.25	0.13±0.02	0.76	0.02	0.22	LM1	n=9	3.05±0.14	0.13±0.01	0.81	0.02	0.17
LM02	n=03	1.67±0.11	0.20±0.06	0.44	0.03	0.53							
LM13	n=10	2.88±0.23	0.07±0.02	0.76	0.01	0.23	LM13	n=9	3.12±0.1	0.07±0.004	0.83	0.01	0.16
LM16							LM16	n=9	3.01±0.1	0.31±0.01	0.80	0.05	0.16
LM26	n=13	2.8±0.33	0.04±0.01	0.74	0.01	0.25							
LM32	n=11	3.41±0.32	0.09±0.02	0.91	0.01	0.08							
LM35	n=12	3.16±0.25	0.07±0.02	0.84	0.01	0.15							
South Zone													
LM38	n=13	3.21±0.21	0.08±0.01	0.85	0.01	0.14							
LM39	n=10	2.27±0.2	0.05±0.01	0.60	0.01	0.39							
LM41	n=10	2.52±0.13	0.28±0.09	0.67	0.04	0.29	LM41	n=9	2.67±0.17	0.35±0.02	0.71	0.05	0.24
LM45	n=11	2.43±0.15	0.52±0.03	0.65	0.08	0.28	LM45	n=9	2.46±0.13	0.49±0.02	0.65	0.07	0.27
LM50	n=11	2.79±0.09	0.16±0.04	0.74	0.02	0.24	LM50	n=9	2.81±0.1	0.13±0.01	0.75	0.02	0.24

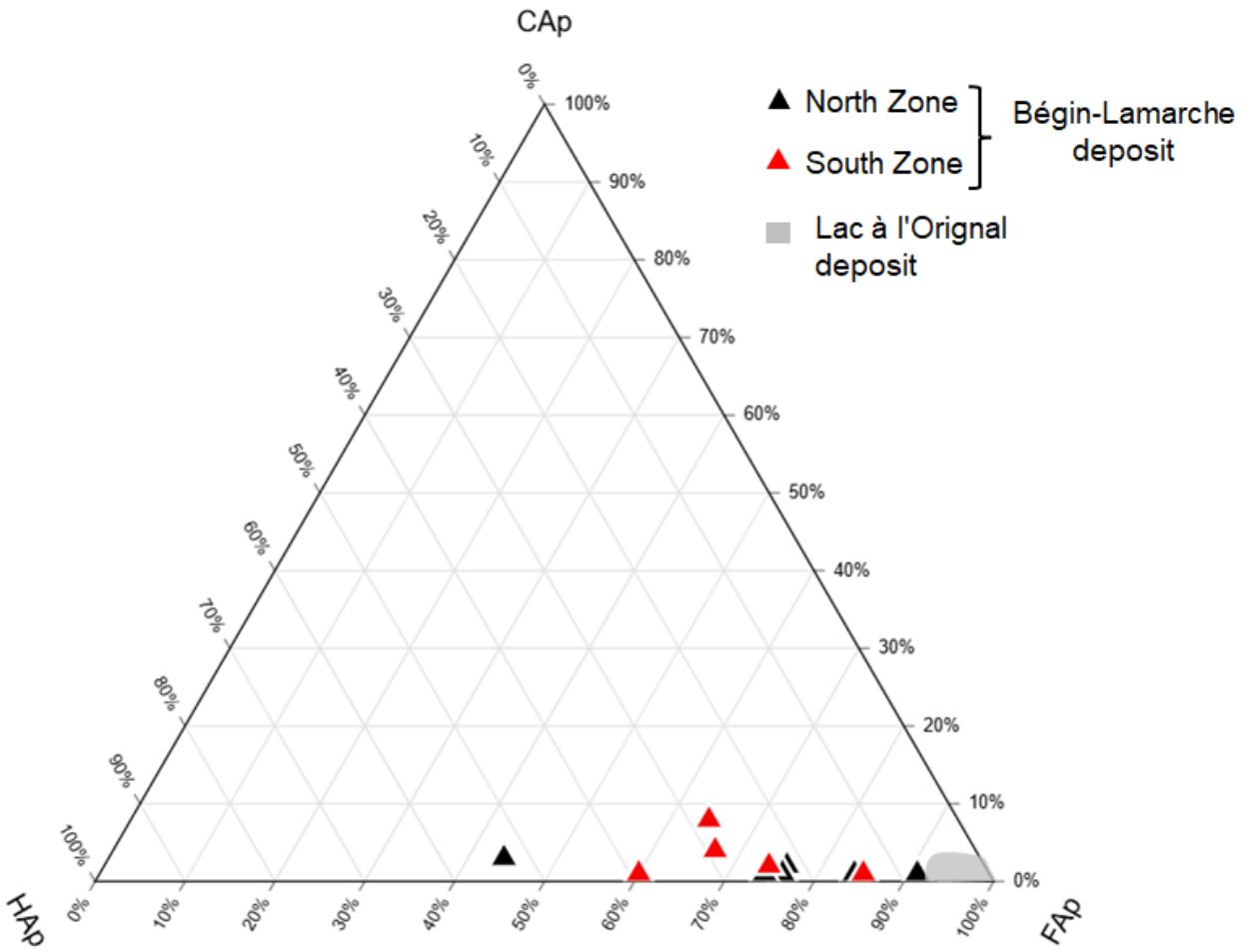

Fig. 21. Ternary plot of fluor- (FAp), chlor-(CAp), and hydroxyl-apatite (HAp) showing the variability of F-Cl-OH in the halogen-site of apatite from the Bégin-Lamarche deposit (North and South Zone). The variabilities of FAp, CAp, and HAp components of apatite crystals of the Lac à l'Orignal deposit are also shown.

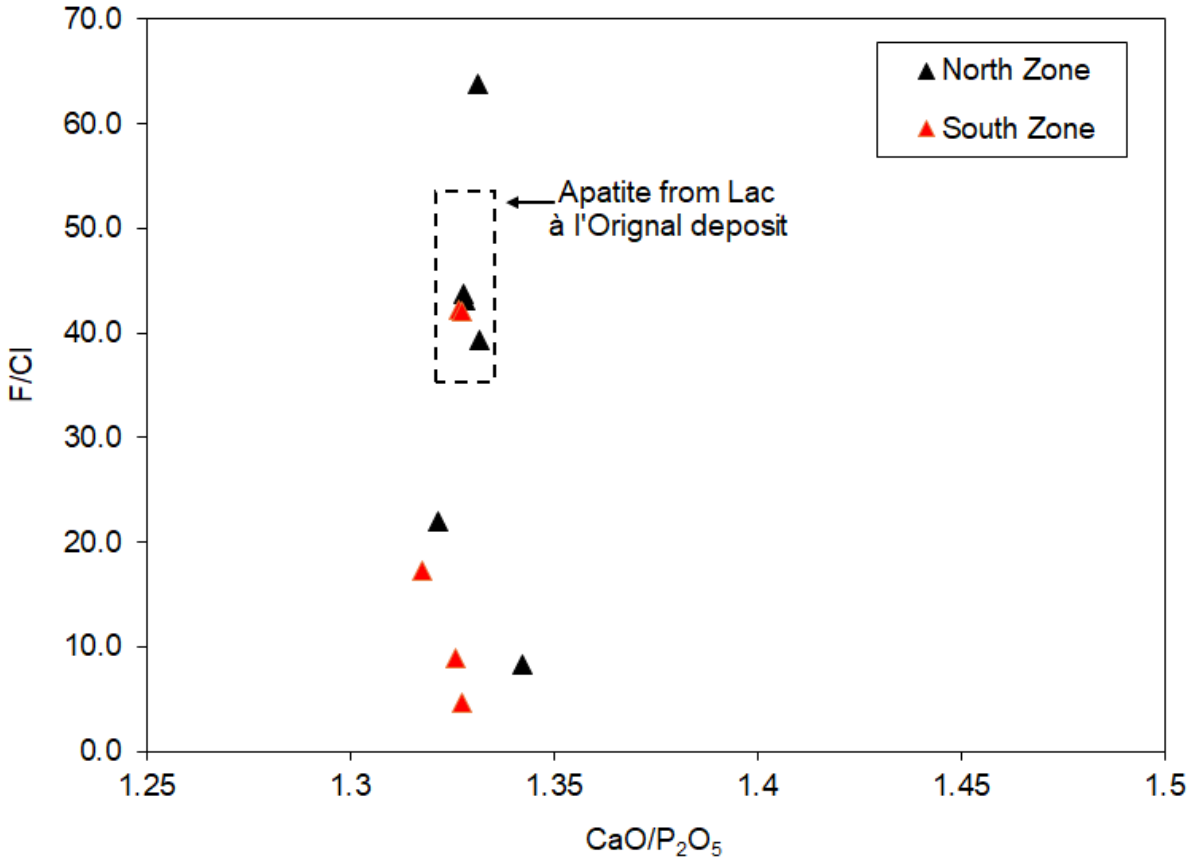

Fig. 22. Variations of F/Cl and CaO/P_2O_5 ratios (from EPMA analysis) of *in situ* apatite crystals from the Bégin-Lamarche deposit (North and South Zone). The variations of F/Cl and CaO/P_2O_5 ratios of apatite crystals of the Lac à l'Orignal deposit are also shown.

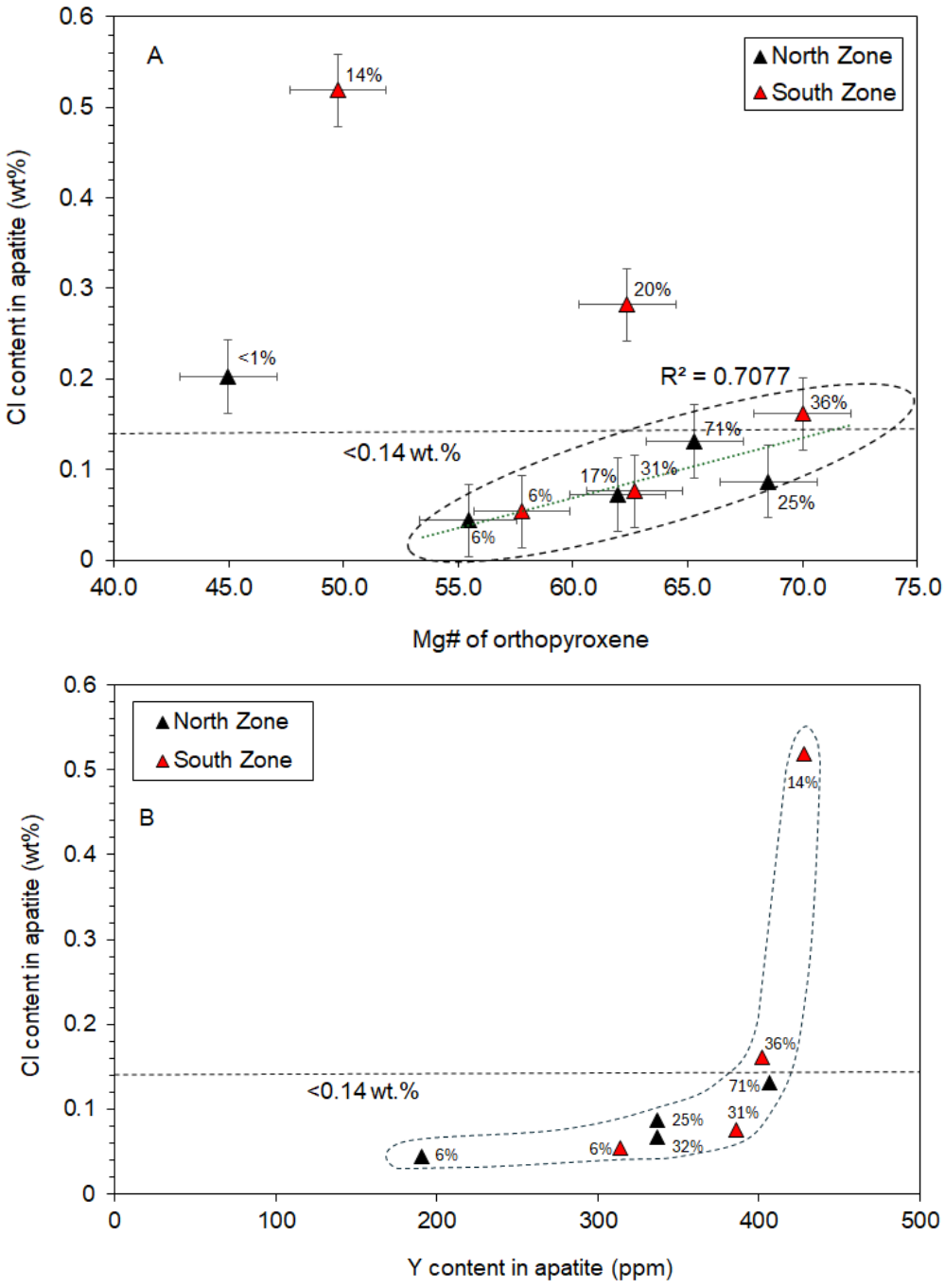

Fig. 23. (A) Relationships between Cl contents of apatite (fluorapatite) and Mg# of coexisting orthopyroxene from the rocks of the Bégin-Lamarche deposit (North and South Zone); (B) Relationships between Cl and Y contents in apatite from the rocks of the Bégin-Lamarche deposit. Apatite abundances (in % values) are shown in Figures. The upper limits of the Cl content of saleable phosphate ore (<0.14 wt.%) suggested by Yara International are also shown (Paiement et al., 2013). The average standard deviations of data (bar and whiskers) are also shown in Figure A, as calculated using avg. SD = $\sqrt{}$ ($S_1^2 + S_2^2 + \ldots. + S_k^2$)/k; where S_k = standard deviation for the 'k'th sample and k = total number of samples (Cohen, 1988).

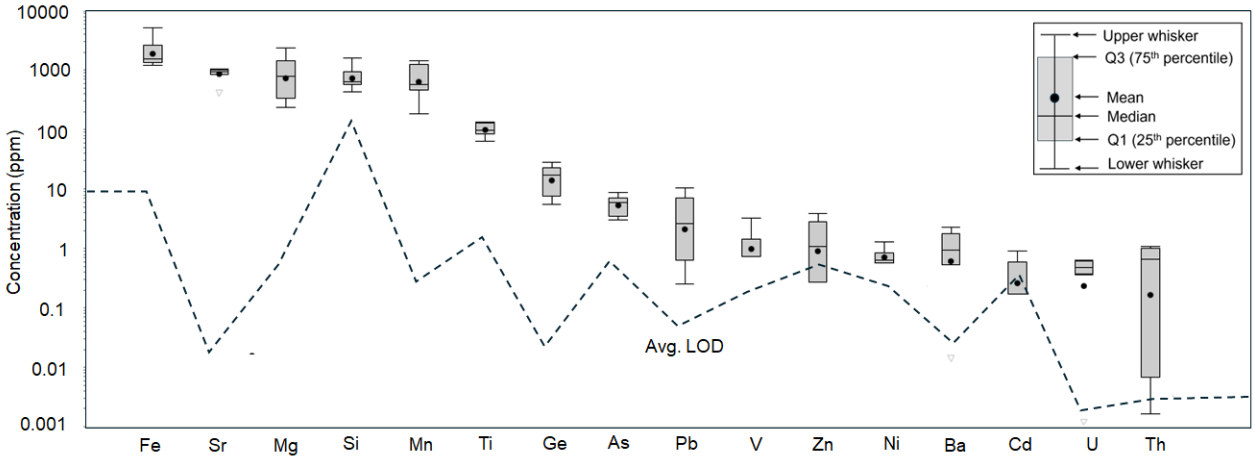

Fig. 24. Concentrations of selected trace (and minor) elements in apatite (n=8 samples) of the Bégin-Lamarche deposit (North and South Zone). The less than LOD values (<LOD) are replaced by LOD/2. The elements are arranged by their decreasing concentrations.

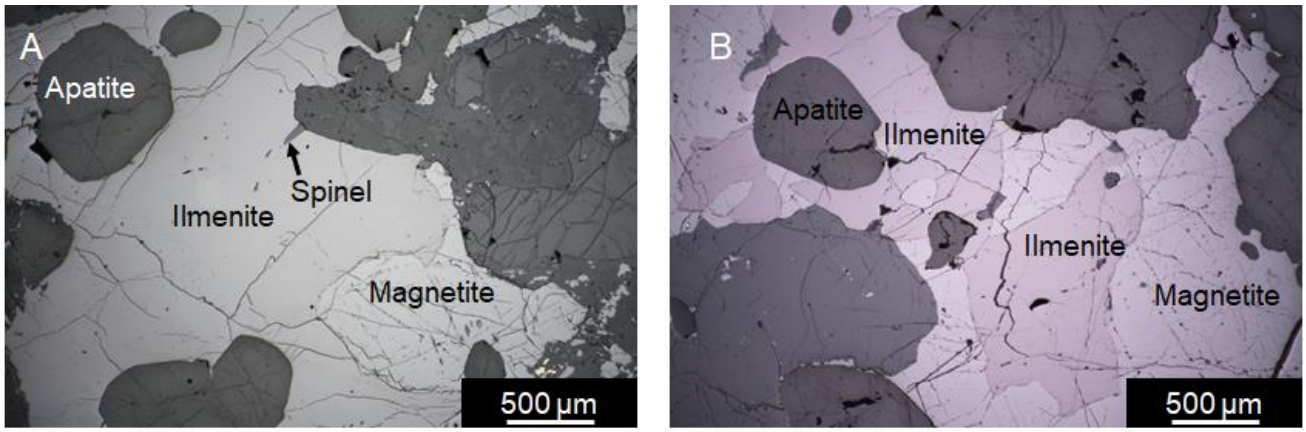

Fig. 25. Textural relationships of ilmenite from the Bégin-Lamarche deposit (under reflected light). A (sample LM 23) and B (sample LM28) showing ilmenite crystals associated with magnetite and apatite crystals.

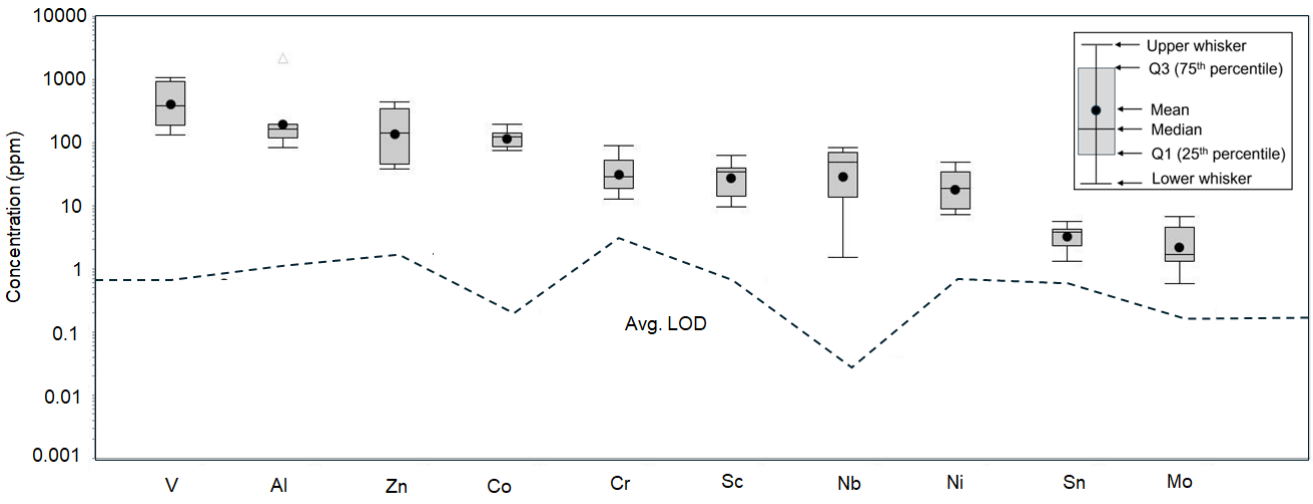

Fig. 26. Concentrations of selected trace elements in ilmenite (n=9 samples) of the Bégin-Lamarche deposit (North and South Zone). The less than LOD values (<LOD) are replaced by LOD/2. The elements are arranged by their decreasing concentrations.

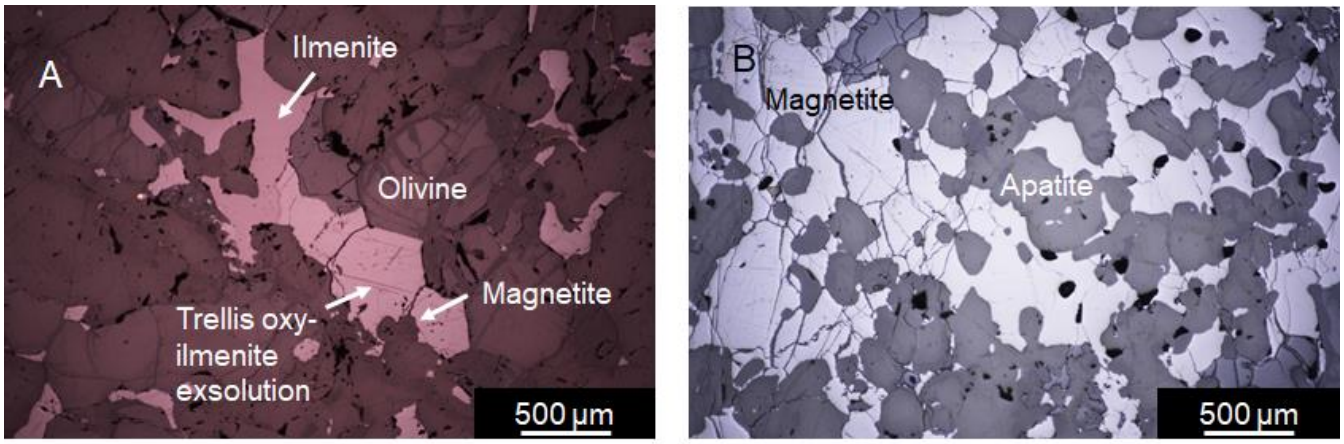

Fig. 27. Textural relationships of magnetite from the Bégin-Lamarche deposit (under reflected light). (A) Magnetite and ilmenite crystals associated with olivine crystals (sample LM8); note the presence of trellis oxy-ilmenite exsolutions in magnetite; (B) Magnetite crystals associated with apatite crystals (sample LM36).

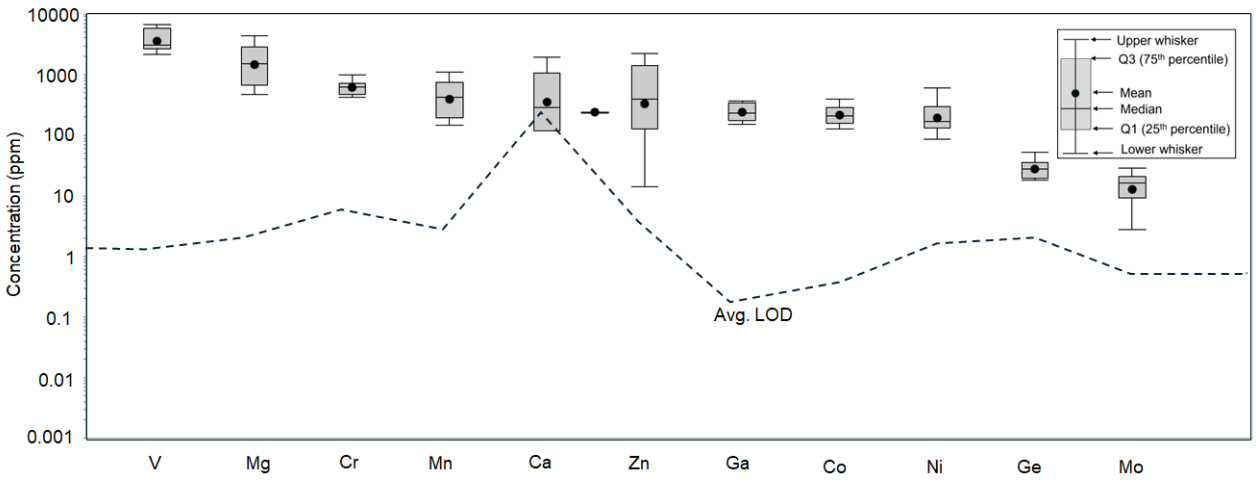

Fig. 28. Concentrations of selected trace (and minor) elements in magnetite (n=8 samples) of the Bégin-Lamarche deposit (North and South Zone). The less than LOD values (<LOD) are replaced by LOD/2. The elements are arranged by their decreasing concentrations.

The Cl content of (fluor)apatite and Mg# of the coexisting orthopyroxene suggests that the rocks from the Bégin-Lamarche deposit can be grouped into at least two groups (Fig. 22A). One group shows a good positive correlation between the Cl content of (fluor)apatite and Mg# of the coexisting orthopyroxene (i.e., Cl contents of apatite increase with increasing Mg# of coexisting orthopyroxene) and other group does not show such relationship. Furthermore, an overall positive correlation also exists between the Cl and Y contents of (fluor)apatite, both of which behave incompatibly during fractional crystallization (Fig. 23B).

Common trace elements in apatite include Sr (409-1053 ppm), Mg (235-2352 ppm), Mn (182-1473 ppm), Ti (64-133 ppm), Ge (11-45 ppm), As (3-9 ppm), and Pb (0.3-11 ppm; Fig. 24; Table 4). The REE concentrations of apatite are high (1565-2596 ppm in total; Table 4).

Ilmenite ($(Fe,Ti)_2O_3$): Ilmenite (0-24 %) is one of the two major oxide minerals forming the melanocratic oxide-rich lithologies (Fig. 25A and B). Ilmenite crystals are mostly subhedral. Hematite exsolution lamellae were not observed in ilmenite crystals in this study. Ilmenite crystals are predominantly associated with magnetite and apatite. The ilmenite/magnetite ratios vary between 0.4 and 8.1 (Table A2).

Ilmenite crystals possess a narrow range of TiO_2 (49.7-52.5 wt.%) and FeO (45.2-49.2 wt.%) contents. The MnO (0.4-0.9 wt.%), MgO (0.3-1.5 wt.%), and Cr_2O_3 ($\leq$ 0.02 wt.%) contents are low (Table 3). The low X_{hem} (mole fraction of hematite in ilmenite) of ilmenite (0.0-0.06; Table 3) also suggests the near absence of hematite in ilmenite crystal in this study.

Common trace elements include V (131-1073 ppm), Al (83-367 ppm), Zn (37-440 ppm), Co (73-195 ppm), Cr (13-87 ppm), Sc (10-62 ppm), Nb (2-82 ppm), Ni (7-49 ppm), Sn (1-6 ppm), and Mo (1-7 ppm; Fig. 26, Table 4). The REE concentrations of ilmenite are very low (< instrumental LOD).

Magnetite (Fe_3O_4): Magnetite (0-27 %) is the other major oxide phase forming melanocratic, oxide-rich lithologies (Fig. 27A and B). Abundances of total oxide minerals (magnetite + ilmenite) in the deposit are 0–49 % (Table A2). Magnetite crystals are mostly subhedral. Magnetite crystals are associated with ilmenite and apatite. Fine-scale trellis oxy-exsolutions of ilmenite (<10μm) are very common in magnetite (Fig. 27A). Magnetite crystals also exhibit a narrow range of FeO content (91.0-92.6 wt%). The TiO_2 (0.15-1.36 wt %), MgO (0.01-0.15 wt%), and MnO ($\leq$0.07 wt. %) contents of magnetite are low (Table 3).

Common trace elements include Cr (415-989 ppm), Mn (144-1097 ppm), Zn (14-2196 ppm), Ga (150-366 ppm), Co (128-389 ppm), Ni (87-600 ppm), Ge (18-53 ppm), and Mo (3-28 ppm; Fig. 28, Table 4). The LA-ICP-MS analysis of magnetite also contains ilmenite exsolution because of the large beam diameter (35 μm) used for the analysis.

Al-spinel ($MgAl_2O_4$-$FeAl_2O_4$): Al-spinel (0-5 %) mostly occurs as individual crystals associated with ilmenite and magnetite (Fig. 19A and E). The Al-spinel are of Fe-rich (FeO= 22.8-33.8 wt%). The MgO contents (3.3-9.4 wt.%) of the Al-spinel are lower than their FeO contents.

Sulfide minerals: Sulfide minerals occur as accessory minerals (< 1 %) in this deposit. The most common sulfide mineral is pyrrhotite ($Fe_{1-x}S$, X=0 to 0.17; Fig. 29A). Chalcopyrite ($CuFeS_2$) is also observed in a few cases (Fig. 29B). Sulfide minerals are predominantly associated with oxide minerals and in a few cases, they also occur as inclusions within olivine (Fig. 29B).

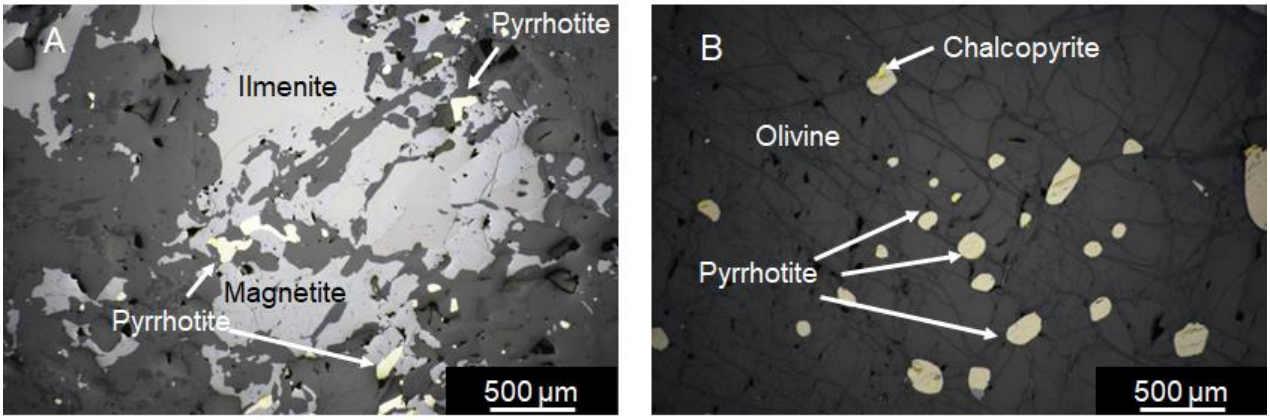

Fig. 29. Textural relationships of sulfide minerals from the Bégin-Lamarche deposit (under reflected light). (A) Pyrrhotite mineral associated with ilmenite and magnetite crystals (sample LM20); (B) Pyrrhotite crystals within olivine crystals (sample LM4).

8.2. Rare earth elements (REE) of apatite and silicate minerals

The REEs are trace elements with atomic numbers of 57-71 (La, Ce, Pr, Nd, Pm, Sm, Eu, Gd, Tb, Dy, Ho, Er, Tm, Yb, Lu). Y is also commonly included in this series. Total concentrations of REE in apatite crystals (REE=1565-2596 ppm, Y=191-429 ppm) are significantly higher than that of plagioclase (REE=8-14 ppm, Y=<LOD to 0.4 ppm), olivine, orthopyroxene, magnetite, and ilmenite (< instrumental LOD) because REE preferentially partition into the Ca site of apatite (Banerjee et al., 2024b; Prowatke and Klemme, 2006; Owens et al., 2019; Ayers and Watson, 1993).

Concentrations of REEs are conventionally represented as normalized (ratios) values with respect to chondrite, which is a type of meteorite (Fig. 30A and B; Pourmand et al., 2012). Chondrite-normalized REE patterns of plagioclase (Fig. 30A), and apatite (Fig. 30B) reveal:

a) plagioclase shows a prominent positive Eu anomaly and apatite shows a slight negative Eu anomaly. Positive and negative Eu anomalies are defined by chondrite-normalized Eu concentrations that are higher and lower than those of its neighboring Sm and Gd concentrations, respectively (Rollinson, 2014).

b) Apatite has higher concentrations of light rare earth elements (LREE include La, Ce, Pr, Nd, Sm, Eu, Gd) than heavy rare earth elements (HREE include Tb, Dy, Ho, Er, Tm, Yb, Lu), typical of apatite from mafic intrusions (Banerjee et al., 2024b; Kieffer et al. 2023; Miloski et al. 2024).

8.3. Chemistry of the Bégin-Lamarche (North and South Zone) apatite concentrate

Apatite concentrate was prepared from a part of the Bégin-Lamarche deposit. The apatite concentrate was prepared and analyzed by SGS Canada. Beneficiation produces an apatite concentrate that has similar CaO (53.8 wt.%) and P_2O_5 (40.9 wt.%) contents to those analysed *in situ* by EPMA (CaO= 55.3 ±0.3 wt.%, P_2O_5= 41.7±0.13 wt.%; Table 6). The CaO/P_2O_5 (1.32) ratios of the concentrate and in situ crystals (1.33±0.1) are also similar (Table 6 and Fig. 22). The minor element ratio [MER= (Fe_2O_3+Al_2O_3+MgO)/P_2O_5] of the apatite concentrate is low (0.04, Table 6). Finally, Na_2O, K_2O, TiO_2, MnO, Cr_2O_3, and V_2O_5 contents of the apatite concentrate are also low (≤0.12 wt%; Table 6).

The F and Cl contents of the apatite concentrate were not analyzed. The *in-situ* analysis of apatite crystals by EPMA indicates that the average F content of apatite crystals is 2.73±0.5 wt% (n=11 samples) and the average Cl content is 1540±1410 ppm (n=11 samples from this study; Table 7).

The threshold concentrations of major oxide and selected elements in an ideal phosphate concentrate for producing phosphoric acid (provided by Prayon, 2022) are provided in Table 7. Those concentration data are compared with those of the apatite from the Bégin-Lamarche deposit. P_2O_5, CaO, Si, Fe, Al, Mg, Ti, and Na concentration data of apatite are from apatite concentrate that were prepared and analyzed by SGS Canada. The elemental concentration data (Si, Fe, Al, Mg, Ti, and Na) of apatite concentrate are calculated from their oxide data provided in Table 6. F, Cl, As, Cd, Th, and U concentrations of apatite are from *in situ* analysis of apatite crystals by EPMA and LA-ICP-MS methods.

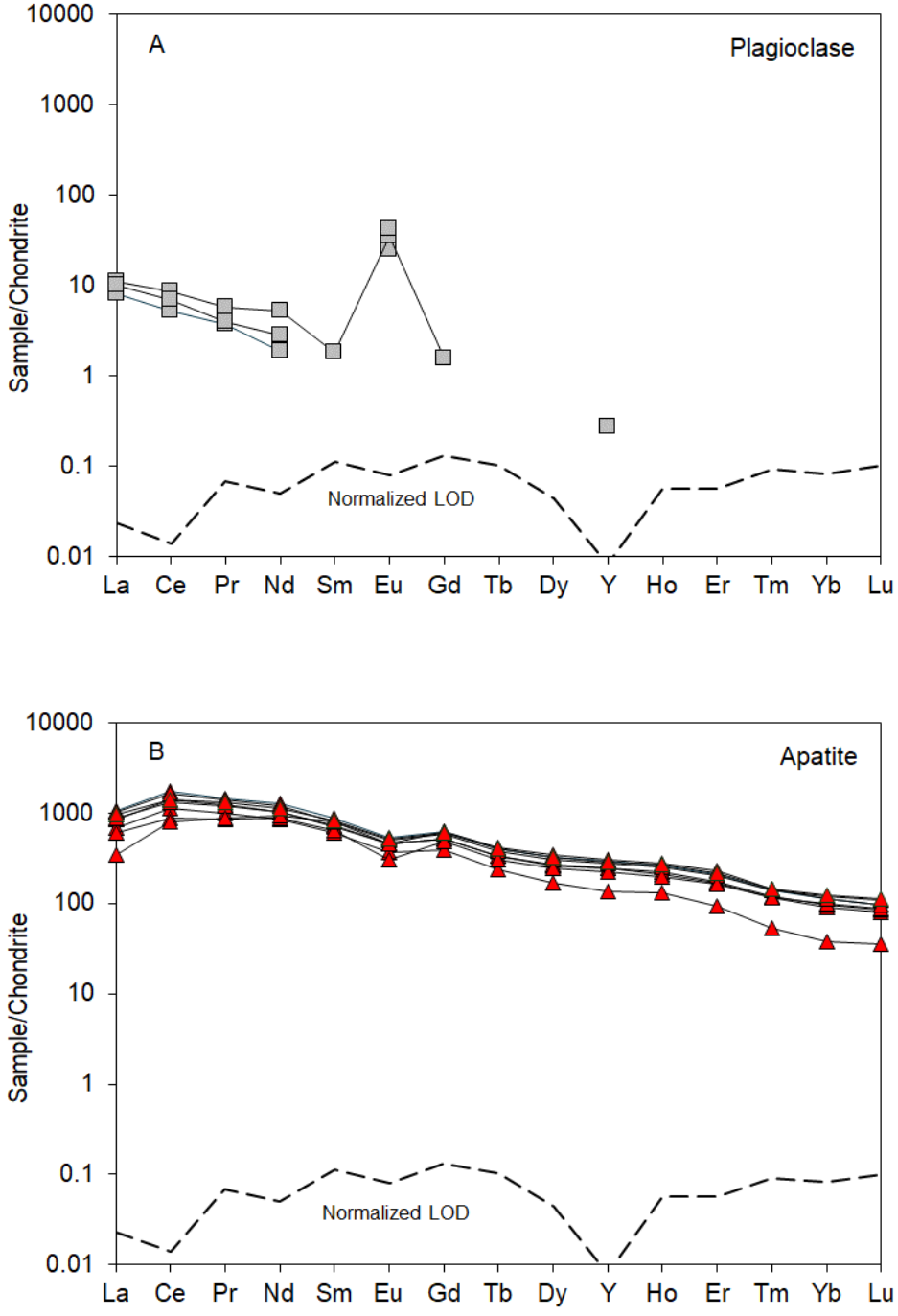

Fig. 30. Chondrite-normalized REE patterns of (A) plagioclase and (B) apatite crystals from the Bégin-Lamarche deposit (North and South Zone).

Table 6. Chemical compositions of apatite concentrate separated and analyzed by SGS Canada. *In situ* analyses of apatite crystals from the University of British Columbia are also included for comparison.

	SGS	University of British Columbia
	(apatite concentrate)	(*in-situ* anlysis of apatite; n=115 spots)
	(wt%)	(wt%)
SiO_2	0.79	0.06±0.05
Al_2O_3	0.34	
Fe_2O_3	0.81	
MgO	0.4	0.07±0.05
CaO	53.8	55.3±0.3
Na_2O	0.09	0.06±0.02
K_2O	0.02	
TiO_2	0.12	
P_2O_5	40.9	41.7±0.13
MnO	0.08	0.07±0.05
Cr_2O_3	0.01	
V_2O_5	<0.01	
CaO/P_2O_5	1.32	1.33±0.01
MER	0.04	
MER= $(Fe_2O_3+Al_2O_3+MgO)/P_2O_5$		

Table 7. Comparison between threshold concentrations of selected elements (and oxides) in an ideal phosphate concentrate for producing phosphoric acid (provided by Prayon, 2022) and elemental (and oxide) concentrations of apatite from the Bégin-Lamarche deposit (North and South Zone).

	Threshold concentrations in an ideal phosphate concentrate	Apatite from the Bégin-Lamarche deposit
P_2O_5	36-39 wt%	40.9 wt%
CaO	48-52 wt%	53.8 wt%
CaO/P_2O_5	<1.5	1.32
F	<3.5 wt%	2.73±0.5 wt%* (n=115)
Cl	<600 ppm	1540±1410 ppm* (n=115)
MER	<4.5	0.04
Si	2.33 wt%	0.4 wt%
Fe	<0.49 wt%	0.57 wt %
Al	<0.37 wt%	0.18 wt%
Mg	<0.12 wt%	0.24 wt%
Ti	<2600 ppm	720 ppm
Na	<0.56 wt%	0.07 wt%
As	<5 ppm	5.6±2 ppm* (n=48)
Cd	<3 ppm	<0.1 ppm* (n=48)
Th	<22 ppm	<1.0 ppm* (n=48)
U	<7 ppm	<1.0 ppm* (n=48)

* Concentration data of these elements are from *in situ* apatite analysis (F and Cl analyses by EPMA; As, Cd, Th, and U analyses by LA-ICP-MS).

Concentration data of other elements or oxides are from apatite concentrate (prepared and analyzed by SGS Canada).

9. Discussion

9.1. Apatite of the Bégin-Lamarche (North and South Zone) as an ESG-compliant source of phosphate

The apatite or its concentrate must meet certain chemical assay criteria for producing phosphoric acid (Table 7). In the Bégin-Lamarche deposit, P_2O_5 (41.7±0.13 wt.%) and CaO (55.3±0.3wt.%) contents of *in situ* apatite crystals and the apatite concentrate (CaO= 53.8wt.%, P_2O_5 = 40.9 wt.%; Table 6 and 7) are better than required. The CaO/P_2O_5 ratios of both *in situ* apatite crystals (1.33±0.01) and the apatite concentrate (1.32) are also lower than (<1.5; Table 7) that of the ideal phosphate concentrate for producing phosphoric acid.

The F concentrations of *in situ* apatite crystals (2.73±0.5 wt%; Table 7) are lower than required (<3.5 wt%; Table 7). The Cl concentrations of *in situ* apatite crystals are variable (400-5000 ppm; Table 3) with an average value of 1540±1410 ppm (Table 7; Fig. 23), which is indeed higher than the required Cl content for ideal phosphate concentrate for producing phosphoric acid (Table 7); Yara International specified that the Cl content of apatite concentrate should be <0.14 wt% (or 1400 ppm) in order to be saleable (Paiement et al., 2013). Therefore, the average Cl contents of *in situ* apatite crystals from a minimal number of samples (n=11 in this study) are slightly higher than the Cl content value specified by Yara International. Here, it is important to note that the average value of Cl of *in situ* apatite crystals is not a weighted average.

The MER value of the apatite concentrate prepared and analyzed by SGS Canada (0.04) is significantly lower than the required value (<4.5) proposed by Prayon (Table 7). Furthermore, Si, Al, Ti, Na, Cd, Th, and U concentrations of apatite are lower than their required values proposed by Prayon (Table 7; Fig. 31). The Fe (0.57 wt%) and Mg (0.24 wt.%) contents of the apatite concentrate are slightly higher than their required values for ideal phosphate concentrate (Fe=<0.49 wt%, Mg= <0.12 wt%; Table 7). However, Fe (1230-5247 ppm or 0.12-0.52 ppm) and Mg (1924-12361 ppm or 0.2-1.2 wt%; Table 4) contents of *in situ* apatite crystals show significant variations.

In addition, the apatite from the Bégin-Lamarche contains a very low amount of radioactive elements, such as Pb (< 11 ppm; Table 4), U, and Th (<1 ppm; Table 7). The apatite concentrate with such low amounts of radioactive elements will produce phosphogypsum with very low amounts of radioactive elements during phosphoric acid production. As the phosphogypsum can potentially be recycled into plaster and wallboard, the high-quality and environment-friendly phosphogypsum could be an attractive saleable product. Finally, the low abundances of sulfide gangue minerals (<1%) suggest that the environmental impacts of acid mine drainage from tailings would be minimal. Thus, the high-quality apatite of the North and South Zone of the Bégin-Lamarche deposit with low contents of toxic trace elements, and low abundances of sulfide minerals make the deposit an attractive ESG-compliant source of North American P for the LFP battery industry.

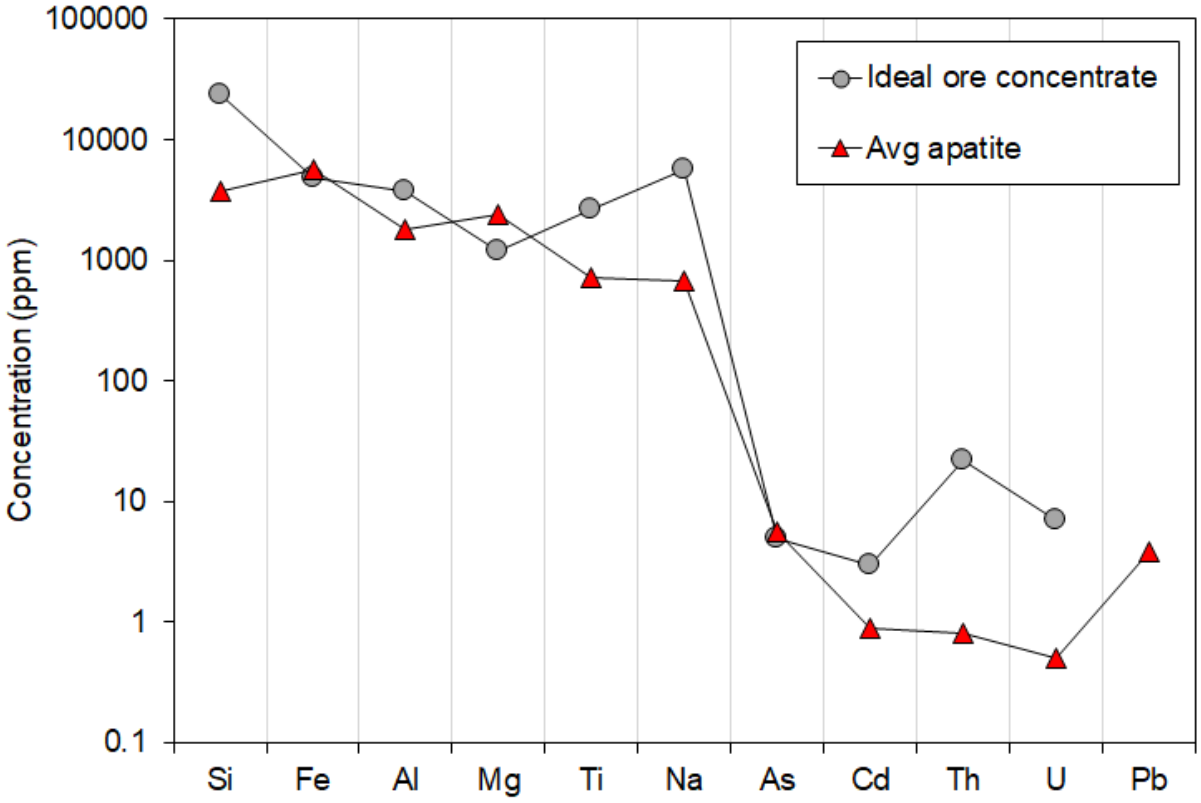

Fig. 31. Comparisons of selected elemental concentrations of ideal phosphate ore concentrate for phosphoric acid production (provided by Prayon), and average apatite crystals of the Bégin-Lamarche deposit (North and South Zone). Si, Fe, Al, Mg, Ti, and Na data of average apatite (Avg apatite) are from apatite concentrate (prepared and analyzed by SGS Canada), and As, Cd, Th, U, and Pb data of average apatite are from *in-situ* analysis of apatite crystals (analyzed in this study).

9.2. Cl content of (fluor)apatite of the Bégin-Lamarche (North and South Zone)

In general, (fluor)apatite can contain a low amount of Cl (<1000 ppm; Andersson et al., 2019). The Cl is corrosive to equipment for the production of phosphoric acid from apatite concentrate (Chandra et al., 2017; Schorr and Valdez, 2017). As Cl cannot be extracted before the production of phosphoric acid (Salas et al., 2017), phosphate ores with low Cl contents are preferred for producing phosphoric acid. **The "low Cl contents" of ideal phosphate ore could be variable**. For example, Prayon suggested that Cl contents should be < 600 ppm for producing phosphoric acid (Table 7) and Yara International suggested that Cl contents should be <1400 ppm for saleable phosphate ore (Paiement et al., 2013). Therefore, understanding the Cl distributions of apatite ore of a deposit is critical.

This study indicates that the Cl content of (fluor)apatite of the Bégin-Lamarche deposit is variable (400-5000 ppm; Table 3). In this study, only a very limited number of samples (n=11) were analyzed for Cl contents of apatite from a large area of the deposit. Furthermore, the deposit contains a wide variation of rock types (Table 2), and a statistically significant number of analyses from each rock type was not done in this study. Previously, a preliminary study from the North and South Zone of the Bégin-Lamarche deposit showed that Cl contents of apatite from the deposit vary between 623 and 863 ppm (n=8; Banerjee, 2023b) with an average value of 694±73 ppm. If all analyses are considered, the Cl contents of apatite in 74% of the samples (14 of the 19 samples) are below 1000 ppm, and 26% of the samples show high Cl contents (>1000 ppm; Fig. 32). **Therefore, it can be inferred that patchy (or local) distributions of apatite with high Cl content exist in the deposit.** Mixing of ore with high and low Cl contents can be considered an option to produce a mixed ore below the Cl concentration threshold required to minimize corrosion of equipment. Advanced methods for the reduction of Cl should also be explored.

9.3. Geological processes controlling the Cl content of (fluor)apatite of the Bégin-Lamarche (North and South Zone)

This study indicates that F/Cl contents of apatite of the Bégin-Lamarche vary significantly (4.7-63.8) and the variations are higher than that of the Lac à l'Orignal deposit (Fig. 22). The positive correlation between the Cl content of apatite and the Mg# of coexisting orthopyroxene for one group of apatite of the Bégin-Lamarche deposit (Fig 23A) suggests that the Cl content of the apatite progressively decreased with differentiation (i.e., with progressive crystallization). The high versus low Mg# for orthopyroxene is indicative of early versus late stage of crystallization, respectively. The Cl content of apatite and the Mg# of coexisting orthopyroxene for the Lac à l'Orignal deposit, however, showed a negative correlation, which suggests that the Cl content of apatite increases with differentiation (i.e., with progressive crystallization; Banerjee et al., 2024b). The negative correlation is expected because Cl behaved incompatibly during its crystallization (Banerjee et al., 2024b), and therefore, the Cl content of the magma increased progressively with magmatic differentiation.

In the case of the Bégin-Lamarche deposit, Cl content of the melt progressively decreased during the crystallization. The major reason for the progressive decrease of the Cl content of the melt is the progressive evolution of Cl-rich (exsolved) fluid during the crystallization of the magma (e.g., Webster et al. 2020). The alteration of olivine crystals to iddingsite (Fig. 9E and 19E), presence of corona structure (Fig. 11F), and alteration of orthopyroxene to amphibole (Fig. 17A) suggest an involvement of fluid during the end stages of crystallization of the magma. Furthermore, the previous study indicates that the Cl content of altered olivine and late-stage veinlets cross-cutting apatite have higher Cl content than that of the apatite (Banerjee, 2023b). Furthermore, the relationships between Al_2O_3 and Mg# of orthopyroxene suggest that the magma of the Bégin-Lamarche deposit was emplaced at shallower levels than that of the Lac à l'Orignal deposit (~0.2 to 1.7 kbar; Table A13, Fig. 12), which possibly facilitated exsolution of fluid (brines) from the magma of the Bégin-Lamarche deposit. Therefore, this study infers that the fluids evolved during the crystallization of the magma of the Bégin-Lamarche deposit and that fluid was responsible for the alteration of the deposit.

Apatite crystals from two samples from the South zone have > 0.25 wt% (or > 2500 ppm) of Cl contents. Both samples contain relatively high proportion of chlorite-type minerals (~ 15-16 %; Table 2). Therefore, other processes (such as alterations and recrystallization) could be responsible for such high Cl contents of the apatite crystals. Furthermore, it is possible that the area experienced multi-stages of magma injections and the high Cl contents of the apatite could be related to a different magmatic event. Apatite from one sample from the North zone also has a high Cl content (2025 ppm; Fig. 23A). However, apatite is present as an accessory phase (<1 %) in that anorthosite sample (LM02), and the Mg# of the orthopyroxene of that sample is the lowest (45). This relation suggests that the apatite crystallized during late stages and the apatite is not from ore-grade rock. In general, intercumulus apatite (i.e., crystallized from the interstitial liquid surrounding initially crystallized cumulus apatite) has higher Cl contents than that of cumulus apatite (Kieffer et al., 2023).

The Cl content of apatite overall increases with increasing Y content of apatite (Fig. 23B). It is important to note that instead of ∑REE contents, only Y contents of apatite are plotted against Cl contents of apatite because different REEs have different accuracies of measurements as inferred from the REE data of the Durango apatite (Appendix Table A9). The REE as well as Y (Y behaves similarly as REE) preferentially partitions into apatite (i.e., REE and Y are compatible in apatite; Fig. 30B and Table 4). Therefore, apatite with both low Y and Cl contents suggests its crystallization during the late stages of magmatic differentiation (or magmatic crystallization). Apatite with significantly high Y and Cl content (and relatively low Mg# of coexisting orthopyroxene, Fig 23A and B) from the South zone (Fig. 23B) can not be well understood due to the limited data set.

9.4. Mineral paragenesis, the timing of apatite crystallization, and fluid evolution

Mineral paragenesis describes the sequence or timing of mineral formation in any rock. Understanding mineral paragenesis is critical for properly characterizing ore bodies and waste rocks, which helps to determine exploration and exploitation strategies. As the rocks of the Bégin-Lamarche deposit are cumulate rocks, mineral paragenesis should be established most effectively

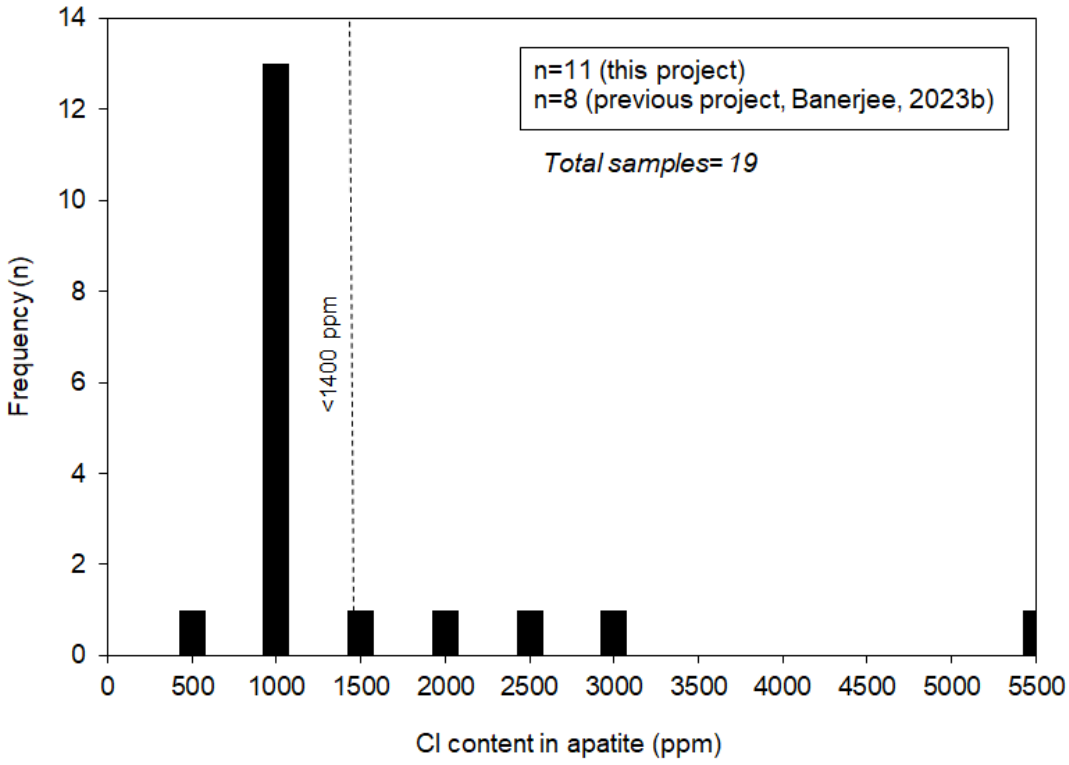

Fig. 32. Frequency distributions of Cl contents from *in situ* apatite crystals from the Bégin-Lamarche deposit (North and South Zone) analyzed in this study and a previous study (Banerjee, 2023b). The upper limit of the Cl content of saleable phosphate ore (< 1400 ppm) suggested by Yara International is also shown (Paiement et al., 2013).

through high-frequency sampling of a drill hole (e.g., Charlier et al., 2008; Namur et al., 2010). A petrographic study from high-frequency samples from a drill hole would help understand the appearance, disappearance, and reappearance of minerals in different layers of the deposit. This study, however, tried to solve the mineral paragenesis puzzle from isolated pieces of information based on petrography and mineral chemistry from different locations covering the total area of the deposit (North and South zones of the Bégin-Lamarche deposit).

The petrographic study reveals that apatite, ilmenite, and magnetite are present in almost all samples (Table 2) either as major or accessory phases. The ubiquitous presence of these three minerals indicates that these minerals precipitated throughout the crystallization of the magma (Fig. 33). The abundances of Al-spinel are low (≤ 5%; Table 2) and the mineral is mostly associated with oxide minerals (ilmenite + magnetite; 19A and E) and is an exsolution product of magnetite. A very low abundances of sulfide minerals (≤ 1%) suggest its protracted and intermittent precipitation (Fig. 33).

Abundances of olivine, orthopyroxene, and plagioclase exhibit noteworthy characteristics. A few of the mineralised samples are composed mostly of olivine (oxide-apatite dunite), and orthopyroxene (oxide-apatite orthopyroxenite; Table 2). Other rocks (e.g., oxide-apatite olivine norite, oxide-apatite olivine gabbro, oxide-apatite olivine gabbronorite, oxide-apatite leuco troctolite; Table 2) contain variable amounts of olivine, orthopyroxene, and plagioclase. Overall, the rock assemblage suggests that the crystallization olivine started to crystallize before orthopyroxene and plagioclase and later, they continued to crystallize together (Fig. 32). Furthermore, some rocks either almost without olivine (e.g., LM16, LM 32, and LM39) or orthopyroxene (e.g., LM04, LM10, and LM12; Table 2), or plagioclase (e.g., LM09, LM10, LM12, and LM13) suggests that those minerals disappeared and reappeared within the magmatic layers possibly resulted from different magmatic events. The disappearance and reappearance of these minerals suggest that the deposit was formed due to multiple injections of magma. The presence of clinopyroxene associated with orthopyroxene and plagioclase suggests that clinopyroxene coprecipitated with these minerals (Fig. 33). ***We acknowledge that a very limited number of samples from multiple boreholes covering a wide area in this study only provide a preliminary framework of the mineral paragenesis of this deposit.***

The negative Eu anomalies in apatite (Fig. 30B) indicate that Eu preferentially partitioned into plagioclase during magma crystallization (e.g., Rollinson, 2014). This process produced plagioclase with positive Eu-anomalies (Fig. 30A). These sympathetic Eu anomalies suggest that apatite and plagioclase crystallized concurrently as is typical for all mafic intrusions.

The presence of amphibole and biotite associated with feldspar (Fig. 15E, 17B, and 18B) and alteration of orthopyroxene to amphibole (Fig. 17A and 18B) suggests that those minerals appeared after orthopyroxene at late stages of magmatic crystallization. Similarly, chlorite also formed at later stages of magmatic crystallization. Carbonatite veins cross-cut apatite (Fig. 19C) and amphiboles (not shown here), which suggests that carbonatite veins injected at the later stages of the magmatic event (Fig. 33). Furthermore, late-stage veinlets cross-cutting iddingsite suggests that the alterations of olivine to iddingsite occurred before this veining event.

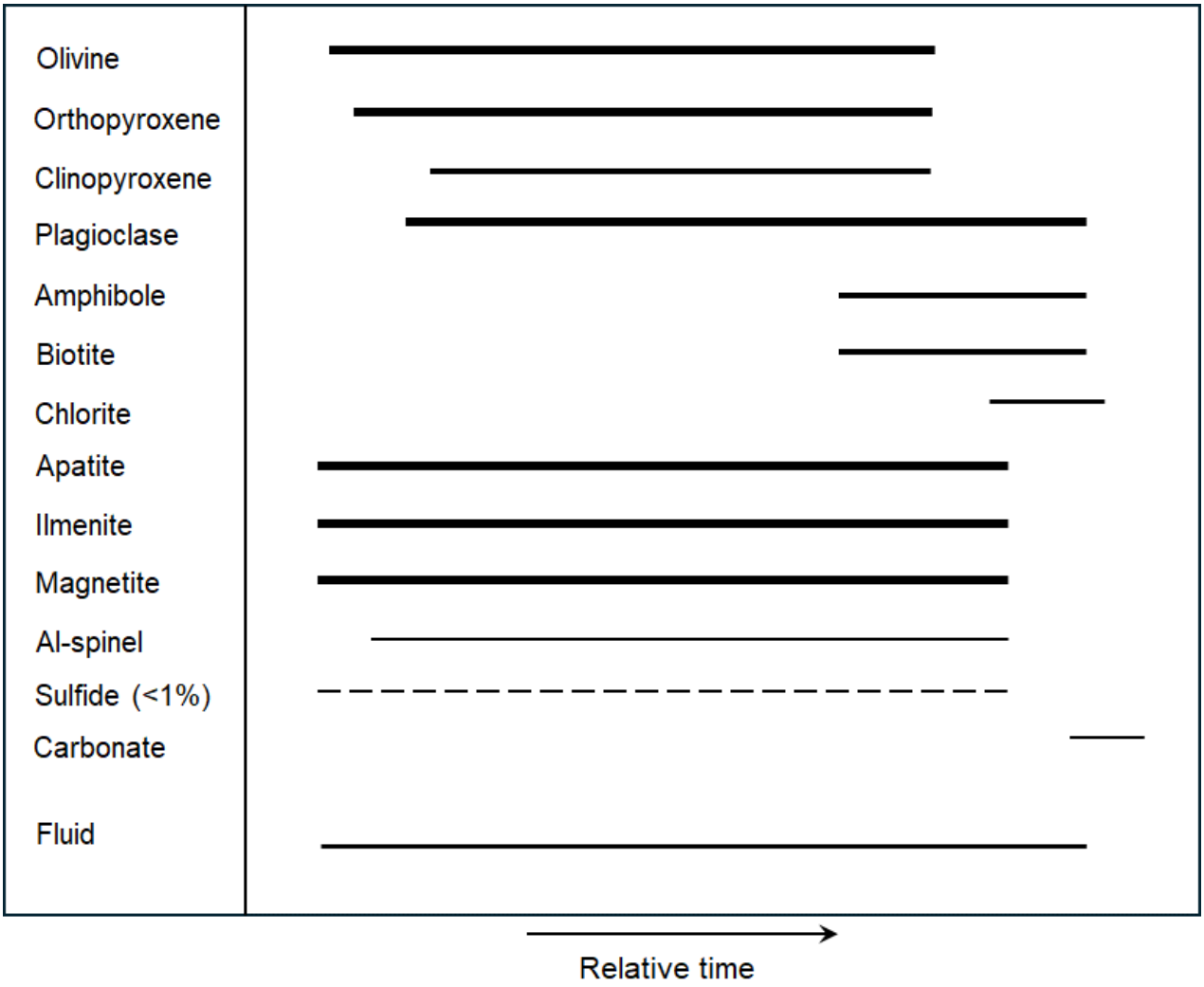

Fig. 33. Preliminary mineral paragenesis of the Bégin-Lamarche deposit (North and South Zone), Quebec, Canada. The thickness of a line corresponds to the relative abundance of a mineral. The dashed line denotes intermittent precipitation of a mineral.

The antithetic or negative correlation between the Cl content of apatite and Mg# of coexisting orthopyroxene (Fig. 23A) for one group of apatite suggests that Cl-rich fluid exsolved during the crystallization of the magma (Fig. 33), which progressively decreased the Cl content of magma during its differentiation (or crystallization). This Cl-rich fluid altered olivine to iddingsite, which resulted in higher Cl contents of altered olivine and late-stage veinlets than that of apatite (Fig. 8 in Banerjee, 2023b).

9.5. Ilmenite and magnetite as secondary commodities

Ultramafic-mafic rocks containing apatite-oxide are relatively new exploration targets for phosphate, Ti, and potentially Fe. The anorthosites of the LSJA Suite in the Grenville Province contain Ti in hemo-ilmenite within the younger, andesine anorthosite and titanomagnetite within the older, labradorite anorthosite (Anderson and Morin, 1969; Hébert et al. 2005; Charlier et al., 2015). In general, labradorite anorthosite is devoid of apatite, whereas andesine anorthosite contains apatite (Hébert et al., 2005; Grant 2020).

Ilmenite in melanocratic, oxide-rich layers in the Bégin-Lamarche deposit has a lower hematite component (X_{hem} of 0.0-0.06) than that of the Lac `a l'Orignal deposit (X_{hem} of 0.07-0.6; Miloski et al., 2024, Banerjee et al., 2024b). **TiO_2 content of ilmenite of the Bégin-Lamarche deposit (49.7-52.5 wt%) is therefore slightly higher than that of the Lac à l'Orignal deposit (46.2-50.0 wt%; Banerjee et al. 2024b)**. Furthermore, ilmenite of the Bégin-Lamarche deposit has low contents of Mg (MgO of 0.3-1.5 wt%; Table 3) and Cr (Cr_2O_3 of ≤ 0.02 wt.%; Table 3). During beneficiation, elevated Mg in ilmenite decreases the reduction rate of ilmenite to form TiO_2 (Kim, 2015) and high Cr contents decrease the whiteness of TiO_2 pigments for paints (Bonsack, 1970). A recovery of 49.7-52.5 wt.% of TiO_2 should be possible from the ilmenite of the Bégin-Lamarche deposit (Table 3). ***However, metallurgical testing is necessary to implement the proper technique to recover ilmenite from gangue minerals (such as olivine).***

Magnetite could also be an important secondary commodity as a source of Fe. It can be concentrated as a by-product of the metallurgical processing of phosphatic ore from the Bégin-Lamarche deposit. The TiO_2 content of magnetite of the Bégin-Lamarche deposit (0.15-1.36 wt%; Table 3) is slightly higher than that of the Lac à l'Orignal deposit (0.07-0.25 wt%, Banerjee et al., 2024b). The MnO (0.0-0.07 wt%) and MgO (0.01-0.15 wt%; Table 3) of the magnetite of the Bégin-Lamarche deposit are comparable to those of the Lac à l'Orignal deposit (MnO < 0.01 wt%, MgO=0.03-0.14 wt%; Banerjee et al., 2024b).

In addition to the steel industry, magnetite nanoparticles can be used for magnetic resonance imaging, manufacturing of catalysts, synthesizing of pigment, and magnetic storage (Darezereshki et al., 2018).

9.6. Use of mafic silicate minerals for CO_2 sequestration

Olivine and pyroxene react with CO_2-rich aqueous fluids at surficial temperature conditions and the reaction rates increase with temperatures (Kelemen et al., 2019; Rasool and Ahmad, 2023, Palandri and Kharaka, 2004). Similarly, plagioclase also reacts with CO_2-rich fluid, but dissolution rates of plagioclase are lower than that of olivine. Therefore, mafic silicate

(+plagioclase) mine tailing could be used for CO_2 sequestration through enhanced weathering (Kelemen et al., 2019). Although the reaction rates for the minerals are low at surficial conditions, high surface area-to-volume ratios of mine tailing can increase reactivity. Carbon mineralization in mine tailings can be enhanced by several methods, such as sparging air, air-saturated water, or CO_2-rich gas through the tailings, stirring the tailings to have a turnover of reactive surfaces in contact with air, or adding microorganisms that accelerate the formation of carbonates (Kelemen et al., 2019 and references therein). Another option is grinding the mafic silicate minerals smaller than mine tailing sizes and mixing them with agriculture soil, forest soil, or along beaches and the CO_2 sequestration process can be enhanced by microbial processes in soils (Beerling et al., 2018, Power et al., 2013, Kelemen et al., 2019).

The mafic silicate minerals (olivine, pyroxene) and plagioclase from the Bégin-Lamarche deposit would be suitable for CO_2 sequestration. Low concentrations of trace elements in these minerals and very low abundances of sulfide minerals of the Bégin-Lamarche deposit can make the mafic silicate and plagioclase fractions of the deposit an excellent source for helping to reduce the carbon footprint of the atmosphere. The assessment of heavy metal contents (such as Cr, Ni, Co, Cr, and Zn) of the minerals and their impact on the environment (e.g., in soil) needs to be investigated before the use of mafic silicate minerals (+plagioclase) for CO_2 sequestration.

10. Conclusions

1. The mineralization of First Phosphate's Bégin-Lamarche deposit (North and South Zone) is widely variable, but is dominated by oxide-apatite mafic rocks (such as oxide-apatite gabbronorite, oxide-apatite olivine gabbronorite, oxide-apatite olivine norite, oxide-apatite leuco-norite, apatite leuco-olivine norite, oxide-apatite mela-norite, oxide-apatite mela-olivine norite, oxide-apatite olivine gabbro, oxide-apatite leuco-troctolite), oxide-apatite ultramafic rocks (such as oxide-apatite dunite, oxide-apatite lherzolite, oxide-apatite harzburgite, oxide-apatite olivine orthopyroxenite, and oxide-apatite orthopyroxenite) and minor massive nelsonite (oxide-apatite only). These rocks contain variable amounts of olivine, orthopyroxene, clinopyroxene, plagioclase, amphibole, biotite, chlorite, apatite, ilmenite, magnetite, and Al-spinel. Fluorapatite is the primary ore mineral and ilmenite, and magnetite are potentially important secondary commodities.

2. The P_2O_5 concentration of *in situ* apatite is 41.7 ±0.13 wt.%, which is comparable to that of the apatite concentrate (40.9 wt.%) produced and analyzed by SGS. P_2O_5 and CaO concentrations and CaO/P_2O_5 ratios are better than required for phosphoric acid production. Therefore, the Bégin-Lamarche deposit is a potentially viable source of P for the LFP battery market.

3. The F content of apatite is lower than the concerning levels for producing phosphoric acid. In general, apatite from some areas of the deposit contains Cl contents lower than levels of concern for the production of phosphoric acid. However, the deposit may have patchy (or local) distributions of apatite with high Cl contents (> 1000 ppm). Cl concentrations could be managed by mixing ores with different Cl contents. Advanced methods for the reduction of Cl should also be explored.

4. The MER of the apatite concentrate prepared and analyzed by SGS is low (0.04). Si, Ti, Na, As, Cd, Th, and U concentrations of apatite are lower than their required values for producing phosphoric acid. Low concentrations of trace and radioactive elements (Pb, Th, and U) in apatite will produce high-quality and environment-friendly phosphogypsum as a by-product during phosphoric acid production. The phosphogypsum could potentially be recycled into plaster and wallboard.

5. The low abundance of sulfide gangue minerals (< 1%) suggests that the environmental risks of acid mine drainage from tailings would be minimal. Such low concentrations of toxic trace elements and sulfide minerals make the Bégin-Lamarche deposit an attractive ESG-compliant source of North American P for the LFP battery industry.

6. Higher TiO_2 content (49.7-52.5 wt%) and lower hematite component (X_{hem} of 0.0-0.06) of ilmenite of the Bégin-Lamarche deposit than those of the Lac à l'Orignal deposit suggest that high recovery of TiO_2 is possible from the ilmenite of the Bégin-Lamarche deposit. However, metallurgical testing is recommended.

7. The mafic silicate minerals (e.g., olivine and pyroxene) and plagioclase of the deposit can be used for CO_2 sequestration, which can reduce the carbon footprint of the atmosphere. The use of gangue minerals to mitigate climate change and environmental protection could be an additional value to the ESG.

8. This study suggests that the deposit formed due to multiple injections of magma. (Fluor)apatite from one group of samples shows a good positive correlation between the Cl content of apatite and Mg# of coexisting orthopyroxene. This relation indicates that the low Cl content of apatite will be associated with low Mg# of orthopyroxene. As halogen component (F and Cl) analysis of apatite is challenging, Mg# of orthopyroxene can be used to trace the locations of high-quality phosphate ore in the Bégin-Lamarche deposit.

9. The positive correlation between the Cl content of (fluor)apatite and Mg# of coexisting orthopyroxene suggests that the Cl-rich fluid (brine) was exsolved from the magma during its crystallization and that fluid was responsible for the alterations of the minerals, particularly olivine, of the deposit.

10. Paragenetic relationships indicate that apatite precipitated throughout the crystallization history of the magma and is mostly associated with oxide minerals (ilmenite+ magnetite). Therefore, magnetic survey is the best method for locating this type of high-quality anorthosite-hosted phosphate deposit.

11. Recommendations

The results from this study indicate that the deposit could produce high-quality phosphate ore as a raw material for the LFP battery. The patchy or local distributions of (fluor)apatite with high Cl content (> 1000 ppm) in the deposit could hinder smooth mining operations. This can be resolved if the high Cl (fluor)apatite area can be delineated in advance. A previous study showed

that the whole-rock Cl content does not necessarily correlate to the Cl content of apatite crystals, i.e., a rock with high Cl content does not also have (fluor)apatite with high Cl content (Banerjee, 2023b). This study showed a good positive correlation between the Cl content of apatite and Mg# of coexisting orthopyroxene (for one group of samples) and the relation is related to the magmatic crystallization process. Therefore, a more detailed study of Cl contents of apatite from this deposit is recommended and will be helpful for future mining operations.

It would be advantageous to do a high-frequency sampling from one drill core for petrography and geochemistry study (particularly for the Cl contents of apatite). Later the results from that drill hole could be compared to the results of strategically selected samples from other drill holes. The 3D model of ore bodies (which was built during mineral reserve estimation) will be helpful in strategically selecting samples from other drill cores. Furthermore, high-frequency sampling from a drill core will help to establish the paragenesis in a more refined way that will be beneficial for the exploration of high-quality phosphate ore in the deposit.

12. References

Ahsan, Z., Ding, B., Cai, Z., Wen, C., Yang, W., Ma, Y., Zhang, S., Song, G., Javed, M.S. (2021). Recent progress in capacity enhancement of LiFePO4 cathode for Li-ion batteries. Journal of Electrochemical Energy Conversion and Storage 18, 010801.

Anderson, A.T., Morin, M. (1969). Two types of massif anorthosite and their implications regarding the thermal history of the crust. In: Isachsen, Y.W. (Ed.), Origin of Anorthosite and Related Rocks. New York State Museum and Science Service Memoir 18, 57–69.

Andersson, S.S., Wagner, T., Jonsson, E., Fusswinkel, T., Whitehouse, M.J. (2019). Apatite as a tracer of the source, chemistry, and evolution of ore-forming fluids: the case of the Olserum-Djupedal REE-phosphate mineralization, SE Sweden. Geochimica et Cosmochimica Acta 255, 163–187.

Ashwal, L.D. (1993). Anorthosites. Springer, Heidelberg.

Ashwal, L.D. (2010). The temporality of anorthosites. The Canadian Mineralogist. 48, 711–728.

Ayers, J.C., Watson, E.B. (1993). Apatite/fluid partitioning of rare-earth elements and strontium: Experimental results at 1.0 GPa and 1000 C and application to models of fluid-rock interaction. Chemical Geology, 110(1-3), 299-314.

Banerjee, S. (2023a). Characterization of First Phosphate's Lac à l'Orignal phosphate deposit, Lac-Saint-Jean Anorthosite (LSJA) Complex, Quebec, Canada: Implications for supplying lithium ferro (Iron) phosphate (LFP) Batteries (Technical report prepared for First Phosphate Corp.).

Banerjee, S. (2023b). Cl contents of phosphatic layers in First Phosphate's Bégin-Lamarche property, Quebec, Canada (Technical report prepared for First Phosphate Corp.).

Banerjee, S., Pufahl, P.K., Dare, S. (2024a) Igneous rock phosphate: ore grades, concentrates, and mining operations around the world. (Technical report prepared for First Phosphate Corp.).

Banerjee, S., Pufahl, P.K., Longstaffe, F.J. (2024b). The Lac à l'Orignal phosphate deposit and constraints on high-quality phosphatic ore in massif-type anorthosite, Grenville Province, Canada. Journal of Geochemical Exploration 263, 107499.

Beerling, D. J., Leake, J. R., Long, S. P., Scholes, J. D., Ton, J., Nelson, P. N., et al. (2018). Farming with crops and rocks to address global climate, food, and soil security. Nature Plants 4, 138–147.

BM Review. (2022). Identifying the pinch points in the LFP supply chain. Battery Materials Review 5(2), 1-4.

Bonsack, J.P. (1970). Titanium Dioxide Pigment. Liquid-Liquid Extraction of Chromium. Industrial & Engineering Chemistry Product Research and Development, 9(3), 398-403.

Bybee, G.M., Ashwal, L.D., Shirey, S.B., Horan, M., Mock, T., Andersen, T.B. (2014). Pyroxene megacrysts in Proterozoic anorthosites: Implications for tectonic setting, magma source and magmatic processes at the Moho. Earth and Planetary Science Letters 389, 74–85.

Carr, S.D., Easton, R.M., Jamieson, R.A., Culshaw, N.G. (2000). Geologic transect across the Grenville orogen of Ontario and New York. Canadian Journal of Earth Sciences 37, 193–216.

Chandra, K., Mahanti, A., Kain, V., Kumar, B.S., Kumar, N., Gautam, V. (2017). Failure cases related to material issues in wet-process phosphoric acid plant. Engineering Failure Analysis, 79, 642-655.

Charlier, B., Duchesne, J.C., Vander Auwera, J., Storme, J.Y., Maquil, R., Longhi, J. (2010). Polybaric fractional crystallization of high-alumina basalt parental magmas in the Egersund–Ogna massif-type anorthosite (Rogaland, SW Norway) constrained by plagioclase and high-alumina orthopyroxene megacrysts. Journal of Petrology 51, 254–2515.

Charlier, B., Namur, O., Bolle, O., Latypov, R., Duchesne, J.C. (2015). Fe–Ti–V–P ore deposits associated with Proterozoic massif-type anorthosites and related rocks. Earth-Science Reviews 141, 56–81.

Charlier, B., Sakoma, E., Sauvé, M., Stanaway, K., Vander Auwera, J., Duchesne, J.C. (2008). The Grader layered intrusion (Havre-Saint-Pierre Anorthosite, Quebec) and genesis of nelsonite and other Fe–Ti–P ores. Lithos 101, 359–378.

Cohen, J. (1988). Statistical Power Analysis for the Behavioral Sciences. Routledge Academic, New York, NY.

Corriveau, L., Perreault, S., Davidson, A. (2007). Prospective metallogenic settings of the Grenville Province. In: Goodfellow, W.D. (Ed.), Mineral Deposits of Canada: A Synthesis of Major Deposit-Types, District Metallogeny, the Evolution of Geological Provinces, and Exploration Methods: Geological Survey of Canada. Special Publication, Mineral Deposits Division, pp. 819–847.

Darezereshki, E., Khodadadi Darban, A., Abdollahy, M. (2018). Synthesis of magnetite nanoparticles from iron ore tailings using a novel reduction-precipitation method. Journal of Alloys and Compounds, 749, 336-343.

Darling, R.S., Florence, F.P., Lester, G.W., Whitney, P.R. (2004). Petrogenesis of prismatine–bearing metapelitic gneisses along the Moose River, west-Central Adirondacks, New York. In: Tollo, R.P., Corriveau, L., McLelland, J., Bartholomew, M. (Eds.), Proterozoic Tectonic Evolution of the Grenville Orogen in North America: Memoirs, vol. v. 197, pp. 325–336.

DeBari, S.M., Coleman, R.G. (1989). Examination of the deep levels of an island arc: evidence from the Tonsina ultramafic-mafic assemblage, Tonsina, Alaska. Journal of Geophysical Research: Solid Earth 94 (B4), 4373–4391.

Diyoyo, K.J., Simard, R-L., Dare, S., Moukhsil, A. (2024). Cartographie de la Suite anorthositique de Lac-Saint-Jean (SALSJ) dans le secteur des minéralisations de Fe-Ti-V-P du corridor de Saint-Charles-de-Bourget et de Bégin-Lamarche. MB 2024-08. Ministère des ressources naturelles et des forêts. 37 pages.

Donovan, J.J., Snyder, D.A., Rivers, M.L. (1993) An improved interference correction for trace element analysis. Microbeam Analysis, 2, 23–28.

Emslie, R.F., Hamilton, M.A., Thériault, R.J., 1994. Petrogenesis of a Mid-Proterozoic anorthosite-mangerite-charnockite-granite (AMCG) complex: isotope and geochemical evidence from the Nain Plutonic suite. The Journal of Geology 102, 539–558.

European Commission (2020). Communication from the commission to the European Parliament, the Council, the European Economic, and Social Committee, and the Committee of the regions. Critical Raw Materials Resilience: Charting a Path towards greater Security and Sustainability COM/2020/4.

Government of Canada (2024). Government of Canada releases updated critical mineral list, Natural Resources Canada, News release dated June 10, 2024.

Government of Ontario (2022). Ontario's Critical Minerals Strategy: Unlocking potential to drive economic recovery and prosperity, p. 53.

Government of Quebec (2024). QPDCSM summary sheet.

Grant, M. (2020). Formation of Magmatic Fe-Ti-VP Deposits within the Lac St. Jean Area Saguenay, Qu´ebec, Canada: Insights from Trace Element Composition of Fe-Oxides and Apatite (M.Sc dissertation, Universit´e d'Ottawa/University of Ottawa).

Guimarães, L.F., Botelho Junior, A.B., Espinosa, D.C.R. (2023). The Characterization of Li-ion Batteries and the Importance of the Recycling Processes. JOM, 75(9), 3622-3631.

Hassen Ali, T.H., Simard, R-L., Dare, S., Moukhsil, A. (2024). Cartographie pétrogéochimique par XRF portative de la marge sud de la Suite anorthositique de Lac Saint-Jean (secteur St-Bruno-Arvida) et des minéralisations de Fe-Ti-V-P associées, Province de Grenville central, Québec. MB 2024-07. Ministère des ressources naturelles et des forêts. 65 pages.

Hassen Ali, T.H., Simard, R-L., Dare, S, Moukhsil, A. (2023). Contexte géologique des minéralisations de Ni-Cu ± Co et de Fe-V-Ti-P de la marge ouest de la Suite anorthositique de Lac-Saint-Jean. MB 2023-08. Ministère de ressources naturelles et forêts. 70 pages.

Hébert, C., Cadieux, A.M., van Breemen, O. (2005). Temporal evolution and nature of Ti–Fe–P mineralization in the anorthosite–mangerite–charnockite–granite (AMCG) suites of the south-central Grenville Province, Saguenay–Lac St. Jean area, Québec, Canada. Canadian Journal of Earth Sciences 42, 1865–1880.

Hébert, C., Lacoste, P. (1998). Géologie de la région de Lac Jalobert (22D/10). RG-97-05.

Heinonen, A., Kivisaari, H., Michallik, R.M. (2020). High-aluminum orthopyroxene megacrysts (HAOM) in the Ahvenisto complex, SE Finland, and the polybaric crystallization of massif-type anorthosites. Contrib. Mineralogy and Petrology 175, 1–25.

Helbig, C., Bradshaw, A.M., Wietschel, L., Thorenz, A., Tuma, A. (2018). Supply risks associated with lithium-ion battery materials. Journal of Cleaner Production, 172, 274-286.

Helmy, H.M., Abd El-Rahman, Y.M., Yoshikawa, M., Shibata, T., Arai, S., Tamura, A., Kagami, H. (2014). Petrology and Sm–Nd dating of the Genina Gharbia Alaskan-type complex (Egypt): insights into deep levels of Neoproterozoic island arcs. Lithos 198, 263–280.

Higgins, M.D., Ider, M., van Breemen, O. (2002). U-Pb ages of plutonism, wollastonite formation, and deformation in the central part of the Lac-Saint-Jean anorthosite suite. Canadian Journal of Earth Sciences, 39(7), 1093-1105.

Higgins, M.D., van Breemen, O. (1992). The age of the Lac-Saint-Jean Anorthosite complex and associated mafic rocks, Grenville Province, Canada. Canadian Journal of Earth Sciences 29, 1412–1423.

Higgins, M.D., van Breemen, O. (1996). Three generations of Anorthosite–Mangerite–Charnockite–Granite magmatism, contact metamorphism and tectonism in the Saguenay-Lac-St-Jean region, Grenville Province, Canada. Precambrian Research 79, 347–362.

Hynes, A., Rivers, T. (2010). Protracted continental collision—evidence froSGSm the Grenville orogen. Canadian Journal of Earth Sciences 47, 591–620.

Ibanez-Mejia, M., Ruiz, J., Valencia, V.A., Cardona, A., Gehrels, G.E., Mora, A.R. (2011). The Putumayo Orogen of Amazonia and its implications for Rodinia reconstructions New U–Pb geochronological insights into the Proterozoic tectonic evolution of northwestern South America. Precambrian Research 191, 58–77.

Intissar, R., Benhamed, S., Bates, M. (2021). Levé magnétique et spectrométrique aéroporté dans le secteur du Lac-Saint-Jean est, Province de Grenville. DP 2021-03.

Jacobs, J., Pisarevsky, S., Thomas, R.J., Becker, T. (2008). The Kalahari Craton during the assembly and dispersal of Rodinia. Precambrian Research 160, 142–158.

Jochum, K.P., Weis, U., Stoll, B., Kuzmin, D., Yang, Q., Raczek, I., Jacob, D.E., Stracke, A., Birbaum, K., Frick, D.A., Günther, D. (2011). Determination of reference values for NIST SRM 610–617 glasses following ISO guidelines. Geostandards and Geoanalytical Research, 35(4), 397-429.

Jochum, K.P., Willbold, M., Raczek, I., Stoll, B., Herwig, K. (2005). Chemical Characterisation of the USGS Reference Glasses GSA-1G, GSC-1G, GSD-1G, GSE-1G, BCR-2G, BHVO-2G

and BIR-1G Using EPMA, ID-TIMS, ID-ICP-MS and LA-ICP-MS. Geostandards and Geoanalytical Research 29(3), 285-302.

Kelemen, P., Benson, S.M., Pilorgé, H., Psarras, P., Wilcox, J. (2019). An overview of the status and challenges of CO2 storage in minerals and geological formations. Frontiers in Climate 1, 482595.

Kharbish, S., Eldosouky, A.M., Amer, O. (2022). Integrating mineralogy, geochemistry and aeromagnetic data for detecting Fe–Ti ore deposits bearing layered mafic intrusion, Akab El-Negum, Eastern Desert, Egypt. Scientific Reports 12, 1–19.

Kieffer, M.A., Dare, S.A., Namur, O. (2023). The use of trace elements in apatite to trace differentiation of a ferrobasaltic melt in the Sept-Iles Intrusive Suite, Quebec, Canada: Implications for provenance discrimination. Geochimica et Cosmochimica Acta 342, 169–197.

Kim, P. H. (2015). Impurities in Ilmenite: Magnesium (Master's thesis, NTNU).

Kobylinski, C. (2015). Characterization and comparison of the oxide-rich footwall rocks of the anorthosite-hosted P-Ti deposit of Lac à Paul, Québec. (B.Sc. Honours Thesis, University of Ottawa).

Laurin, A.F., Sharma, K.N.M. (1972). Geology of the Mistassini River north, Mistassini River south, Peribonca Lake, Pipmuacan Reservoir, Chicoutimi and Baie St-Paul map-areas, Quebec: Grenville project 1965,1966, 1967. DP. 126.

Li, J., Ma, Z.F. (2019). Past and present of LiFePO4: from fundamental research to industrial applications. Chem 5(1), 3-6.

Liu, X., Li, K., Li, X. (2018). The electrochemical performance and applications of several popular lithium-ion batteries for electric vehicles-a review. In Advances in Green Energy Systems and Smart Grid: First International Conference on Intelligent Manufacturing and Internet of Things and 5th International Conference on Computing for Sustainable Energy and Environment, IMIOT and ICSEE 2018, Chongqing, China, September 21-23, 2018, Proceedings, Part III 5 (pp. 201-213). Springer Singapore.

Ludden, J., Hynes, A. (2000). The Lithoprobe Abitibi-Grenville transect: two billion years of crust formation and recycling in the Precambrian Shield of Canada. Canadian Journal of Earth Sciences 37, 459–476.

Lunde, A. E. (2022). Investigating how the LFP battery demand is shaping the future of phosphorus and the role of secondary resources. Master's thesis, Norwegian University of Science and Technology.

Marks, M.A., Wenzel, T., Whitehouse, M.J., Loose, M., Zack, T., Barth, M., Worgard, L., Krasz, V., Eby, G.N., Stosnach, H., Markl, G. (2012). The volatile inventory (F, Cl, Br, S, C) of magmatic apatite: an integrated analytical approach. Chemical Geology 291, 241–255.

Miao, Y., Hynan, P., Von Jouanne, A., Yokochi, A. (2019). Current Li-ion battery technologies in electric vehicles and opportunities for advancements. Energies, 12(6), 1074.

Miloski, P., Dare, S., Morisset, C.E., Davies, J.H., Perrot, M.G., Savard, D. (2024). Petrogenesis of Fe-Ti-P mineral deposits associated with Proterozoic anorthosite massifs in the Grenville Province: insights from oxide and apatite trace-element geochemistry at Lac `a l'Orignal, Quebec, Canada. Mineral Deposita 59, 519-556.

Miloski, P., Dare, S., Morisset, C.E., Perrot, M.G., Davies, J.H. (2023). Petrogenesis of oxide-apatite mineralization associated with Proterozoic anorthosite massifs at Lac Mirepoix, Quebec, Canada: a multi-stage model for Fe-Ti-P mineralization in the Central Grenville Province. Ore Geology Reviews 163, 105734.

Morisset, C.E., Scoates, J.S., Weis, D., Friedman, R.M. (2009). U–Pb and 40Ar/39Ar geochronology of the Saint-Urbain and Lac Allard (Havre-Saint-Pierre) anorthosites and their associated Fe–Ti oxide ores, Qu´ebec: Evidence for emplacement and slow cooling during the collisional Ottawan orogeny in the Grenville Province. Precambrian Research 174, 95–116.

Murdock, B.E., Toghill, K.E., Tapia-Ruiz, N. (2021). A perspective on the sustainability of cathode materials used in lithium-ion batteries. Advanced Energy Materials 11(39), 2102028.

Namur, O., Charlier, B., Toplis, M.J., Higgins, M.D., Liégeois, J.P., Vander Auwera, J., (2010). Crystallization sequence and magma chamber processes in the ferrobasaltic Sept Iles layered intrusion, Canada. Journal of Petrology 51, 1203–1236.

Ouabid, M., Raji, O., Dautria, J.M., Bodinier, J.L., Parat, F., El Messbahi, H., Garrido, C. J., Ahechach, Y., 2021. Petrological and geochemical constraints on the origin of apatite ores from Mesozoic alkaline intrusive complexes, Central High-Atlas, Morocco. Ore Geology Reviews 136, 104250.

Owens, C.L., Nash, G.R., Hadler, K., Fitzpatrick, R.S., Anderson, C.G., Wall, F. (2019). Apatite enrichment by rare earth elements: A review of the effects of surface properties. Advances in colloid and interface science, 265, 14-28.

Paiement, J-P, Gagne, J., Duplessis, C., Rousseau, G., Gagnon, G., Dagbert, M. (2013). Pre-Feasibility Study Mine Arnaud lnc. Sept-Iles Deposit, Québec. SGS Canada.

Palandri, J.L., Kharaka, Y.K. (2004). A compilation of rate parameters of water-mineral interaction kinetics for application to geochemical modeling (No. 2004-1068). US Geological Survey.

Paton, C., Hellstrom, J., Paul, B., Woodhead, J., and Hergt, J. (2011). Iolite: Freeware for the visualisation and processing of mass spectrometric data. Journal of Analytical Atomic Spectrometry, 26(12), 2508-2518.

Philpotts, A.R. (1967). Origin of certain iron-titanium oxide and apatite rocks. Economic Geology 62, 303-315.

Pourmand, A., Dauphas, N., Ireland, T.J. (2012). A novel extraction chromatography and MC-ICP-MS technique for rapid analysis of REE, Sc and Y: Revising CI-chondrite and Post-Archean Australian Shale (PAAS) abundances. Chemical Geology, 291, 38-54.

Power, I.M., Harrison, A.L., Dipple, G.M., Wilson, S.A., Kelemen, P.B., Hitch, M., et al. (2013). Carbon mineralization: from natural analogues to engineered systems. Reviews in Mineralogy and Geochemistry 77, 305–360.

Prayon (2022). Chemical specification of phosphate ore for producing phosphoric acid. (e-mail communication).

Prowatke, S., Klemme, S. (2006). Trace element partitioning between apatite and silicate melts. Geochimica et Cosmochimica Acta, 70(17), 4513-4527.

Pufahl, P.K., Groat, L.A. (2017). Sedimentary and igneous phosphate deposits: formation and exploration: an invited paper. Economic Geology, 112(3), 483-516.

Ragan, D.M. (1969). Olivine recrystallization textures. Mineralogical Magazine, 37(286), 238-240.

Rasool, M.H., Ahmad, M. (2023). Reactivity of basaltic minerals for CO_2 sequestration via in situ mineralization: a review. Minerals, 13(9), 1154.

Rivers, T. (2012). Upper-crustal orogenic lid and mid-crustal core complexes: signature of a collapsed orogenic plateau in the hinterland of the Grenville Province. Canadian Journal of Earth Sciences 49, 1–42.

Rivers, T. (1997). Lithotectonic elements of the Grenville Province: review and tectonic implications. Precambrian Research 86, 117–154.

Rollinson, H. R. (2014). Using geochemical data: evaluation, presentation, interpretation. Routledge.

Salas B.V., Wiener M.S., Martinez J.R.S. (2017). Phosphoric Acid Industry: Problems and Solutions, in Phosphoric Acid Industry-Problems and Solutions, Wiener M.S., Valdez B. (Eds.), InTech, 172.

Schorr, M., Valdez, B. (2017). Phosphoric Acid Industry: Problems and Solutions. BoD – Books on Demand.

Spears, B.M., Brownlie, W.J., Cordell, D., Hermann, L., Mogollón, J.M. (2022). Concerns about global phosphorus demand for lithium-iron-phosphate batteries in the light electric vehicle sector. Communications Materials, 3(1), 14.

Steiner, G., Geissler, B., Watson, I., Mew, M.C. (2015). Efficiency developments in phosphate rock mining over the last three decades. Resources, Conservation and Recycling, 105, 235-245.

Tran, Y.H.T., Han, J., Song, S.W. (2021). Solid electrolyte interphase stabilization path to lithium metal plating-free high-energy lithium-ion battery under subzero-temperature. Journal of The Electrochemical Society, 168(2), 020529.

Trost, J.N., Dunn, J.B. (2023). Assessing the feasibility of the inflation Reduction Act's EV critical mineral targets. Nature Sustainability 6, 639–643.

Walsh, M., Schenk, G., Schmidt, S. (2023). Realising the circular phosphorus economy delivers for sustainable development goals. npj Sustainable Agriculture, 1(1), 2.

Walvekar, H., Beltran, H., Sripad, S., Pecht, M. (2022). Implications of the electric vehicle manufacturers' decision to mass adopt lithium-iron phosphate batteries. IEEE Access, 10, 63834-63843.

Wang, H., Feng, K., Wang, P., Yang, Y., Sun, L., Yang, F., Chen, W.Q., Zhang, Y., Li, J. (2023). China's electric vehicle and climate ambitions jeopardized by surging critical material prices. Nature Communications 14, 1246.

Webster, J.D., Iveson, A.A., Rowe, M.C., Webster, P.M. (2020). Chlorine and felsic magma evolution: Modeling the behavior of an under-appreciated volatile component. Geochimica et Cosmochimica Acta 271, 248-288.

Woodhead, J.D., Hellstrom, J., Hergt, J. M., Greig, A., Maas, R. (2007). Isotopic and elemental imaging of geological materials by laser ablation inductively coupled plasma-mass spectrometry. Geostandards and Geoanalytical Research, 31(4), 331-343.

Woussen, G., Dimroth, E., Corriveau, L., Archer, P., (1981). Crystallization and emplacement of the Lac St-Jean anorthosite massif (Quebec, Canada). Contributions to Mineralogy and Petrology 76, 343–350.

Ye, N., Yan, T., Jiang, Z., Wu, W., Fang, T. (2018). A review: conventional and supercritical hydro/solvothermal synthesis of ultrafine particles as cathode in lithium battery. Ceramics International 44, 4521–4537.